Semiconductor Device Simulation: A Spectral Method for Solution of the Boltzmann Transport Equation

by

Yannick L. Le Coz
B.S., Rensselaer Polytechnic Institute
(1980)
S.M., Massachusetts Institute of Technology
(1982)

Submitted in partial fulfillment
of the requirements of
the degree of

Doctor of Philosophy

at the

MASSACHUSETTS INSTITUTE OF TECHNOLOGY

January 1988

Signature of Author_____
Department of Electrical Engineering and Computer Science
January 29, 1988

Certified by_____
Alan L. McWhorter
Thesis Supervisor

Accepted by_____
Arthur C. Smith
Chairman, Departmental Committee on Graduate Students

Semiconductor Device Simulation: A Spectral Method for Solution of the Boltzmann Transport Equation

by

Yannick L. Le Coz

Submitted to the Department of Electrical Engineering and Computer Science on January 29, 1988, in partial fulfillment of the requirements for the degree of Doctor of Philosophy.

ABSTRACT

Theoretical investigation of short length- and time-scale transport phenomena in semiconductor devices necessitates a full dynamical analysis. Under the assumption of semiclassical behavior, the Boltzmann transport equation (BTE) is useful in describing transport in semiconductors. An efficient numerical method for solving the BTE has been developed using a basis-function expansion of the distribution function's velocity dependence. This spectral method is ten to one-hundred times faster than the conventional Monte Carlo method, for equivalent accuracy.

The spectral method is developed through a hierarchical sequence of numerical calculations. Initial calculations deal with solution of the BTE by means of conventional numerical methods. These methods are applied to simple systems, possessing two space-velocity variables. A spectral method is then developed for solution of the BTE in the case of three space-velocity variables. Lastly, the spectral method is extended to systems that have four or more space-velocity variables.

Issues pertaining to computational efficiency, numerical errors, and future modifications and applications of the spectral method are also addressed.

Thesis Supervisor: Alan L. McWhorter
Title: Professor of Electrical Engineering

Acknowledgments

It pleases me to thank all those who have helped me in completing this work. In particular, I am indebted to Prof. A.L. McWhorter for his guidance and unusual patience.

I would like to personally thank Prof. D.A. Antoniadis for generously providing his computational resources and participating as a thesis reader, not to mention first introducing me to the world of scientific research.

Thanks, too, to other MIT faculty and research staff for their advice, assistance, and contribution to my education: Profs. M.B. Giles, A.T. Patera, L.R. Reif, M. Schlecht, S.D. Senturia, and A.C. Smith.

I cannot forget my friends from MIT and environs, who have made my stay in Boston all the more fun and interesting: Kristen Day, Steve Garverick, Bob Harris, Merit Hung, Ralph and Pat Iverson, Jarvis Jacobs, Ed Maby, Mark and Susan (to be) Rodder, Frank Smith, Thye-Lai Tung, Jim Vlcek, and many others.

And last, I say thank you Mom and Dad for everything; you guys, too, Christian, Monica, and Yolande.

Contents

List of Figures

List of Tables

Chapter 1

Introduction

In recent decades, the rapid evolution of semiconductor technology has resulted in extremely small device geometries. This trend towards smaller and smaller geometries derives from the importance of increasing electrical speed and integration density. Conventional and novel device design have benefited from advancements in semiconductor technology. For example, advancements in photolithography, molecular-beam epitaxy, and organometallic chemical-vapor deposition [1,2], have stimulated research in bipolar junction transistor and metal-oxide-semiconductor field-effect transistor design, and have aided in the development of novel devices, such as the high electron mobility transistor and the permeable-base transistor [3,4].

Increasingly sophisticated simulation techniques must be devised to describe device behavior. These techniques have to portray nonequilibrium phenomena that vary rapidly in space and time. Incorporation of complicated collision processes is also essential. In addition, simulation techniques should be efficient—a proper balance between computational effort and solution accuracy must be realized.

With the above requirements in mind, the simulation technique proposed in this work is based upon the Boltzmann transport equation (BTE) [5]. Solution of the BTE permits evaluation of numerous macroscopic quantities, such as carrier concentration, mean carrier velocity, and mean carrier kinetic energy. The BTE formalism provides a reasonably accurate description of transport in many semiconductor devices of current interest.

1.1 Basic Physics

1.1.1 Transport

The BTE is predicated on the assumption that charge carriers behave quasi-classically. The conditions under which the "quasi-classical assumption" is justified are readily determined through a detailed quantum-mechanical analysis [6].[1] Fortunately, the outcome of this analysis is easily implemented: the classical mass of each carrier is replaced with an effective mass m^*. Classical laws of motion and quantities such as momentum,[2] $\boldsymbol{p}= m^*\boldsymbol{v}$, and kinetic energy, $\varepsilon = m^*v^2/2$, remain unchanged.[3] As a final note, the concept of phase space is also valid in the quasi-classical regime. The six-dimensional phase-space domain $(\boldsymbol{r},\boldsymbol{p})$ is viewed as a well-defined continuum.[4]

Transport in semiconductor devices involves two classical phenomena: drift and diffusion. Drift effects arise from macroscopic electric fields and result in a net carrier flux. Diffusion effects are a consequence of random thermal motion; thus, inhomogeneities in carrier concentration will also result in a net carrier flux. Both these effects are incorporated in the BTE.

Collisions must also be considered. The important collision processes in

[1] A discussion concerning the validity of the quasi-classical assumption will be given later in Section 1.1.3.

[2] The vector $\boldsymbol{p} = m^*\boldsymbol{v}$ is in reality a quasi momentum called crystal momentum, which is a quantum number associated with each carrier state. Crystal momentum and carrier momentum have similar properties, for example, $d\boldsymbol{p}/dt = \boldsymbol{F}$ where where $\boldsymbol{F}$ is the force on the carrier, but the two quantities are different in other respects (see footnote 14).

[3] Carriers are assumed located near the minimum of a single, spherical, parabolic band. The assumption is used throughout this work and is made solely for purposes of simplification. However, the numerical solution procedure that will be proposed can be used to simulate multivalley systems with aspherical, nonparabolic bands.

[4] The charge carriers cannot be represented as idealized points in phase space. Uncertainty smearing "broadens" phase-space coordinates: $\Delta r > a$ and $\Delta p \sim \hbar/\Delta r$, where a is the lattice constant. The point-in-phase-space description can be recovered, however, if spatial and momentum scales are considered large in comparison with Δr and Δp respectively.

semiconductors are:

- phonon scattering,[5]
- crystal-defect scattering,
- carrier-carrier scattering, and
- ionized and neutral impurity scattering.

This work is primarily concerned with collisions engendered by lattice vibrations, that is, phonon scattering.[6] The theory of carrier-phonon scattering is quite involved and is based on a quantum-mechanical treatment of the carrier-phonon interaction [6] (see also Appendix E). In brief, the scattering process is described by a perturbation of the potential "seen" by the charge carriers. Time-dependent perturbation theory is then used to calculate a scattering-probability-rate function $S(\boldsymbol{v},\boldsymbol{v}')$. The quantity $S(\boldsymbol{v},\boldsymbol{v}')d^3v'dt$ gives the probability that a carrier is scattered from an initial velocity $\boldsymbol{v}$ to a final velocity within $(\boldsymbol{v}', \boldsymbol{v}' + d\boldsymbol{v}')$ during the infinitesimal time interval dt. The scattering-probability-rate function includes contributions from interactions which absorb a single phonon and those which emit a single phonon.

At this point, the fundamental processes that govern transport in semiconductors—drift, diffusion, and collisions—have been introduced and derivation of the BTE is now possible. The carrier ensemble is treated using statistical methods. The "state" of an individual carrier is defined by its phase-space coordinates $(\boldsymbol{r},\boldsymbol{v})$.[7] The "collective state" of the carrier ensemble, is represented by the distribution function $f(\boldsymbol{r},\boldsymbol{v},t)$. By definition, the quantity $f(\boldsymbol{r},\boldsymbol{v},t)d^3rd^3v$ is the average number of carriers at time t with center of mass within $(\boldsymbol{r},\boldsymbol{r}+d\boldsymbol{r})$ and velocity within $(\boldsymbol{v},\boldsymbol{v}+d\boldsymbol{v})$. Therefore, knowledge of the distribution function permits evaluation of all relevant macroscopic quantities that are associated with the carrier ensemble.

A typical carrier trajectory can be described as follows: the carrier moves (in real space) with an initial velocity, it is accelerated by external fields,

[5]The phonon, is a quasi particle corresponding to the quantum of lattice vibration.

[6]Only intravalley scattering mechanisms are considered here, in keeping with the single-valley assumption. Specifically, deformation-potential acoustic, nonpolar optic, and polar optic phonon scattering will be modeled [7–10].

[7]For convenience, the term "phase space" will apply to either velocity or momentum representations.

and then it is instantaneously scattered to another velocity state. With this picture in mind, conservation of carriers in an infinitesimal phase-space volume implies

$$\frac{\partial f}{\partial t} = -\nabla_r \cdot (\boldsymbol{v} f) - \nabla_p \cdot (\boldsymbol{F} f) + C f, \tag{1.1}$$

where $\boldsymbol{F}$ is the force due to external fields,[8] $\boldsymbol{p}$ is momentum, and C is a collision operator. Equation (1.1) is known as the Boltzmann transport equation and is written in a form suitable for semiconductor device simulation. In terms of velocity coordinates and an external electric field $\boldsymbol{E}(\boldsymbol{r},t)$, the BTE becomes

$$\frac{\partial f}{\partial t} = -\boldsymbol{v} \cdot \nabla_r f - \frac{q\boldsymbol{E}}{m^*} \cdot \nabla_v f + C f. \tag{1.2}$$

where q is the charge of the carrier (negative for electrons). Equation (1.2), neglecting the collision term for now, is a linear, first-order, partial differential equation. The BTE is defined on the seven-dimensional $(\boldsymbol{r}, \boldsymbol{v}, t)$ domain; hence, it is generally very difficult to solve.

The collision term Cf can be calculated through use of the scattering-probability-rate function $S(\boldsymbol{v}, \boldsymbol{v}')$. Application of local carrier conservation in phase space yields the following formula[9]:

$$Cf = \int d^3v' \; f(\boldsymbol{r}, \boldsymbol{v}', t) S(\boldsymbol{v}', \boldsymbol{v}) - \lambda(\boldsymbol{v}) f(\boldsymbol{r}, \boldsymbol{v}, t). \tag{1.3}$$

Here,

$$\lambda(\boldsymbol{v}) = \int d^3v' \; S(\boldsymbol{v}, \boldsymbol{v}'), \tag{1.4}$$

and is called the total scattering probability rate. The first term on the right side of (1.3) refers to "in-scattering ", since it describes scattering into $(\boldsymbol{r}, \boldsymbol{v})$ from other phase-space points. Similarly, the second term refers to "out-scattering", since it describes scattering out from $(\boldsymbol{r}, \boldsymbol{v})$ to other phase-space points. The BTE is therefore a linear integrodifferential equation upon inclusion of the collision term.

[8] Here, $\boldsymbol{F}$ may represent the influence of electric as well as magnetic fields.

[9] All integrations are performed over the infinite velocity domain. Also, carriers are assumed to obey nondegenerate statistics, and $S(\boldsymbol{v}, \boldsymbol{v}')$ is assumed to have no implicit spatial dependence.

1.1.2 The BTE and Device Simulation

Device simulation using the BTE introduces a variety of complications. The BTE must be made consistent with Poisson's equation.[10] Coupling is achieved through the electric field term of Eq. (1.2) and the charge-density term of Poisson's equation.[11] Unfortunately, the BTE-Poisson system is inherently nonlinear; thus special solution methods are required.

One more complication relating to device simulation is the prescription of boundary conditions. These conditions pertain to Poisson's equation as well as the BTE. Poisson's equation usually requires Dirichlet, Neumann, or mixed conditions along spatial boundaries [34]. These boundaries usually correspond to device electrodes, free surfaces, or perhaps internal symmetry regions. Unlike Poisson's equation, boundary conditions for the BTE are not frequently discussed and therefore will be elaborated upon here. The boundary conditions are imposed throughout the hyper-dimensional surface that encloses the phase-space domain. The distribution function is expected to vanish at "large-velocity" surfaces,

$$\lim_{v\to\infty} f(\boldsymbol{r},\boldsymbol{v},t) = 0. \tag{1.5}$$

Surfaces that include spatial boundaries involve various conditions. Two more common ones are injective and reflective boundary conditions. The injective boundary condition requires specification of the distribution function over an injecting surface,

$$f(\boldsymbol{r}_s,\boldsymbol{v},t) = g(\boldsymbol{r}_s,\boldsymbol{v},t), \quad \boldsymbol{v}\cdot\hat{\boldsymbol{n}}_s < 0. \tag{1.6}$$

Vectors $\boldsymbol{r}_s$ and $\hat{\boldsymbol{n}}_s$ refer to spatial points on the injecting surface and their corresponding outwardly directed unit normals, respectively. Injective conditions are applied in connection with "free-flow" boundaries. The reflective boundary condition requires that the distribution function possess even velocity parity normal to the reflecting surface,

$$f(\boldsymbol{r}_s, v_{ts}, v_{ns}, t) = f(\boldsymbol{r}_s, v_{ts}, -v_{ns}, t) \tag{1.7}$$

[10]Frequencies of operation are assumed small enough to neglect electromagnetic effects. Only quasi-electrostatic phenomena need be considered.

[11]Solution of Poisson's equation, $\nabla_r^2\psi = -(qn+Q_I)/\epsilon$, where n is the carrier concentration and Q_I is the net charge density due to ionized impurities and other crystalline defects, permits evaluation of the electric field, $\boldsymbol{E} = -\nabla_r\psi$, while solution of the BTE permits evaluation of the carrier density, $n = \int d^3v\, f$.

where $\boldsymbol{v}_{ts} = \hat{\boldsymbol{n}}_s \times (\boldsymbol{v} \times \hat{\boldsymbol{n}}_s)$ is the tangential component of $\boldsymbol{v}$ at position $\boldsymbol{r}$ and $v_{ns} = \hat{\boldsymbol{n}}_s \cdot \boldsymbol{v}$ is the normal component. Condition (1.7) can be modified for partially reflecting situations. The boundary condition then becomes

$$f(\boldsymbol{r}_s, \boldsymbol{v}_{ts}, v_{ns}, t) = \Gamma(v_n) f(\boldsymbol{r}_s, \boldsymbol{v}_{ts}, -v_{ns}, t) \tag{1.8}$$

In the absence of any boundary carrier generation the reflection function must obey $0 < \Gamma \leq 1$. The exact form of the reflection function Γ depends on the physical nature of the boundary.

The BTE-Poisson system is, in general, first-order time dependent so that an initial condition is necessary. Solution of time-independent systems through steady-state evolution of a pseudo-transient[12] also requires an initial condition. Mathematically, the initial condition can be expressed

$$f(\boldsymbol{r}, \boldsymbol{v}, t_o) = h(\boldsymbol{r}, \boldsymbol{v}), \tag{1.9}$$

where $h(\boldsymbol{r}, \boldsymbol{v})$ is the distribution function at initial time t_o.

1.1.3 Assumptions of Quasi-Classical Transport

It is informative to examine some of the assumptions which validate quasi-classical transport theory. Space-dependent quantities (lattice inhomogeneities and electric fields) must vary slowly on a length scale of several lattice constants. The distribution function, electric field, and boundary conditions are not permitted to vary significantly during a collision-interaction time or along a collision-interaction length.[13] Moreover, the energy absorbed by carriers during acceleration by the electric field is limited to the width of the carrier energy band. Assumptions pertaining to phonon scattering also exist. The phonon population is assumed near thermal equilibrium despite collisions with nonthermal carriers. The collision process is assumed to conserve carrier spin. As a final note, the carrier-phonon ensemble is assumed to be in a state of "molecular chaos". Thus, statistical correlations between the initial quasi momenta[14] of colliding particles are ignored.

[12]This procedure is will be discussed later in Chapters 2 and 4.

[13]This agrees with the concept that collisions are instantaneous—the elapsed time between collisions is much greater than the collision interaction time.

[14]Crystal momentum is conserved during collisions only to within an integral multiple of $\hbar\boldsymbol{K}$ (taking into account the phonon quasi momentum), where $\boldsymbol{K}$ is a reciprocal lattice vector. Collisions that involve nonsero multiples (Umklapp processes) will be ignored. For further discussion of this topic see reference [6].

1.2 Solution of the BTE

1.2.1 Conventional Methods

Numerous approaches have been used to solve the BTE in device structures. Many approaches implement simplifying approximations, yet almost all are numerical in nature because of mathematical complexity.

The simplest and most widely known approach is drift-diffusion theory [11]. Carrier collisions are modeled by means of a relaxation time. The main result of this theory is that the carrier current density can be written as

$$J(r,t) = |q|\mu n(r,t)E(r,t) - qD\nabla_r n(r,t), \tag{1.10}$$

where n is the carrier concentration, μ is the mobility, and D the diffusivity, with the latter two quantities being derived from the theory. Device simulation is carried out by solving Eq. (1.10) in conjunction with the continuity and Poisson equations. This theory works best when the deviation of the actual carrier distribution function from equilibrium is relatively small and ballistic effects (pertaining to collisionless or nearly collisionless situations) are negligible.[15]

A more sophisticated approach to solving the BTE involves parameterization of the distribution function. For example, the distribution function is often approximated by a displaced and heated Maxwellian [5]:

$$f(r,v,t) \sim n(r,t)\exp(-\delta v^T \beta \delta v), \tag{1.11}$$

in which the column vector $\delta v = v - v_d(r,t)$, δv^T denotes matrix transpose of δv, and β is the inverse temperature matrix with elements $\{\beta\}_{ij} = m^*/2k_B T_{ij}(r,t)$. Approximation (1.11) is then substituted into the BTE and successive moments are evaluated. The resulting equations for n, v_d, and β—corresponding to mass, momentum, and energy conservation—are then solved along with Poisson's equation. The validity of this technique becomes questionable when the distribution function is poorly described by (1.11), as in ballistic systems or those with highly anisotropic scattering.

[15] A necessary condition for validity of drift-diffusion theory is that typical carrier velocities must be small compared with the thermal velocity, $v_{th} \sim (k_B T/m^*)^{1/2}$. As a rule, drift-diffusion theory is valid for length scales greater than the mean free path and times scales greater than the mean collision time.

Another common technique is the Monte Carlo method [9]. Device simulation is accomplished through tabulation of phase-space carrier trajectories. Scattering events are determined by random-number generation based on actual scattering-probability-rate functions. Poisson's equation can be included in the simulation procedure. Data storage requirements are extremely large and certain scattering mechanisms, such as carrier-carrier, are difficult to handle. Moreover, statistical convergence is slow; yet, the Monte Carlo method is favored by many because of its simplicity and ease of implementation.

Other solution procedures also exist: momentum- and energy-dependent relaxation-time methods, iterative integral methods, and direct integration methods, to name a few [7,12,13].

1.2.2 The Spectral Method

The method of weighted residuals is the general approximation technique that will be used to solve the BTE in this work [14]. This method finds application in a wide variety of numerical problems and is closely related to the finite-element and Rayleigh-Ritz (variational) methods [15,16].

The method of weighted residuals has been successfully implemented in various fields, ranging from fluid flow, heat and mass transfer, chemical-reaction systems to analysis of mechanical structures and nuclear-reactor simulation [14,17]. Specifically, the type of weighted-residual method that will be dealt with here is known as a spectral method [16].[16] This method can be used to solve differential (ordinary and partial) and integrodifferential equations, linear and nonlinear. The principle behind the spectral method is that the solution of the governing equation can be approximated with a linear combination of "basis functions". These functions, composing a basis set, are defined over the entire domain of interest. The choice of basis functions is an important consideration; it is desirable to choose successive elements of a mathematically complete set. The calculation of the basis function expansion coefficients, α_n, $n = 1, \ldots, N$, proceeds by substituting the basis function expansion into the governing equation, which in generalized space

[16]Throughout the literature other names are in frequent use: eigenfunction or global expansion, modal, and Rits-Galerkin.

and operator notation can be written as $\mathcal{O}y(\boldsymbol{x}) = 0$. Hence,

$$\mathcal{O}\sum_{n=1}^{N}\alpha_n\Phi_n(\boldsymbol{x}) = R(\boldsymbol{x}) \tag{1.12}$$

where $\boldsymbol{x}$ has dimensionality s, the functions Φ_n are elements of the basis set,[17] and the quantity R is called the residual. Equations can be developed for the α_n by forcing the integrated residual to vanish for N different weighting functions, w_n:

$$\int d^s\boldsymbol{x}\; w_n(\boldsymbol{x})R(\boldsymbol{x}) = 0, \tag{1.13}$$

$$n = 1, \cdots, N.$$

Here, the integration is to be performed over the entire $\boldsymbol{x}$ domain. Standard residual-weighting procedures, as defined by selection of weighting functions, have been established. The more common methods are the collocation (pseudospectral), where $w_n = \delta(\boldsymbol{x} - \boldsymbol{x}_n)$; the Galerkin, where $w_n = \Phi_n(\boldsymbol{x})$; and the least-square, where $w_n = \mathcal{O}\Phi_n(\boldsymbol{x})$ [14,16]. In theory, the residual is expected to vanish throughout its domain as $N \to \infty$, and thus the method becomes exact. This property is ensured if the basis functions constitute a mathematically complete set. Note that it is computationally advantageous to use an orthogonal (or "nearly orthogonal") basis set.

The distinct advantage of the spectral method is its mathematical compactness. Frequently, sufficient accuracy can be maintained while keeping the total number of basis functions reasonably small. These "low-order" expansions result in substantial reduction of computational effort. Hence, the spectral method is particularly useful when the spectral content of the solution is limited.[18]

1.2.3 Spectral Solution of the BTE

Actual implementation of the spectral method is slightly more complicated than what has so far been discussed. But before delving into details of the proposed method it is useful to review the closely related work of Rees.

[17] It is presently assumed, for simplicity, that each basis function satisfies the appropriate boundary conditions.

[18] These considerations aside, the spectral method is generally quite accurate. For example, the spectral method typically requires a factor of two to ten fewer degrees of freedom (unknowns) than the popular finite-difference method [16,18].

Rees has developed a numerical simulation procedure to model the Gunn effect in GaAs diodes [4,19]. The simulation procedure directly solves the BTE along with Poisson's equation. Rees's starting point was the assertion that the distribution function can be approximated with the series expansion,[19]

$$f(\boldsymbol{r},\boldsymbol{v},t) \approx \sum_{n=1}^{N} \alpha_n(\boldsymbol{r},t)\Phi_n(\boldsymbol{v}). \tag{1.14}$$

The basis functions Φ_n were obtained from previously calculated numerical solutions of the time-independent, spatially homogeneous BTE for a series of electric-field strengths. Rees then formulated an elaborate numerical scheme to calculate the expansion coefficients α_n. It was found that approximately eighteen basis functions were sufficient to achieve five-percent accuracy in calculating average carrier velocities.

Although Rees was able to significantly reduce computational effort, several important limitations, which relate to generalization and applicability, have not been resolved. For instance, the time-stepping algorithm requires weak variation of the distribution function over a mean free path,[20] a severe constraint when attempting to simulate ballistic systems. Also, extension of the method to systems of higher dimensionality is not easily effected.

In light of the work by Rees, the spectral method used here is predicated upon the expansion (1.14). A numerical algorithm is developed by substituting the expansion into the BTE. The spatial and temporal dependence of the expansion coefficients is treated using the method of finite differences [15]. A residual-weighting procedure, in velocity, is then carried out to determine the expansion coefficients. This method can be regarded as a hybrid between the finite-difference and spectral methods, and hereafter will be called the FD-spectral method.

---

[19]The independent variables for this cylindrically symmetric problem were (z, v_ρ, v_z, t).

[20]Rees has claimed that time steps could be taken at least as large as the mean carrier collision time, $\Delta t \sim \tau_c$. In addition, numerical stability is ensured only if the spatial discretization length is large compared to the distance traveled by carriers during a single time step Δt (see Appendix B): $\Delta x \gg \bar{v}\tau_c$, where $\bar{v}$ is the mean carrier velocity. Hence, space-dependent quantities (the distribution function included) must vary weakly over a mean free path $\ell_{mfp} \sim \bar{v}\tau_c$.

1.3 Thesis Scope

This work's primary goal is to establish and test a new algorithm for direct solution of the BTE in semiconductor device structures. All analyses will be carried out for the time-independent case; quasi-classical scattering will be included. A single spherical, parabolic band will be assumed and only monopolar (electron) transport will be described. Solution of the Poisson-BTE system will not be attempted; thus *a priori* specification of the electric field will be necessary.

The specific objectives of this work fall into three categories:

- The development of an FD-spectral algorithm, with particular attention to the choice of basis functions, residual-weighting procedures, and finite-differencing schemes.
- The establishment of a numerical solution procedure for the resultant FD-spectral equations. Direct and iterative methods will be examined.
- Analysis of the numerical behavior of the FD-spectral method, including issues pertaining to stability, accuracy, data storage, and execution speed.

The thesis is organized in four subsequent chapters. Chapter 2 deals with preliminary numerical calculations. Two proven methods for direct solution of the BTE are chosen: an iterative integral method and a finite-difference method. Calculations are performed for simple problems to gain familiarity in solving the BTE; issues relating to the collision operator and numerical behavior of quasi hyperbolic equations are investigated. Chapter 3 focuses on solution of the low-dimensionality[21] BTE by means of the FD-spectral method. Simulations of various one-dimensional device structures are accomplished by direct Gaussian elimination of the FD-spectral equations. Chapter 4 concerns solution of the high-dimensionality BTE by means of the FD-spectral method. An iterative pseudo-transient method is presented to simulate transport in a two-dimensional transversally periodic and mirror-symmetric device structure. Finally, Chapter 5 concludes the thesis with a summary of important results and an assessment of the FD-spectral method. That chapter ends with a discussion of numerous modifications and extensions of the FD-spectral method.

[21] "Low-dimensionality" refers to the (r,v,t) domain

Chapter 2

Preliminary Numerical Calculations

Investigative numerical calculations have been performed to gain familiarity in solving the BTE. These calculations are vital for formulation of the FD-spectral method even though they involve established solution methods. The BTE, as pointed out in the previous chapter, is a linear integrodifferential equation. Without the collision term, this equation becomes a standard hyperbolic partial differential equation, first order in space, velocity, and time. Numerical solution of hyperbolic equations is extensively discussed in the literature, especially for problems of low dimensionality [20,21].[1] The collision term, however, complicates the solution of the BTE in two ways. First, the collision term usually requires a series of integrations over the velocity domain, an arduous numerical task. And second, the mere existence of the collision term removes the BTE from the well-understood hyperbolic class of differential equations. Preliminary numerical calculations presented in this chapter provide information concerning the behavior of typical carrier distributions in semiconductors as well as "benchmark" solutions that can be compared with FD-spectral solutions of Chapters 3 and 4.

The preliminary numerical calculations implement two proven solution methods: the finite-difference method and the Rees integral method. Each method is well suited for solution of the low-dimensionality BTE, but only the integral method can take into account the effects of a physically realistic collision term. The finite-difference method is easier to apply when solving

[1] That is, involving one through three independent variables, not counting time.

ballistic problems or when solving problems where the collision term does not involve explicit integration [see, for example, collision term (2.35)]. The Rees integral method will be used to solve the space-independent, time-dependent BTE with cylindrical velocity symmetry, the (v_ρ, v_z, t) problem, whereas the finite-difference method will be used to solve the space- and time-dependent BTE with a single velocity variable, the (x, v_x, t) problem. Independent variable sets for these test problems have been chosen to facilitate numerical implementation[2] and provide reasonably realistic results.

2.1 The (v_ρ, v_z, t) Problem

Under certain circumstances the BTE may become space independent. One such case is when the electric field is z directed, spatially uniform, although possibly time dependent: $\boldsymbol{E} = E_z(t)\hat{\boldsymbol{e}}_z$. The distribution function is then cylindrically symmetric and depends on three independent variables, $f = f(v_\rho, v_z, t)$. Variation with velocity polar angle coordinate ϕ does not occur.[3] Explicitly, the BTE for this spatially uniform problem is

$$\frac{\partial f}{\partial t} = -\frac{qE_z}{m^*}\frac{\partial f}{\partial v_z} + Cf. \tag{2.1}$$

2.1.1 The Rees Integral Method

2.1.1.1 Velocity Discretization

Equation (2.1) can be solved by an iterative integral method. The method used here has been developed and verified by Rees [12].[4] The Rees integral

[2] In particular, computer variable storage, execution rate, and program coding issues were addressed.

[3] This can be understood by examining individual carrier trajectories. The spatially uniform electric field points in the z direction and can only perturb the z component of velocity, v_z. Collision processes scatter carriers with rotational uniformity about the collision axis (see Appendix E). The distribution function can vary only in v_ρ and v_z, not ϕ. This symmetry can be proved rigorously by examining the invariance of the BTE to rotations about the v_z axis.

[4] This method should not be confused with the more general one discussed in Chapter 1, developed for solving the space-dependent BTE.

method uses a standard velocity discretization in which the continuous velocity variable, $v = v_\rho \hat{e}_\rho + v_z \hat{e}_z$, is transformed as follows:

$$f(v,t) \longrightarrow f_{ij}(t), \tag{2.2}$$

$$\begin{aligned} v_{\rho i} &= (i-1)\Delta v_\rho, \\ v_{zj} &= v_{zo} + j\Delta v_z, \\ i &= 1, \cdots, L, \\ j &= 1, \cdots, M. \end{aligned}$$

The discrete velocity domain $v_{ij} = v_{\rho i}\hat{e}_\rho + v_{zj}\hat{e}_z$ constitutes a uniform mesh with LM cells centered at $(v_{\rho i}, v_{zj})$ of size Δv_ρ by Δv_z. Since the collision term entails a continuous integration over velocity variables, the collision operator appropriately transforms into a discrete collision operator,

$$Cf \longrightarrow \sum_{i'j'} C_{iji'j'} f_{i'j'}(t). \tag{2.3}$$

The discrete collision operator $C_{iji'j'}$ operates only on the dummy velocity indices i' and j', and numerically approximates the continuous mathematical operations entailed in Cf.

2.1.1.2 Time Discretization

Time is discretized, like velocity, by introducing a discrete time variable h:

$$f_{ij}(t) \longrightarrow f_{ij}^h, \tag{2.4}$$

$$\begin{aligned} t_h &= t_o + \sum_{u=1}^{h} \Delta t^u, \\ h &= 0, 1, 2 \cdots. \end{aligned}$$

The quantity t_h corresponds to a discrete time sample after initial time t_o; the time step Δt^h can be made variable for each time sample as indicated by the superscript h. The Rees integral method also requires time discretization of the electric field,

$$E_z(t) \longrightarrow E_z^h. \tag{2.5}$$

2.1.1.3 The Rees Equations

Figure 2.1 depicts the velocity discretization mesh over which iterative computations are performed. For practicality, the velocity domain is made finite and is enclosed with boundary cells.[5] Cells not on the boundary are denoted internal cells.

Only the results of Rees's method will be presented here since a complete derivation is lengthy and can be found in Rees's original paper [12]. As discussed in Appendix A, the method breaks down into two iterative steps which are carried out at each internal mesh point. The first step describes the influence of collisions. An intermediate array g_{ij}^h is calculated:

$$g_{ij}^h = (\Delta t^h)^{-1} f_{ij}^h + \sum_{i'j'} C_{iji'j'} f_{i'j'}^h, \tag{2.6}$$

$$i = 1, \cdots, L-1,$$
$$j = 2, \cdots, M-1.$$

In the second step, which describes the additional influence of the electric field, g_{ij}^h is used to calculate the distribution function after a time step Δt^h:

$$\begin{aligned} f_{ij}^{h+1} &= \exp\left[-\frac{m^*}{qE_z^h \Delta t^h}(v_{zj} - v_{zj-1})\right] f_{ij-1}^{h+1} \\ &+ \frac{m^*}{qE_z^h} \exp\left(-\frac{m^*}{qE_z^h \Delta t^h} v_{zj}\right) \sum_{\mu=j-1}^{j} w_\mu g_{i\mu}^h. \end{aligned} \tag{2.7}$$

The summation derives from numerical evaluation of a continuous integral as detailed in Appendix A.2. In this case, a variant of standard trapezoidal integration is used with sample weights w_μ [see formulas (A.12) and (A.13)].

Boundary mesh points are handled differently. In accordance with the discussion of Section 1.1.2, the proper boundary condition for this problem is that the carrier distribution must vanish at each boundary node. No iteration is therefore necessary at boundary mesh points and the distribution function is set to zero for all time samples:

$$f_{ij}^h = 0, \tag{2.8}$$

[5]The boundary encloses a large enough region to minimize artificial "edge effects".

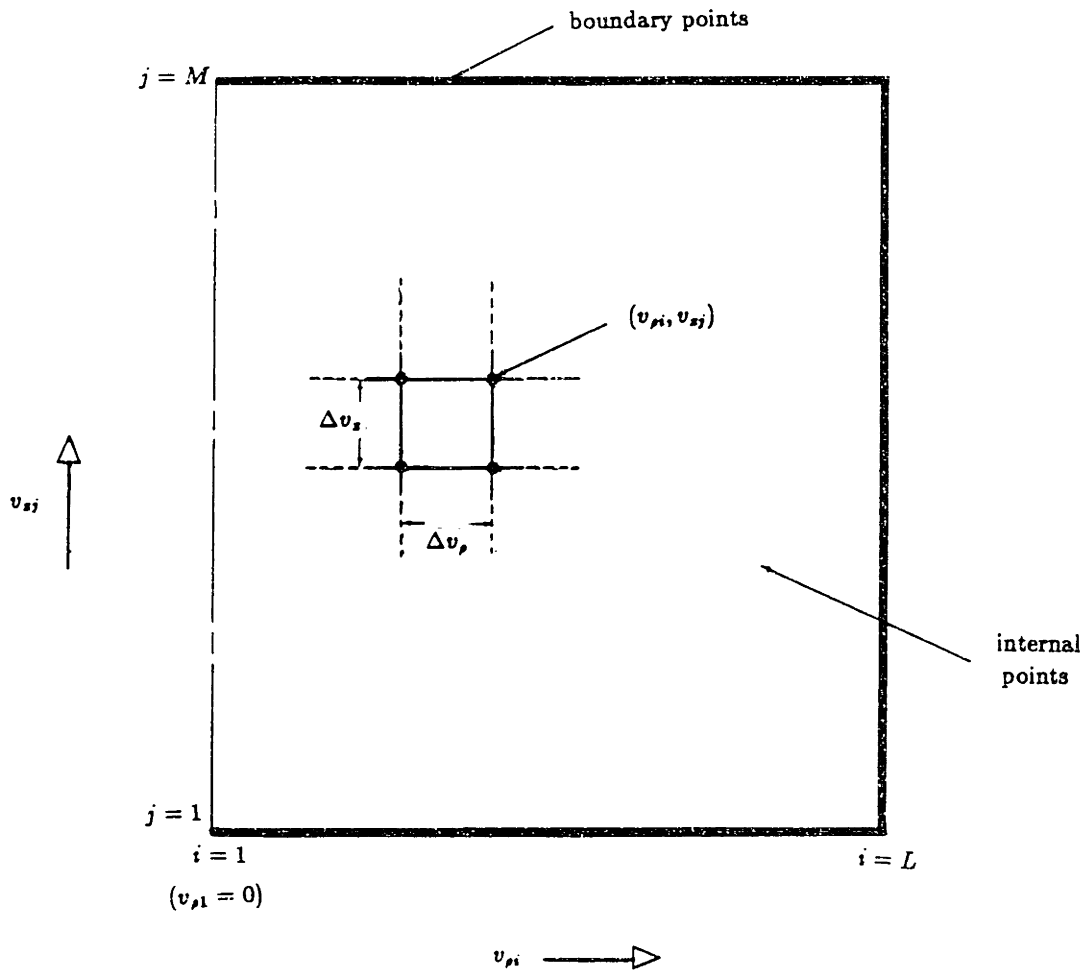

Figure 2.1. Velocity discretization mesh for the (v_ρ, v_z, t) problem.

$$h = 0, 1, 2, \cdots,$$
$$i = 1, \cdots, L, \quad j = 1, M,$$
$$i = L, \quad j = 1, \cdots, M.$$

Presentation of the Rees integral method would not be complete without discussion of initial conditions. Initial conditions establish the starting point for subsequent iteration. A natural choice is the equilibrium Maxwellian,

$$f_{ij}^0 = f_o(v_{ij}) = \mathcal{N} \exp\left(-\frac{m^*}{2k_B T} v_{ij}^2\right). \tag{2.9}$$

$$i = 1, \cdots, L-1,$$
$$j = 2, \cdots, M-1.$$

This initial distribution must be normalized to yield a desired carrier concentration through specification of the normalization constant $\mathcal{N}$.[6] Initial condition (2.9) is appropriate for many applications involving time-dependent calculations of systems initially near equilibrium. Other initial conditions may be expedient when the initial transient is irrelevant, as in steady-state calculations. An initial condition obtained from a previous, closely related calculation can greatly enhance steady-state computation time, for example.

2.1.2 The Collision Term

2.1.2.1 Polar-Optic Phonon Scattering Rates

For the present problem a single phonon scattering mechanism, polar optic, has been selected. Polar-optic phonon scattering arises from the electric polarization associated with lattice atoms. Polar-optic phonon scattering is the dominant scattering mechanism in the central Γ valley of gallium arsenide[7] and was selected primarily for sake of physical realism. A brief

[6] By definition of the distribution function the normalization constant $\mathcal{N}$ and the carrier concentration n are related as follows: $\mathcal{N} \int_{-\infty}^{\infty} \int_0^{\infty} \int_0^{2\pi} d\phi dv_\rho dv_z \, v_\rho \exp(-m^* v^2/2k_B T) = n$. Upon integration, $\mathcal{N}(2\pi k_B T/m^*)^{3/2} = n$. It should also be mentioned that the velocity discretization mesh is chosen large enough to make (2.9) nearly zero close to boundary mesh points [$v_{\rho L}, |v_{z1}|, |v_{zM}| \gg (2k_B T/m^*)^{1/2}$], and therefore consistent with (2.8).

[7] At extremely low temperatures of a few degrees kelvin acoustic phonon scattering becomes important.

discussion along with a derivation of this, and other, phonon scattering rates can be found in Appendix E ; Section E.4 treats polar-optic phonon scattering, where the scattering probability rate is shown to be [Eq. (E.24)]

$$S_{po}(\boldsymbol{v},\boldsymbol{v}') = \frac{m^* q^2 \omega_\ell (\epsilon_\infty^{-1} - \epsilon_o^{-1})}{8\pi^2 \hbar |\boldsymbol{v}-\boldsymbol{v}'|^2} \begin{cases} N_\ell \delta(\varepsilon' - \varepsilon - \hbar\omega_\ell) & \text{(absorption)} \\ (N_\ell + 1)\delta(\varepsilon' - \varepsilon + \hbar\omega_\ell) & \text{(emission).} \end{cases} \tag{2.10}$$

Quantities $\hbar, \epsilon_o, \epsilon_\infty$, and ω_ℓ are Planck's constant, the static and high-frequency dielectric constants, and the longitudinal-optic-phonon frequency, respectively. The parameter N_ℓ is the Bose-Einstein occupancy factor corresponding to a phonon energy $\hbar\omega_\ell$: $N_\ell = [\exp(-\hbar\omega_\ell/kT) - 1]^{-1}$. The functions ε and ε' are simply initial and final carrier kinetic energies, $m^* v^2/2$ and $m^*(v')^2/2$. Equation (2.10) contains expressions for phonon absorption and emission processes.

Polar-optic scattering is inelastic; initial and final carrier energies are not identical but differ by the phonon energy $\hbar\omega_\ell$.[8] Furthermore, the scattering is anisotropic. In other words, the scattering rate varies with angle between initial and final carrier velocity vectors.[9]

The total scattering probability rate due to polar-optic phonons is found upon integration of (2.10) over all possible final states $\boldsymbol{v}'$ [Eq. (E.27)]:

$$\lambda_{po}(\varepsilon) = \frac{(m^*)^{1/2} q^2 \omega_\ell (\epsilon_\infty^{-1} - \epsilon_o^{-1})}{4\sqrt{2}\pi\hbar\sqrt{\varepsilon}} \times \begin{cases} N_\ell \ln \left| \dfrac{\sqrt{\varepsilon}+\sqrt{\varepsilon+\hbar\omega_\ell}}{\sqrt{\varepsilon}-\sqrt{\varepsilon+\hbar\omega_\ell}} \right| & \text{(absorption)} \\ (N_\ell + 1) \ln \left| \dfrac{\sqrt{\varepsilon}+\sqrt{\varepsilon-\hbar\omega_\ell}}{\sqrt{\varepsilon}-\sqrt{\varepsilon-\hbar\omega_\ell}} \right| u(\varepsilon - \hbar\omega_\ell) & \text{(emission).} \end{cases} \tag{2.11}$$

Observe that the total scattering-probability rate is a function of initial energy or, equivalently, the magnitude of initial velocity. Phonon emission contributes to total scattering only when carriers have initial energy greater than the phonon energy, as is ensured by the unit step function $u(\varepsilon - \hbar\omega_\ell)$.[10]

[8] The delta functions of in (2.10) are nonsero only when $\epsilon - \epsilon' = \pm\hbar\omega_\ell$.

[9] This property is manifested from the presence of the anisotropy term $|\boldsymbol{v} - \boldsymbol{v}'|^{-2}$ in (2.10). Note, too, that low-angle scattering is strongly favored.

[10] Carrier-phonon scattering is characterized by two conservation rules. Conservation of

2.1.2.2 The Collision Operator

According to Eqs. (1.3) and (1.4) the collision term, as expressed by the action of a collision operator on the distribution function, consists of in- and out-scattering contributions. Upon integration over the symmetry variable ϕ, the action of the continuous collision operator can be expressed as

$$\begin{aligned} Cf &= \int_{-(v^2-v_\ell^2)^{1/2}}^{(v^2-v_\ell^2)^{1/2}} d\xi\ f(\sqrt{v^2-v_\ell^2-\xi^2},\xi,t)\,S_{po}^{-}(\xi,v) \\ &+ \int_{-(v^2+v_\ell^2)^{1/2}}^{(v^2+v_\ell^2)^{1/2}} d\xi\ f(\sqrt{v^2+v_\ell^2-\xi^2},\xi,t)\,S_{po}^{+}(\xi,v) \\ &- \lambda_{po}^{-}(\varepsilon)f(v,t) - \lambda_{po}^{+}(\varepsilon)f(v,t), \end{aligned} \tag{2.12}$$

where $v_\ell = (2\hbar\omega_\ell/m^*)^{1/2}$ is the carrier velocity corresponding to the longitudinal-optic-phonon energy. Absorption and emission components have been linearly combined, and scattering probability rates S_{po}^{-} and S_{po}^{+} have been cast in cylindrical coordinates. Refer to Appendix E for a complete derivation of the in-scattering contributions in (2.12) [Eqs. (E.28) through (E.30)]. Total scattering probability rates λ_{po}^{-} and λ_{po}^{+} are given by the absorption $(-)$ and emission $(+)$ entries of (2.11).

In order to implement Rees's integral method the collision operator must be converted to discrete form. Numerical evaluation of (2.12) is conveniently carried out using the trapezoidal rule [15]. Quantities between mesh points are approximated via linear interpolation (see Section C.1). Thus, the collision term takes the form

$$\begin{aligned} \sum_{i'j'} C_{iji'j'} f_{i'j'}^{h} &= \sum_{\mu} w_\mu S_{po}^{-}(v_{z\mu}, v_{ij})\{w^{-}(\mu) f_{\mu\nu-(\mu)}^{h} + [1-w^{-}(\mu)] f_{\mu\nu-(\mu)+1}^{h}\} \\ &+ \sum_{\mu} w_\mu S_{po}^{+}(v_{z\mu}, v_{ij})\{w^{+}(\mu) f_{\mu\nu+(\mu)}^{h} + [1-w^{+}(\mu)] f_{\mu\nu+(\mu)+1}^{h}\} \\ &- \lambda_{po}^{-}(\varepsilon_{ij}) f_{ij}^{h} - \lambda_{po}^{+}(\varepsilon_{ij}) f_{ij}^{h}, \end{aligned} \tag{2.13}$$

for which $\varepsilon_{ij} = m^* v_{ij}^2/2$ and w_μ are the trapezoidal integration weights. Sum limits are specified through correspondence with integral limits in (2.12)

---

emission. Conservation of momentum states that initial and final carrier-phonon momentum is preserved to within a reciprocal lattice vector (see footnote 14, Chapter 1): $m^*\boldsymbol{v} = m^*\boldsymbol{v}' \pm \hbar\boldsymbol{q} + n\hbar\boldsymbol{K}$, $n = 0, 1, 2, \cdots$, where $\hbar\boldsymbol{q}$ is the phonon quasi momentum. Phonon quasi momentum and energy are connected through a dispersion relation $\omega = \omega(q)$ for the type of phonon involved. See reference [6] for further elaboration.

(which may necessitate additional interpolation). Linear interpolation weighting fractions, w^- and w^+, as well as discrete distribution indices, ν^- and ν^+, are all functions of summation variable; their dependencies are likewise determined through correspondence with (2.12).

2.1.3 Numerical Implementation

2.1.3.1 Velocity Discretization Mesh

Equations (2.6) and (2.7), which define the Rees integral method, have been solved by iterative scanning over a velocity mesh. In this study the velocity mesh comprises fixed, uniform rectangular cells; the distribution function f_{ij}^h corresponds to the velocity mesh point $(v_{\rho i}, v_{zj})$ (see Fig. 2.1). The largest mesh used in actual simulations was $L = 40, M = 80$.

2.1.3.2 Solution of the Rees Equations

At each internal point on the velocity discretization mesh a two-step iteration must be performed in order to advance the the distribution function a single time step Δt^h. A single scan constitutes two separate "sub-scans", one for (2.6) and another for (2.7). Boundary mesh points require no iteration. A "Gauss-Siedel" time-stepping algorithm has been found to yield favorable results. The algorithm simply requires replacement of f_{ij}^h by f_{ij}^{h+1} on a point by point basis [that is, over $(v_{\rho i}, v_{zj})$ as soon as f_{ij}^{h+1} is calculated]. For small time steps the difference compared with updating after each complete mesh scan—"Jacobi" time stepping—is miniscule. In fact, Gauss-Siedel time stepping saves on computer memory in that storage of temporary mesh arrays is not necessary. An additional benefit of Gauss-Siedel time stepping is good numerical stability because of its semi-implicit nature.[11]

[11] Explicit methods are characterised by iterations in which quantities for the next time step (f_{ij}^{h+1} in the present case) depend only on information obtained from previous time samples. Implicit methods, which are generally more stable but more difficult to implement, depend on information obtained from the current time sample. Semi-implicit methods depend on information obtained in part from the current time sample and in part from previous time samples. The method presented here can be shown to be semi-implicit, thus combining the ease of implementation associated with explicit methods and the increased stability associated with implicit methods. See reference [22] for additional information.

2.1.3.3 Numerical Stability

On account of the original BTE being quasi-hyperbolic, an overall constraint exists to ensure numerical stability during iterative solution. The constraint, known as the CFL (Courant-Friedrichs-Lewy) stability criterion, applies to all situations dealing with numerical solution of first-order hyperbolic or quasi-hyperbolic equations [20,21]. A full discussion of the CFL criterion is given in Appendix C; in simple, intuitive terms the constraint amounts to the statement that any "physical velocity" cannot exceed the "mesh velocity". For the specific problem at hand

$$\frac{|qE_x|}{m^*} \leq \frac{\Delta v_x}{\Delta t^h}. \tag{2.14}$$

Here, the physical velocity corresponds to the coefficients in the original BTE [Eq. (2.1)] that multiply gradient terms. The mesh velocity is obtained by dividing the increment in gradient variable by the time step. Criterion (2.14) asserts that specification of E_x and Δv_x sets an upper bound on the largest time step usable; using any larger time step will generate erroneous, ever-growing solutions.

Highly accurate calculations of time-dependent phenomena naturally require the use of small time steps. Using small time steps will result in large computation times. Unfortunately, this situation is inescapable for time-dependent calculations. Convergence to a steady state can be accelerated by means of pseudo-transient iteration, however. Initially, time steps are chosen large, but within stability limits, allowing the system to rapidly "equilibrate" to an approximate steady-state solution. The fact that this initial transient is of low accuracy (because of large Δt^h) is of no concern. Accuracy of the approximate steady-state solution can then be ameliorated if the time step is gradually decreased ($\Delta t^h \to 0$ as $h \to \infty$). Theoretically, vanishingly small time discretization error (see the next section) can be achieved as long as the time steps are made smaller and smaller. Steady-state solution of the Rees equations has been found to be ten to one-hundred times faster than the alternative fixed time-step iteration scheme.

To conclude this section, a discussion of the iterative velocity mesh scanning procedure is warranted. Iteration over the velocity mesh can occur in

stability associated with implicit methods. See reference [22] for additional information.

an infinity of scanning patterns.[12] Scanning in a left-to-right, top-to-bottom fashion has proved advantageous (refer to Fig. 2.1). First, numerical indexing (ij) of the scan pattern is trivial and thus computer coding is simplified. Second, and more important, left-to-right scanning allows calculation of (2.7) in a highly efficient manner. The time-wasting operation associated with performing the sums in (2.7) can be optimized by storing partial sums and merely adding a single term corresponding to the current mesh point. In actual practice, iterative scans involving (2.7) take a small fraction of time compared with those involving (2.6).

2.1.3.4 Numerical Errors

Numerical solution of differential equations introduces errors in the dependent variable, which arise from the finite-digit representation of numbers in computer systems– round-off error—and discretization of continuous variables—discretization error [15]. A complete analysis of the Rees integral method therefore entails a study of the two types of errors mentioned above.

Numbers stored in modern-day computers are usually represented by a set of binary digits, one set for storage of the mantissa and another for storage of the exponent. Each set comprises a finite number of binary digits. Thus mathematical operations cannot provide numerical results which require resolution beyond the least-significant binary digit of the mantissa (and the exponent, for that matter). These round-off errors are quantified by specifying the smallest quantity that can be added to unity the result of which can still be resolved. In this work, all calculations were performed on a computer system with a resolution of one part in ten million (single precision). Iterative solution of Rees's equations yields negligible round-off error because the error per mathematical operation is extremely small and each time step entails a relatively low number of mathematical operations which prevents excessive accumulation of round-off error.[13]

A more significant numerical error is discretization error. The discrete representation of continuous velocity and time variables and hence the carrier distribution is the essential starting point for Rees's integral method.

[12] As a reminder, scanning refers to a systematic sampling of all velocity mesh point to effect one single iterative time step of Eqs. (2.6) and (2.7).

[13] Round-off error can become a serious problem when numerous mathematical operations are involved, such as a long series of matrix-matrix multiplications.

It is difficult to obtain *a priori* knowledge of velocity increments and time steps $(\Delta v_\rho, \Delta v_z, \Delta t^h)$ which will result in acceptably small absolute error. Nevertheless, it is possible to self-consistently monitor relative discretization errors if a series of solutions is examined, each for smaller velocity and time steps. Monotonically decreasing velocity increments and the time step will ensure acceptably small absolute errors. Self-consistent error monitoring does, however, suffer from certain limitations. Decreasing velocity increments will result in an increase in computer variable storage; decreasing the time step will result in an increase in computation time (not to mention the possibility that a decrease in velocity increment may, on account of the CFL criterion, force use of an unmanageably small time step).

In practice, numerical errors have been found to accumulate during iteration of the Rees equations [12]. Unchecked, these errors will eventually lead to corruption of the desired solution. Normalization scaling can prevent unwanted accumulation. The principle behind this approach is that the total carrier concentration is expected to remain constant with time. Error correction is achieved through scaling the distribution function with an appropriate correction factor:

$$\varsigma = \frac{\sum_{ij} w_i w_j v_{\rho i} f_{ij}^0}{\sum_{ij} w_i w_j v_{\rho i} f_{ij}^h}. \tag{2.15}$$

The correction factor ς is easily calculated by double trapezoidal integration. It represents the ratio of original carrier concentration at initial time t_o $(h = 0)$ to error-corrupted carrier concentration.[14] Equation (2.15) needs to be applied only when ς is significantly different from unity; for example, calculations carried out in Section 2.1.4 have shown that tens of time steps may pass before ς varies by more than a few percent.

Numerical errors can also be responsible for generating completely unphysical, negative values for the distribution function. Occurrence of negative values prevails in regions where the distribution function is extremely small, typically those of large velocity magnitude. A simple corrective procedure has proved efficacious—"zero clipping". At the mesh point in question the distribution function is forced to zero whenever acceptance of the usual

[14]The appearance of $v_{\rho i}$ in (2.15) stems from the fact that the velocity volume element in cylindrical coordinates is $d^3v = v_\rho d\phi dv_\rho dv_z$. After integration over the symmetry variable ϕ, $d^3v = 2\pi v_\rho dv_\rho dv_z$; the factors of 2π have been canceled in writing (2.15).

iterative update would produce negative values; otherwise, the iteration proceeds according to (2.6) and (2.7).

2.1.4 Results and Discussion

2.1.4.1 Execution Rate

Calculations for this section, and, in fact, throughout this thesis, were performed on an Hewlett-Packard 1000F minicomputer. The HP-1000F executes at roughly five one-hundredths MFLOPS (million floating-point operations per second). Whenever possible, pseudo-transient iteration was performed to enhance calculation rates. Iteration of the Rees equations proceeded at approximately ten time step scans per second (error correction included) for a mesh size of $L = 40$, $M = 80$. Tests have shown that evaluation of collision term (2.13) dominates iterative calculation, so that calculation time is nearly proportional to the number of trapezoidal integration samples ($\sim L$).

2.1.4.2 Solution Verification

Verification of solutions generated from any numerical method is crucial, and sometimes tedious, especially when analytical solutions are unavailable. A sequence of tests was undertaken to establish validity of the numerical solutions. At first, ballistic tests (no collisions) were performed, whereby the time evolution of an initial equilibrium Maxwellian was studied. In this case a simple analytical expression for the carrier distribution, given in Eqs. (F.13) and (F.14) of Appendix F, is available for comparison. Good agreement was observed between numerical and exact solutions. Most errors were less than one-tenth of one percent after hundreds of time steps.

The next verification test was performed on the full BTE, collision term included. Proper installation of scattering-rate computer routines was checked through evaluation of the total scattering probability rate from $S(\boldsymbol{v}, \boldsymbol{v}')$ directly, using numerical integration [refer to Eq. 1.4], as well as comparison with results given by Fawcett for polar-optic phonon scattering [10]. Further, steady-state calculations of the velocity-field characteristic ($\bar{v}_z$ versus E_z) were compared with those obtained from Fawcett's Monte-Carlo method [10]. Even though Fawcett's calculations were for the multivalley gallium arsenide system, comparison was made over the pre-DNR (differential negative

Quantity	*Value*	*Units*
Carrier charge, q	1.62×10^{-19}	coulombs
Carrier effective mass, m^*	6.10×10^{-32}	kilograms
Boltzmann's constant, k_B	1.38×10^{-23}	joules/kelvin
Planck's constant, $\hbar$	1.06×10^{-34}	joule-seconds
Lattice temperature, T	300	kelvin
Static dielectric constant, ϵ_o	1.11×10^{-10}	farads/meter
High-frequency dielectric constant, ϵ_∞	9.58×10^{-11}	farads/meter
Longitudinal-optic phonon frequency, ω_ℓ	5.37×10^{13}	seconds^{-1}

Table 2.1: Physical parameters for Γ valley of gallium arsenide, with polar optic scattering.

resistance) region $|E_x| < 3$ kV/cm.

A final verification test, based on qualitative physical reasoning, was conducted. Solutions were checked for overall consistency of form: velocity and time variation in a mathematically smooth manner, agreement with initial and boundary conditions, and rapid "roll-off" for velocities beyond which polar-optic phonons are generated, $v > v_\ell$.

2.1.4.3 Numerical Solutions

Numerical calculations, employing Rees's integral method, have been successfully carried out. This section will present the results of a representative calculation.

Table 2.1 lists the physical parameters used in the calculation. Parameter values closely agree with the data available for the Γ valley of gallium arsenide [4,8–10]. Computational parameters are displayed in Table 2.2. The values given for these parameters have been adjusted to yield acceptable solution accuracy (less than one-percent relative error). Pseudo-transient iteration to a steady state was performed, and therefore only the smallest time step is given.

The plots of Figs. 2.2 and 2.3 depict the steady-state distribution function versus velocity in two high-symmetry directions[15]: one along v_x for $v_\rho = 0$

[15]Figure 2.3 portrays the distribution as an even function of v_ρ solely for aesthetic purposes. Actually v_ρ is defined for nonnegative values only, so that "negative v_ρ" coincides with positive v_ρ at a polar angle $\phi = \pm\pi$.

Quantity	*Value*	*Units*
Electric field strength, E_z	5.00×10^6	volts/meter
Time step (minimum), Δt^h	1.00×10^{-14}	seconds
Number of v_ρ points, L	40	—
Number of v_z points, M	80	—
Cell size, Δv_ρ	6.13×10^4	meters/second
Cell size, Δv_z	4.60×10^4	meters/second
Number of iterative scans	~ 3000	—
Average change in f_{ij}^h per iterative scan (steady state)	$\sim 10^{-7}$	—

Table 2.2: Computational parameters for the (v_ρ, v_z, t) problem.

and the other along v_ρ for $v_z = 0$. As expected, the distribution vanishes at large velocity magnitudes. More importantly, an asymmetry in the v_z dependence of the distribution is evident and arises from the influence of the z-directed electric field. In addition, optic phonon emission is seen to rapidly attenuate the distribution for velocities greater than v_ℓ. Significant heating (or broadening) of the distribution is apparent and is chiefly a consequence of randomizing collisions. Interestingly, the v_ρ dependence of the distribution shows significant heating (see Fig. 2.3), although the field points in a direction perpendicular to $\hat{\mathbf{e}}_\rho$. Again, this feature is produced by collision processes, which transfer carriers from states with large v_z and small v_ρ to those with small v_z and large v_ρ.

The true three-dimensional nature of the carrier distribution is displayed in the contour plot of Fig. 2.4. It is now apparent that the distribution closely resembles a distorted ellipsoid. The distortion can be understood as arising from two factors: the z-directed electric field and the optic-phonon collision process. Anisotropic polar-optic phonon scattering tends to accentuate elongation of this ellipsoid because low-angle collisions dominate.

2.2 The (x, v_x, t) Problem

Now that some of the issues relating to space-independent solution of the BTE have been investigated, it is fitting to consider solution of the space-dependent BTE. In fact, device simulation is intrinsically space dependent;

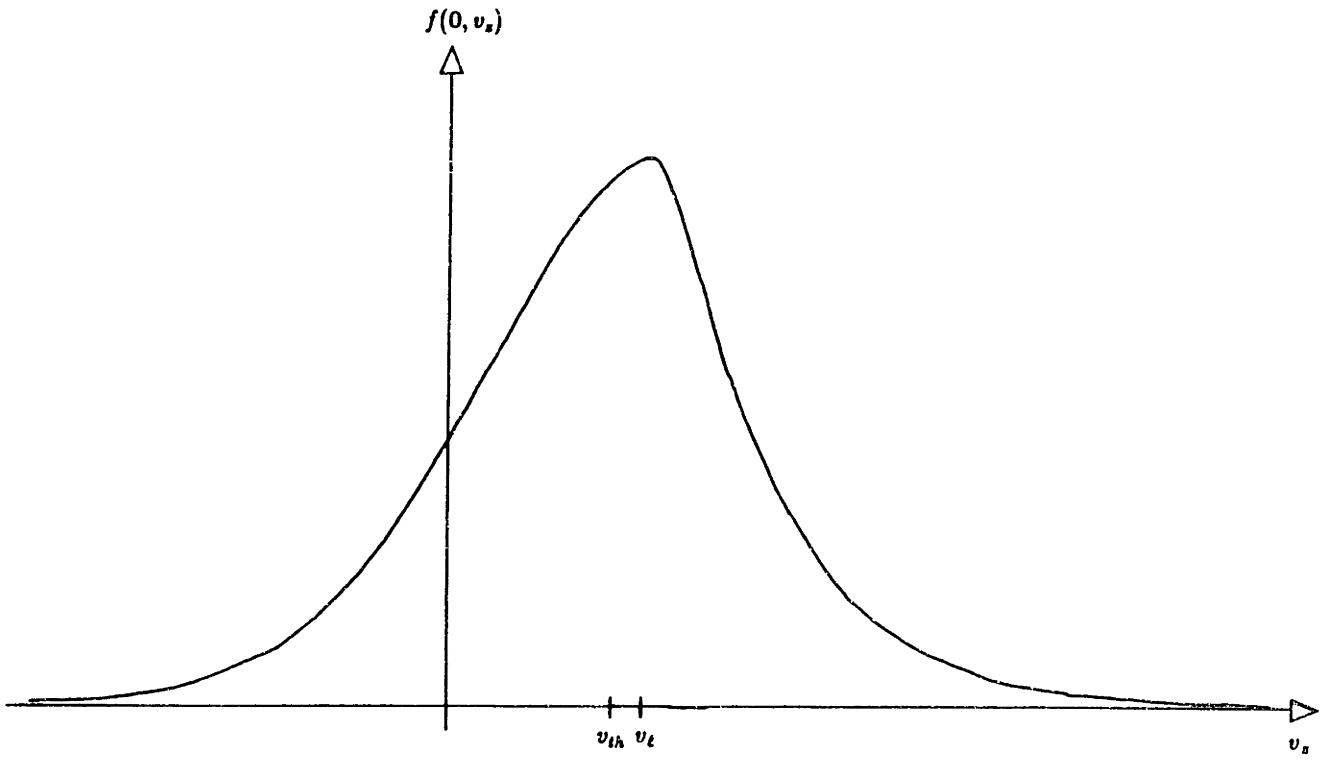

Figure 2.2. Steady-state carrier distribution versus v_z for $v_\rho = 0$.

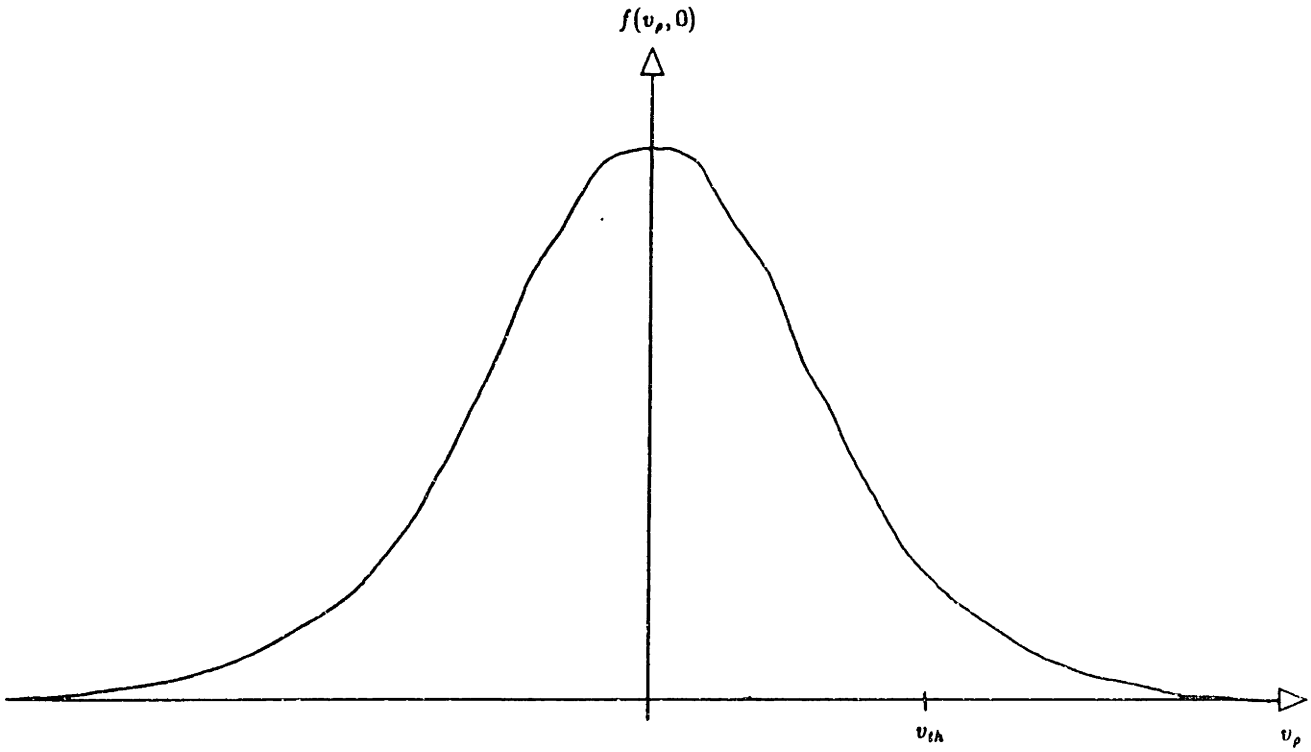

Figure 2.3. Steady-state carrier distribution versus v_ρ for $v_z = 0$.

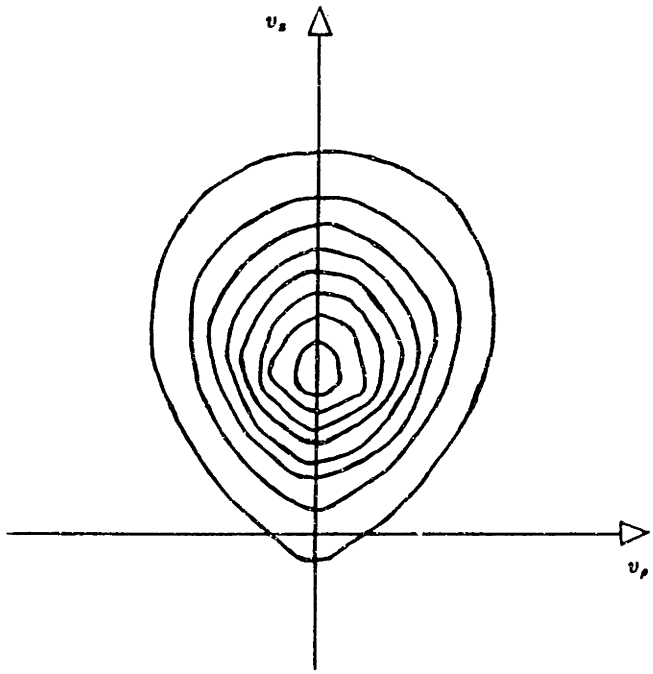

Figure 2.4. Contour plot of steady-state carrier distribution versus (v_ρ, v_z).

hence solution of the space- as well as the velocity- and time-dependent BTE is of great importance. The simplest case of a space-, velocity-, and time-dependent distribution function is $f = f(x, v_x, t)$; variation is allowed along only a single space and velocity dimension.[16] Physically, this case corresponds to a situation in which carriers are constrained to move along a single, fixed line where collisions can alter only the magnitude and sign of velocity. Although physically unrealistic in the context of device simulation, this simple problem possesses many essential attributes that directly generalize to systems of higher dimensionality.

Consistent with the distribution function's dependence, only the x component of electric field is nonvanishing. It varies in space and time: $\boldsymbol{E} = E_x(x,t)\hat{\boldsymbol{e}}_x$. In continuous variables, the BTE takes the form

$$\frac{\partial f}{\partial t} = -v_x \frac{\partial f}{\partial x} - \frac{qE_x}{m^*}\frac{\partial f}{\partial v_x} + Cf. \tag{2.16}$$

One of the more frequently employed techniques for numerical solution of differential equations is the finite-difference method. Over the years, much has been written about this method [15,20,21]. In the following sections the finite-difference method will be applied to Eq. (2.16). Implementation of the finite-difference method is straightforward and requires moderate levels of computation when three independent variables are involved. Moreover, a detailed understanding of this method is critical for the development of the hybrid FD-spectral method which will be taken up in the next two chapters.

2.2.1 The Finite-Difference Method

2.2.1.1 Space and Velocity Discretization

Finite-difference discretization of independent and dependent variables is analogous to that of Rees's integral method. A discrete space-velocity domain is defined, indexed with (ij):

$$f(x, v_x, t) \longrightarrow f_{ij}(t), \tag{2.17}$$

$$x_i = x_o + i\Delta x,$$

[16] In physically realistic systems, as will be seen in later chapters, other components of space and velocity must be included.

$$v_{xj} = v_{xo} + j\Delta v_x,$$
$$i = 1, \cdots, L,$$
$$j = 1, \cdots, M.$$

The above equation is completely analogous to (2.2) and should be self-explanatory.

Various differencing schemes exist for approximating the derivatives in (2.16). There is the forward-difference scheme:

$$\frac{\partial f}{\partial x} \longrightarrow \frac{f_{i+1j} - f_{ij}}{\Delta x} \doteq \Delta_x^+ f_{ij}, \tag{2.18}$$

$$\frac{\partial f}{\partial v_x} \longrightarrow \frac{f_{ij+1} - f_{ij}}{\Delta v_x} \doteq \Delta_{v_x}^+ f_{ij}. \tag{2.19}$$

For convenience, the difference operators Δ_x^+ and $\Delta_{v_x}^+$ have been defined. On the other hand, a reverse-difference scheme also exists:

$$\frac{\partial f}{\partial x} \longrightarrow \frac{f_{ij} - f_{i-1j}}{\Delta x} \doteq \Delta_x^- f_{ij}, \tag{2.20}$$

$$\frac{\partial f}{\partial v_x} \longrightarrow \frac{f_{ij} - f_{ij-1}}{\Delta v_x} \doteq \Delta_{v_x}^- f_{ij}. \tag{2.21}$$

Both difference schemes are of equal accuracy, having a truncation error that is first order in increment variable.[17] Unfortunately, formulas (2.18) and (2.19) or (2.20) and (2.21) will result in a numerical instability when applied to (2.16), or to any other hyperbolic system for that matter (see Appendix B) [20,21]. To resolve this difficulty, the physical origin of each derivative term must be examined. Each term corresponds to convection of carriers either in space or in velocity. Flow by convection is always directional, its direction determined by the sign of the prefactor which multiplies each derivative term in (2.16). Negative prefactors imply flow in the direction of increasing mesh point index and thus reverse differencing should be used. Contrarily, positive prefactors imply flow in the direction of decreasing mesh point index and thus forward differencing should be used. Consistent with these remarks

[17]This is evident after expanding the distribution function in a Taylor series. For the forward-difference representation of $\partial f/\partial x$, $f(x + \Delta x, v_x, t) = f(x, v_x, t) + [\partial f(x, v_x, t)/\partial x]\Delta x +$ (terms of order $\leq \Delta x^2$). Therefore, $\partial f/\partial x = (f_{i+1j} - f_{ij})/\Delta x +$ (terms of order $\leq \Delta x$); other derivative approximations can be handled similarly.

a "mixed" difference operator can be defined:

$$\frac{\partial f}{\partial x} \longrightarrow \begin{cases} \Delta_x^- f_{ij} & \text{if } v_{xj} > 0 \\ \Delta_x^+ f_{ij} & \text{if } v_{xj} < 0 \end{cases} \doteq \Delta_x^{\pm} f_{ij}, \tag{2.22}$$

$$\frac{\partial f}{\partial v_x} \longrightarrow \begin{cases} \Delta_{v_x}^- f_{ij} & \text{if } qE_x > 0 \\ \Delta_{v_x}^+ f_{ij} & \text{if } qE_x < 0 \end{cases} \doteq \Delta_{v_x}^{\pm} f_{ij}. \tag{2.23}$$

Difference formulas (2.22) and (2.23) will result in a numerically stable finite-difference algorithm.[18]

The electric field is defined at each mesh point and discretizes as

$$E_x(x,t) \longrightarrow E_{xi}(t). \tag{2.24}$$

And, in the spirit of the Rees integral method, the continuous collision term transforms into a sum over velocity mesh points $v_{xj'}$, symbolized below:

$$Cf \longrightarrow \sum_{j'} C_{jj'} f_{ij'}(t). \tag{2.25}$$

2.2.1.2 Time Discretization

The time dependence of the distribution function discretizes in a straightforward manner, with variable time samples, according to [compare with (2.4)]

$$f_{ij}(t) \longrightarrow f_{ij}^h, \tag{2.26}$$

$$t_h = t_o + \sum_{u=1}^{h} \Delta t^u,$$
$$h = 0, 1, 2, \cdots.$$

Conversion of the time derivative in (2.16) to a discrete representation parallels the forward-difference scheme of the previous section, except in this case instabilities are not expected to arise. Therefore,

$$\frac{\partial f_{ij}(t)}{\partial t} \longrightarrow \frac{f_{ij}^{h+1} - f_{ij}^h}{\Delta t^h}. \tag{2.27}$$

[18]Numerical analysts commonly call this differencing scheme "upwinding", as the differencing is in the direction from which the "convective wind" is "blowing" (the "wind" components being given by the pertinent prefactor).

Discretization (2.27) is simply the conventional forward-Euler formula, modified for a variable time step [22]. The truncation error per time step is of order Δt^h. Lastly, the electric field transforms as follows:

$$E_{xi}(t) \longrightarrow E_{xi}^h. \tag{2.28}$$

2.2.1.3 Finite-Difference Equations

At each time sample t_h a set of coupled difference equations for f_{ij}^{h+1} in terms of f_{ij}^h can be written. The equations are defined on a uniform rectangular space-velocity mesh that extends over a finite line segment in space and over an infinite segment in velocity. However, as depicted in Fig. 2.5, this velocity mesh has been truncated for convenience. Computational cells with centers (x_i, v_{xj}) are of two types, internal and boundary.

Based on the transformation equation of the previous sections, the finite-difference equation holding at each internal mesh point is[19]

$$f_{ij}^{h+1} = f_{ij}^h + \Delta t^h(-v_{xj}\Delta_x^{\pm} f_{ij}^h - \frac{qE_{xi}^h}{m^*}\Delta_{v_x}^{\pm} f_{ij}^h + \sum_{j'} C_{jj'} f_{ij'}^h), \tag{2.29}$$

$$i = 2, \cdots, L-1, \quad j = 2, \cdots, M-1.$$

Thus, the difference Eq. (2.29) establishes a procedure for numerical solution of the BTE (2.16), and, unlike Rees's integral method, incorporates the effects of drift, diffusion, and collisions in a single iterative step.

At boundary mesh points, alternate equations apply. With reference to Fig. 2.5 and the discussion of Section 1.1.2, for mesh points along the top and bottom boundaries

$$f_{ij}^h = 0, \tag{2.30}$$

$$h = 0, 1, 2, \cdots,$$
$$i = 1, \cdots, L, \quad j = 1, M.$$

The mathematically correct condition is $f_{ij}^h = 0$ for $i = 1, \cdots, L$ when $qE_{xi} > 0$ and $j = 1$ or when $qE_{xi} < 0$ and $j = M$; otherwise (2.29) is to be invoked. This condition is equivalent to (2.30) when the boundary velocities v_{x1} and

[19] Without loss of generality M is assumed even and the discretization mesh is assumed symmetric about $v_x = 0$ (see Fig. 2.5).

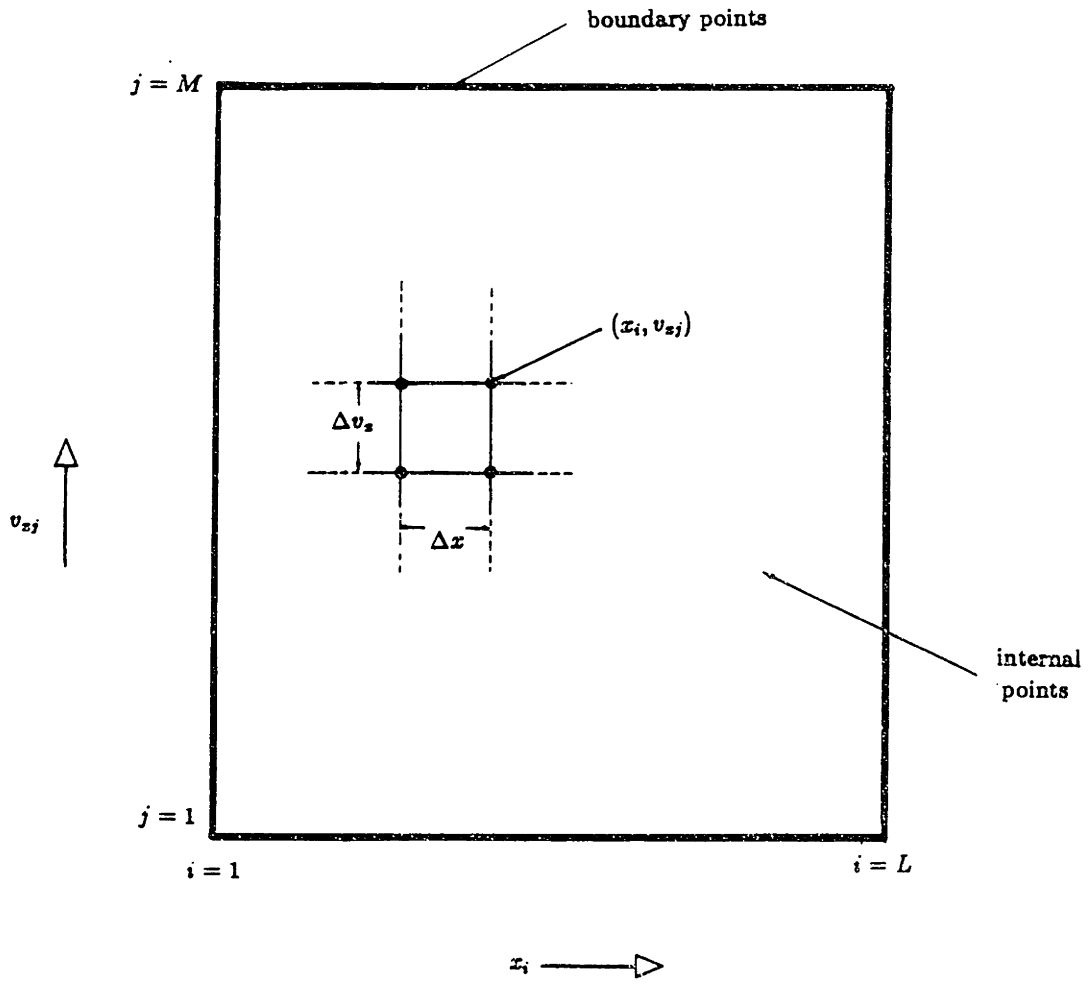

Figure 2.5. Space-velocity discretization mesh for the (x, v_x, t) problem.

v_{xM} are sufficiently large. For the sake of computational efficiency, boundary condition (2.30) should be used. Meanwhile, for left and right boundary mesh points,

$$f_{ij}^h = \begin{cases} f_o(v_{xj}) = \mathcal{N} \exp\left(-\frac{m^*}{2k_BT} v_{xj}^2\right) & i = 1,\ j = (M/2)+1, \cdots, M, \\ 0 & i = L,\ j = 1, \cdots, M/2, \end{cases} \tag{2.31}$$

$$h = 0, 1, 2, \cdots,$$

where f_o is the equilibrium Maxwellian with normalization constant $\mathcal{N}$. Otherwise (2.29) is to be invoked. Other, more complicated left- and right-injected carrier distributions are possible; those of (2.31) have proved adequate for these numerical studies.

The final matter of initial conditions must now be resolved. Along the same lines as the latter part of Section 2.1.1.3, a frequent choice for initial distribution function is the equilibrium Maxwellian:

$$f_{ij}^0 = f_o(v_{xj}), \tag{2.32}$$

$$\begin{aligned} &i = 1,\ j = 1, \cdots, M/2, \\ &i = 2, \cdots, L-1,\ j = 2, \cdots, M-1, \\ &i = L,\ j = (M/2)+1, \cdots, M. \end{aligned}$$

Occasionally, it may be desirable to use previously calculated results rather than the above equation.

2.2.2 The Collision Term

2.2.2.1 Fictitious One-Dimensional Scattering Rates

Equation (2.16) governs transport in a physically unrealistic one-dimensional system, as mentioned before. Consequently, scattering rates that are analogous to those of realistic higher-dimensionality systems must be postulated. A fictitious scattering probability rate can be deduced by arbitrarily asserting criteria: (1) the scattering probability rate should depend on only initial and final velocity states, v_x and v_x', (2) only velocity states with equal magnitude

should couple (scattering is therefore quasi elastic), (3) scattering should be isotropic, that is, there should be no directional preference for the final scattered velocity vector $v_x'\hat{e}_x$, and last of all, (4) the scattering probability rate should have a simple mathematical form. Equation (2.33) meets all these criteria:

$$S_{qe}(v_x, v_x') = S_{qe}\delta(v_x + v_x'). \tag{2.33}$$

The subscripts refer to quasi-elastic scattering and the fixed constant S_{qe} is an adjustable "scattering strength". On account of the quasi-elastic nature of scattering both absorption and emission rates combine into the single rate given above.

After integration over all possible final velocities (2.33) gives forth a constant total scattering probability rate,

$$\lambda_{qe} = S_{qe}. \tag{2.34}$$

2.2.2.2 Collision Operator

The action of the collision operator on the continuous distribution function can now be determined. Subtracting the in-scattering from the out-scattering contribution yields

$$Cf = S_{qe}[f(x, -v_x, t) - f(x, v_x, t)]. \tag{2.35}$$

When discretized, (2.35) turns into

$$\sum_{j'} C_{jj'} f_{ij'}^h = S_{qe}(f_{iM+1-j}^h - f_{ij}^h) \tag{2.36}$$

for a symmetric velocity mesh (see footnote 19).

2.2.3 Numerical Implementation

2.2.3.1 Discretization Mesh

As previously discussed in connection with Fig. 2.5, a uniform rectangular discretization mesh has been set up that spans the space-velocity domain (x_i, v_{xj}). Equation (2.29) is iterated via systematic scanning of the discretization mesh. In this study, the maximum mesh size was $L = M = 80$.

In order to enhance convergence rates, a mapping algorithm was devised so that the number of cells (and therefore the cell size) could be altered during iteration. Mapping simply entailed two-dimensional interpolation between different-sized meshes (see Section C.1). Convergence rates were enhanced by starting with a coarse mesh and progressively refining the mesh during ensuing time steps. In practice, the procedure was found to speed up convergence by factors as large as ten.

2.2.3.2 Collection Points

An interesting peculiarity of first-order, quasi-hyperbolic systems is the existence of so-called collection points.[20] When one or more coefficients of gradient terms in the governing equation vanish, sudden, unexpected behavior may occur. In the BTE (2.16) collection points are $v_{xj} = 0$ and $E^h_{xi} = 0$. Anomalies, including step discontinuities and numerical instabilities, have been observed whenever mesh and collection points coincide. The situation is easily remedied if the discretization mesh is shifted or, alternatively, if a small amount is added to the coefficients at each collection point.

2.2.3.3 Solution of the Finite-Difference Equations

The change in the distribution function after each time step is determined by iterating (2.29) at each internal mesh point. An initial condition begins the iteration; note, however, that boundary points for which f^h_{ij} is specified in (2.30) and (2.31) do not require iteration. According to Section 2.2.1.2, Eq. (2.29) defines a forward-Euler time-stepping scheme. The dual advantage of reduced memory requirement and improved numerical stability is obtained through a modification of the time-stepping scheme. Updated values for the distribution function replace old values as soon as available in a Gauss-Siedel fashion. A separate mesh array need not be stored for each time step, contrary to the standard forward-Euler scheme; at the same time, numerical stability is improved because the iteration is semi-implicit (see footnote 12). The numerical errors associated with conversion from the forward-Euler to modified forward-Euler schemes are insignificant.

[20]The term "collection" arises from the field of fluid dynamics where it signifies an accumulation of fluid matter.

Accuracy in time-dependent calculations necessitates small time steps, thus demanding a relatively large amount of computation. The use of variable time steps can somewhat reduce the computational effort.[21] In the case of steady-state calculation, computational effort can be dramatically reduced if a pseudo-transient is evolved. Convergence is accelerated by starting with large time increments (but not too large as to violate any CFL criteria; refer to the next section) and gradually decreasing their size as the iteration proceeds. A reduction of time-step size will improve accuracy in steady-state solutions.

With reference to Fig. 2.5, an antisymmetric scanning pattern has been used to iterate (2.29). First, the top half of the space-velocity mesh is scanned left-to-right, top-to-bottom, and then, the bottom half is scanned right-to-left, bottom-to-top. This scanning pattern is designed to eliminate nonuniformities due to the scanning process itself. Successful results have been attained using this scanning procedure.

2.2.3.4 Numerical Stability

The CFL stability criterion (see Section 2.1.3.3 and Appendix C) sets limits for the relative sizes of time steps and space increments. Any quasi-hyperbolic system that violates the CFL criterion will inevitably develop a numerical instability. For the case at hand, two CFL stability criteria exist:

$$|v_{xj}|_{max} \leq \frac{\Delta x}{\Delta t^h} \tag{2.37}$$

and

$$\frac{1}{m^*}|qE^h_{xi}|_{max} \leq \frac{\Delta v_x}{\Delta t^h}. \tag{2.38}$$

In other words, maximum physical velocities and accelerations need be less than corresponding mesh velocities and accelerations.

2.2.3.5 Numerical Errors

The finite-difference method, like the Rees integral method, is subject to round-off and discretization errors. Accumulation of round-off error is

[21] Even though the time steps are variable, they are always assumed small compared with the time to converge to steady state.

ignorable since there are relatively few mathematical operations per iteration. This is not the case with discretization error. These errors—originating from discretization in space, velocity, and time—can lead to false solutions, or perhaps, a numerical instability.

It is possible to monitor discretization error by checking the relative change in the distribution function for successively smaller space-velocity increments and time step ($\Delta x, \Delta v_x, \Delta t^h$). Except for the difference in the independent variables, this self-consistent procedure is identical to to that of Section 2.1.3.4, and is therefore limited by the computer system specifications—memory size and execution rate.

2.2.4 Results and Discussion

2.2.4.1 Execution Rate

All calculations were performed on an HP-1000F minicomputer (see also Section 2.1.4.1). Execution rates were enhanced using variable time-stepping, space-velocity mesh mapping, and whenever appropriate, iterating a pseudo-transient. An execution rate of twenty-five time-steps per second was achieved for a mesh size of $L = M = 80$.

2.2.4.2 Solution Verification

A three-level solution verification procedure has been carried through. This procedure has been established in treating the previous (z, v_ρ, v_z) problem (see Section 2.1.4.2). Verification consists of tests without collisions (ballistic), tests with collisions, and tests based on qualitative physical reasoning.

Steady-state[22] ballistic calculations, in which the collision term of (2.29) is dropped, were compared with available analytical solutions in Appendix F. Calculated solutions agreed with Eqs. (F.13) and (F.14) to within one percent for constant positive electric fields and to within ten percent for constant negative fields ($q > 0$). The larger error in negative field solutions is attributable to difficulties in resolving shock discontinuities associated with the ballistic version of the BTE.[23]

[22]In accordance with thesis objectives, issues relating to time-dependent calculations are left to future works and will not be addressed here.

[23]These discontinuities disappear upon inclusion of the collision term.

Quantity	*Value*	*Units*
Carrier effective mass, m^*	2.99×10^{-31}	kilograms
Quasi-elastic scattering constant, S_{qe}	2.00×10^{6}	seconds^{-1}

Table 2.3: Physical parameters for equivalent spherical, parabolic X valley of silicon, with fictitious quasi-elastic scattering.

After verification of ballistic solutions, the collision term was included. Despite its simple form, the collision-term computer routine was checked numerical evaluation of the identity $\sum_{j'} C_{jj'} f_{ij'} = 0$ for $f_{ij'} = f_o(v_{zj'})$.

Qualitative physical reasoning was then used for additional verification. Solutions were checked to obey boundary conditions. Also, the x component of current density, J_x, was checked for spatial invariance.[24] Finally, observation of a bimodal velocity distribution in high-field spatial regions confirmed the physical fact that the fictitious scattering mechanism has a symmetrizing influence.

2.2.4.3 Numerical Solutions

This section is devoted to results for a representative finite-difference solution of the BTE (2.16). Physical parameters for the calculations are listed in Table 2.3.[25] Though the scattering mechanism is artificial, most physical parameters were chosen to closely agree with those for silicon.[26] Computational parameters are listed in Table 2.4. Only the final minimum values of space increment, velocity increment, and time step are given for this steady-state calculation.

A cusped-barrier potential distribution was selected, as drawn in Fig. 2.6. On either side of the cusp the potential varies quadratically; hence the electric field is piecewise linear. This potential is similar to that found during the operation of many semiconductor devices. In fact, the cusp represents an extreme test of the solution method because real device potentials will tend to vary more smoothly.

[24] In general $\partial J_x/\partial x = -q\partial n/\partial t$, where $J_x = q \int dv_x \; v_x f(x, v_x, t)$. Under steady-state conditions, $\partial n/\partial t = 0$, $f = f(x, v_x)$; thus $J_x =$ constant.

[25] Here, and in all future calculations, refer to Table 2.1 for the values of $q, \hbar, k_B$, and T.

[26] For simplicity, an equivalent X-point minimum (spherical, parabolic) is assumed.

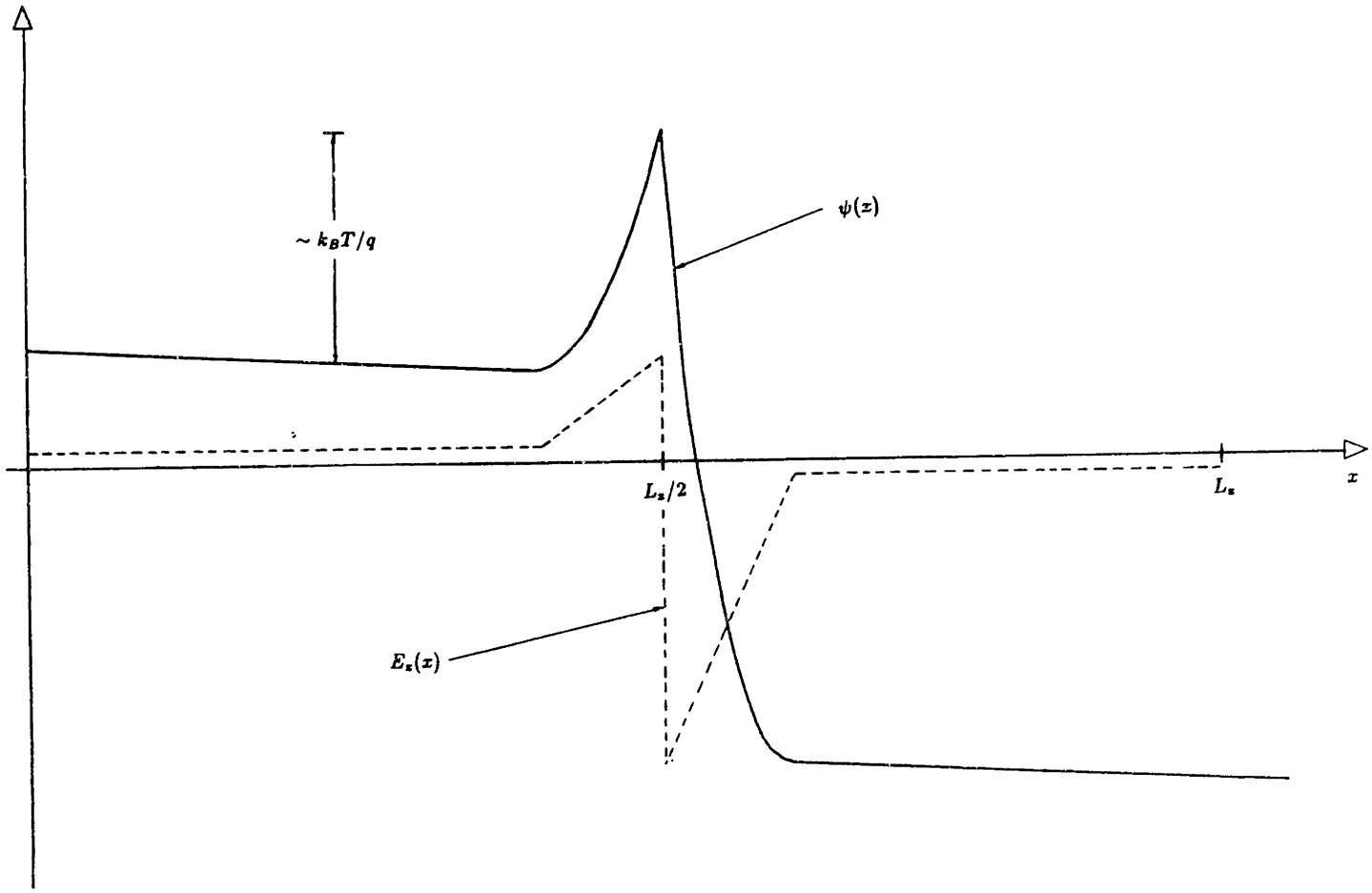

Figure 2.6. Potential and electric field versus x.

Quantity	*Value*	*Units*
Time step (minimum), Δt^h	1.00×10^{-9}	seconds
Number of x points, L	80	—
Number of v_x points, M	80	—
Cell size, Δx	1.25×10^{-8}	meters
Cell size, Δv_x	2.75×10^{4}	meters/second
Number of iterative scans	~ 2500	—
Average change in f_{ij}^h per iterative scan (steady state)	$\sim 10^{-7}$	—

Table 2.4: Computational parameters for the (x, v_x, t) problem.

The steady-state distribution functions are displayed in Figs. 2.7 and 2.8. Figure 2.7 shows how the distribution function changes with v_x, with x as a parameter. Figure 2.8 is a three-dimensional representation of the same distribution function over the entire space-velocity domain. It is apparent that boundary conditions are obeyed. The distribution function vanishes for large positive and negative v_x and at $x = L_x$, $v_x < 0$; while it becomes the equilibrium Maxwellian at $x = 0, v_x > 0$. Near the entrance region $x \approx 0$ the distribution function is symmetric and nearly Maxwellian. Carriers with insufficient energy to cross the potential cusp simply "roll back" to the entrance region; the symmetrizing effect of scattering is a weak perturbation. In the region near the potential cusp, the transition region $x \approx L_x/2$, the distribution changes rapidly versus x and v_x. This behavior is primarily attributable to the sudden reversal of electric field. Beyond the transition region and toward the exit region $x \approx L_x$ the distribution function is highly asymmetric and in no way resembles an equilibrium Maxwellian. Its bimodal structure stems from the simultaneous influence of accelerating fields and symmetrizing scattering. The secondary peak in the distribution ($v_x < 0$) is always smaller than the primary one ($v_x > 0$). This is in large part due to the boundary condition at $x = L_x, v_x < 0$.

Carrier transport can be better understood if typical trajectories are considered. Two types of trajectories are possible. Carriers with insufficient energy to surmount the potential barrier merely roll up against it and then back down with the random chance of being scattered to a velocity state of opposite sign along the way. Some carriers have sufficient energy to surmount the potential barrier, beyond which they quickly roll down toward the exit

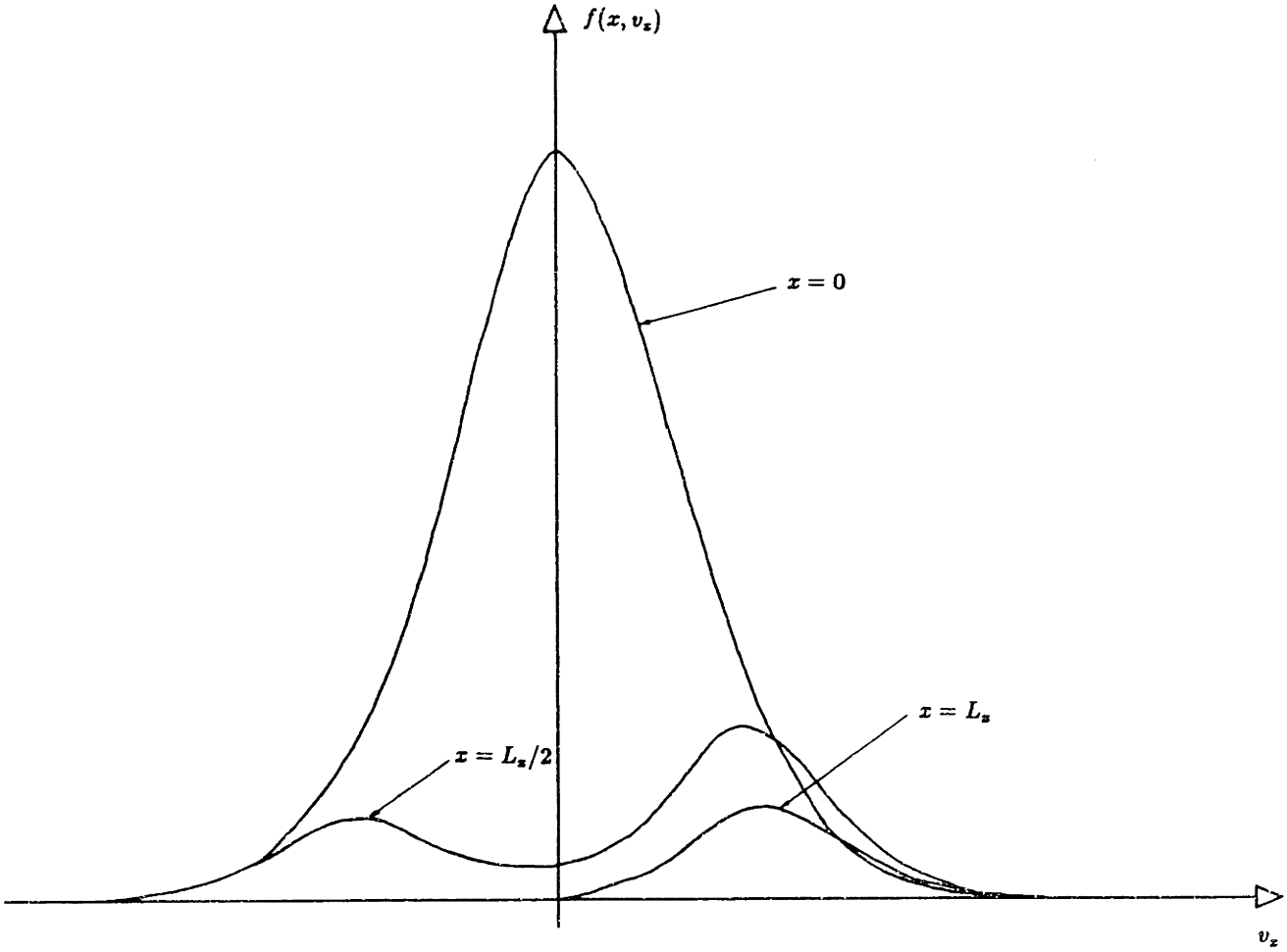

Figure 2.7. Steady-state carrier distribution versus v_x, parameterized from $x = 0$ to $x = L_x$.

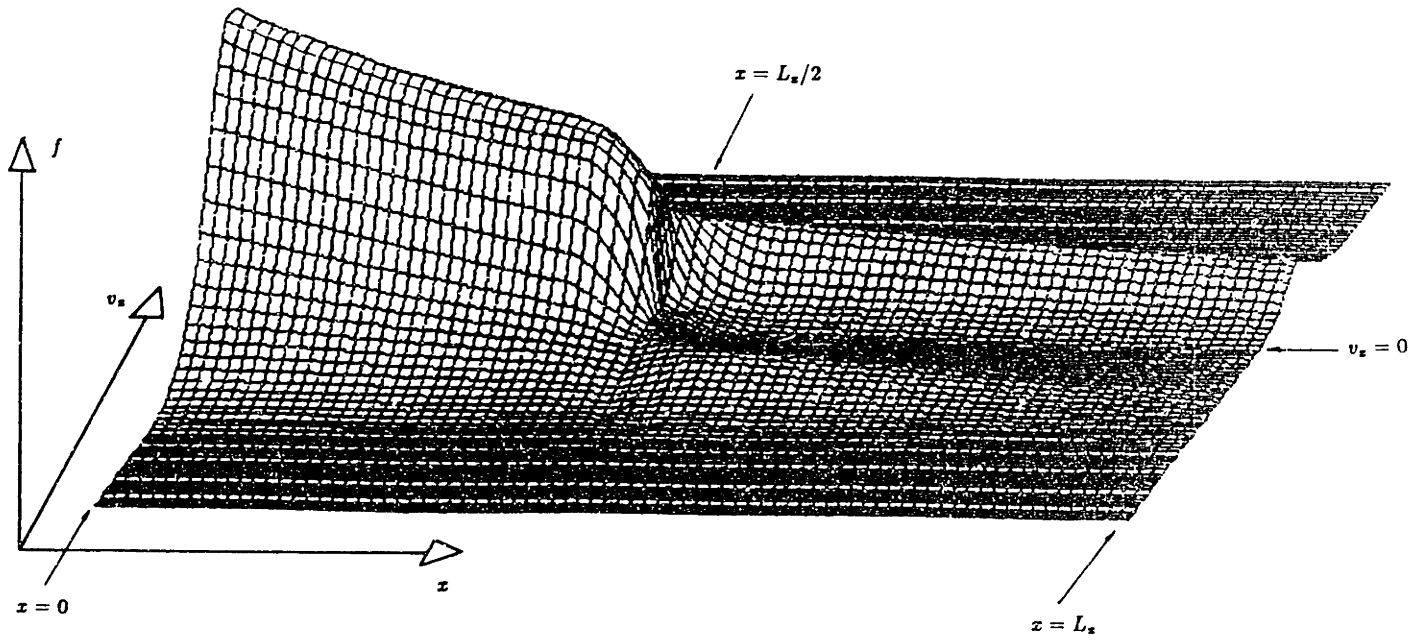

Figure 2.8. Three-dimensional plot of the carrier distribution versus (x, v_x).

region. Random scattering can reverse the direction of some carriers (the first time after which they are greatly slowed by the large opposing field); yet, from time to time carriers will eventually reach the exit region.

It is fitting to close this section with a brief digression from which one can draw direct parallels to the FD-spectral method that composes the core of this thesis and which is covered in the next two chapters. As stated earlier, the x component of current density should be constant with x. Numerical integration for J_x shows that it indeed is not constant but varies as much as seven percent from average, with largest deviations in close proximity to the potential cusp. The finite-difference method, as presented here, is not conservative, yet it attempts to minimize the spatial variation of current density. If desired, current density variation can be reduced by decreasing space and velocity increments.[27] Conservative numerical formulations are possible but are significantly more complicated [23]. Moreover, it is precisely this variation in current density which permits an accessment of absolute numerical error. Consequently, so long as the discretization procedure is of sufficient resolution (in other words, consists of sufficiently many mesh points), easily implemented nonconservative methods are well-suited for solution of the BTE.

[27] In the limit $\Delta x, \Delta v_x \rightarrow 0$, variation in current density becomes vanishingly small. Here, issues concerning round-off error and execution time are assumed ignorable.

Chapter 3

Spectral Solution of the Low-Dimensionality BTE

The methods of Chapter 2 are practical when the BTE takes on a simple form, that is, no more than two independent variables in space and velocity. Consider, for example, the finite-difference method of Section 2.2.1. If an additional space variable were included, iterative scanning would proceed over a three-dimensional domain (two space and one velocity variables), a difficult computational task.[1] Consider now, the Rees integral method of Section 2.1.1. If an additional velocity variable were included, not only would iterative scanning proceed over a three-dimensional domain, but evaluation of the physically realistic collision term would involve a time-consuming double integration (see Appendix E).

Chapter 2 has, however, laid the groundwork from which highly efficient methods for solving the BTE can be developed. The present chapter is devoted to one such method, the FD-spectral method, first mentioned in Section 1.2.3. The FD-spectral method, as developed here, applies to systems of low dimensionality that have a total of one to three space and velocity variables. In line with the thesis objectives, only solution of the time-independent BTE will be attempted. To advantage, time-independent FD-spectral equations will be solved directly in a single one-step procedure,

[1] Three-dimensional finite-difference calculations are barely feasible on today's large computer mainframes and array processors; in fact, most medium-sized computers and minicomputers (the HP-1000F included) are overburdened by these calculations.

Gaussian elimination.[2]

This chapter breaks down into two major parts. In the first part, the FD-spectral method is applied to a two-dimensional (x, v_x) problem. In the second part, it is applied to a three-dimensional (z, v_ρ, v_z) problem. Although somewhat artificial from the device simulation standpoint, the (x, v_x) problem offers relative simplicity and, using collision term (2.35), should agree with steady-state finite-difference solutions of Section 2.2.4.3. Once the FD-spectral method has been established, the more realistic (z, v_ρ, v_z) problem, which incorporates phonon scattering, will be solved. It is this latter problem that will indicate the overall feasibility of simulating real devices by FD-spectral solution of the BTE.

3.1 The (x, v_x) Problem

Based on the introductory remarks of Section 2.2, the simplest case of a time-independent, space- and velocity-dependent distribution function is $f = f(x, v_x)$. Hence, variation is permitted only along a single space and velocity dimension. Consistent with this picture, the electric field can only have an x component, with possibly an x dependence: $\boldsymbol{E} = E_x(x)\hat{\boldsymbol{e}}_x$. The BTE for this problem is identical to Eq. (2.16), except for exclusion of the time variable:

$$-v_x\frac{\partial f}{\partial x} - \frac{qE_x}{m^*}\frac{\partial f}{\partial v_x} + Cf = 0. \tag{3.1}$$

3.1.1 The FD-Spectral Method

3.1.1.1 Velocity Discretization

When the FD-spectral method is applied to (3.1) velocity is discretized in spectral fashion (refer to Section 1.2.3). The distribution function is approximated with a series expansion in N velocity-dependent basis functions ϕ_n with space-dependent expansion coefficients:

$$f(x, v_x) \approx \sum_{n=1}^{N} \alpha_n(x)\phi_n(v_x). \tag{3.2}$$

[2]In low-dimensionality systems, direct solution of time-independent equations is numerically efficient compared with iterative solution. The next chapter concerns iterative solution of high-dimensionality systems.

From the above equation, it is apparent that knowledge of the N expansion coefficients is all that is necessary to evaluate the carrier distribution (given a specific basis set $\phi_1, \cdots, \phi_N$). Symbolically, this spectral discretization can be represented as[3]

$$f(x, v_x) \longrightarrow \alpha(x), \tag{3.3}$$

$$\{\alpha(x)\}_n = \alpha_n(x),$$
$$n = 1, \cdots, N.$$

Relation (3.3) merely states that the distribution function, under a spectral velocity discretization, transforms into a spatially dependent vector field $\alpha(x)$.

Implicit in this treatment is an *a priori* selection of the basis set. For the time being, the basis set is assumed to comprise N successive functions of a mathematically complete set. Additional details concerning specific basis sets will be given in a later section. These basis functions, in general, possess zeros and extrema that will be taken to increase in number with order n. Furthermore, it will be assumed that the functions alternate in parity with increasing order.[4]

3.1.1.2 Space Discretization

Discretization of the space variable x proceeds according to the finite-difference method, in a manner analogous to that of Section 2.2.1.1. Space is divided into L cells of width Δx with center points x_i; the coefficient vector $\alpha(x)$ is now defined over a discrete domain:

$$\alpha(x) \longrightarrow \alpha_i, \tag{3.4}$$

$$x_i = x_o + i\Delta x,$$
$$i = 1, \cdots, L.$$

[3]Here, and throughout this work, subscripted curly brackets denote elements of a vector quantity in the single-subscript case, or elements of a matrix quantity in the double-subscript case.

[4]These last two properties are true for all basis sets used in this thesis and most of the standard mathematical sets found in the literature [24]. In general, for an arbitrary basis set, these properties need not be strictly true.

In similar fashion, the electric field becomes a function of discrete space, so that

$$E_x(x) \longrightarrow E_{xi}. \tag{3.5}$$

Observe that the discrete version of the distribution function can now be written

$$f_i(v_x) = \sum_{n=1}^{N} \{\alpha_i\}_n \phi_n(v_x). \tag{3.6}$$

3.1.1.3 FD-Spectral Equations

FD-spectral equations are formulated following the method outlined in Section 1.2.3. The series approximation (3.2) is substituted into the governing equation, (3.1). Spatial variables and derivatives are handled through the standard finite-difference method. Velocity derivatives and collision term integrals are evaluated explicitly for each basis function. FD-spectral equations are developed by forcing the velocity residual to zero at N collocation points v_{xk}, $k = 1, \cdots, N$. Collocation points can be chosen to coincide with either extrema of ϕ_N or zeros of ϕ_{N+1}.[5] Collocation at either extrema or zeros results in a highly accurate spectral approximation (see Appendix C.4). Extrema and zero collocation are of comparable accuracy, so for reasons of standardization, extrema collocation will be adopted here and for the rest of this work. Collocation should avoid the collection point $v_x = 0$, based on the observations of Section 2.2.3.2. Conveniently, collection points are avoided by simply choosing N even.[6]

The illustration of Fig. 3.1 depicts the hybrid FD-spectral mesh for this problem. It consists of finite-difference points x_i, internal and boundary, as well as collocation points v_{xk}. At each internal finite-difference point the procedure described in the preceding paragraph produces the vector difference equations:

$$-\boldsymbol{V}\boldsymbol{\Delta}_x^{\pm}\boldsymbol{\alpha}_i - \frac{qE_{xi}}{m^*}\boldsymbol{A}\boldsymbol{\alpha}_i + \boldsymbol{C}\boldsymbol{\alpha}_i = \mathbf{0}, \tag{3.7}$$

$$i = 2, \cdots, L-1,$$

[5]It is assumed that ϕ_{N+1} is available and that each basis function ϕ_n has n extrema and $n-1$ zeros.

[6]Since the basis functions used here have either odd or even parity, their extrema are symmetrically located with respect to $v_x = 0$.

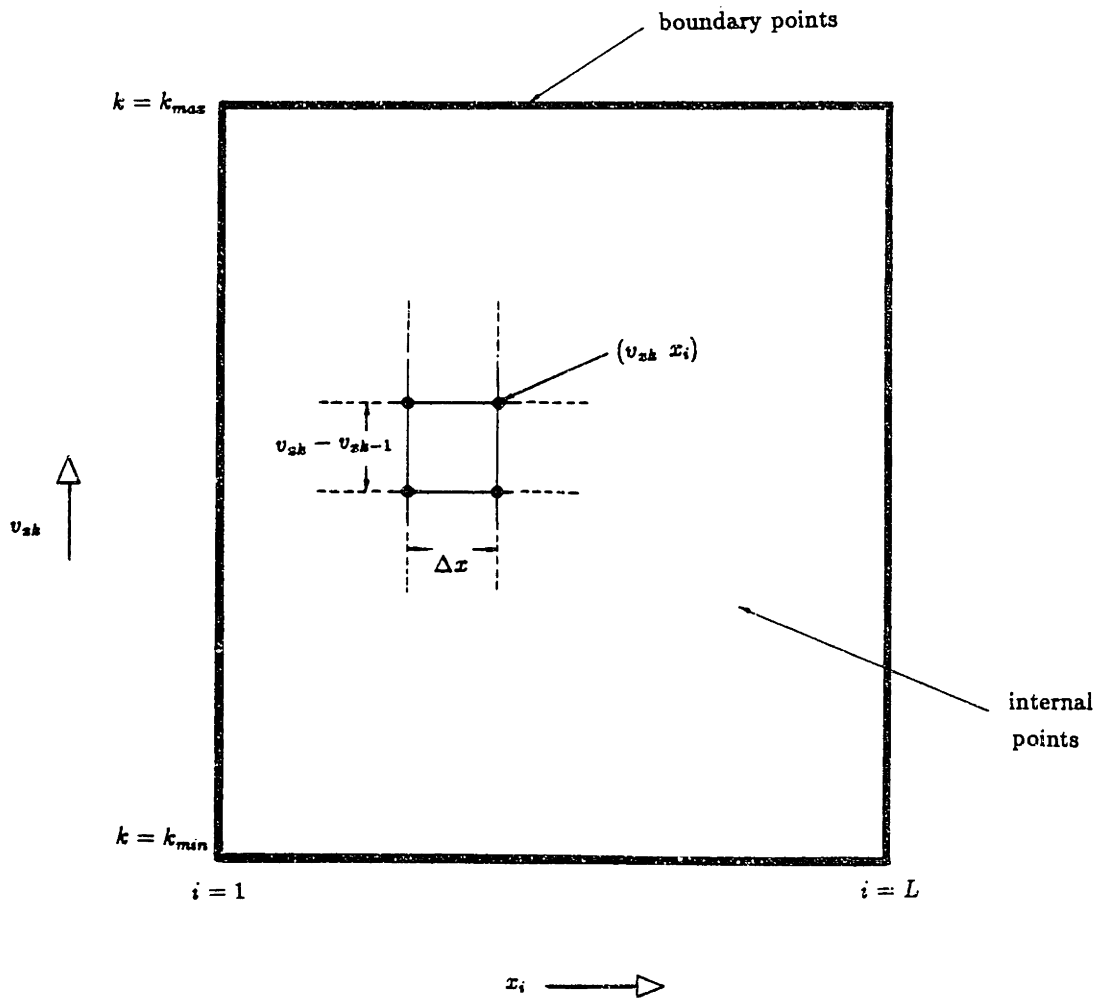

Figure 3.1. FD-spectral discretization mesh for the (x, v_z) problem.

in which α_i is an N vector, $\mathbf{o}$ is the null vector; and V, A, and C are $N \times N$ matrices with elements

$$\begin{aligned} \{V\}_{kn} &= v_{xk}\phi_n(v_{xk}), \\ \{A\}_{kn} &= \phi_n'(v_{xk}), \\ \{C\}_{kn} &= C[\phi_n(v_{xk})], \end{aligned} \tag{3.8}$$

$$k, n = 1, \cdots, N.$$

where the prime superscript denotes differentiation. The vector operator $\Delta_x^{\pm}$ in (3.7) is a direct generalization of the scalar mixed difference operator $\Delta_x^{\pm}$, first encountered in Section 2.2.1.1.

$$\{\Delta_x^{\pm}\alpha_i\}_k = \begin{cases} \Delta_x^{-}\{\alpha_i\}_k & \text{if } v_{xk} > 0. \\ \Delta_x^{+}\{\alpha_i\}_k & \text{if } v_{xk} < 0. \end{cases} \tag{3.9}$$

Coupling to boundary points with $i = 1$ and $i = L$ must also be treated. Assume collocation points are labeled $k = 1, \cdots, N/2$ for $v_{xk} > 0$ and $k = (N/2) + 1, \cdots, N$ for $v_{xk} < 0$. With Section 2.2.1.3 as a guide, at the left boundary (see Fig. 3.1) an equilibrium Maxwellian distribution of carriers is injected. Vector difference Eqs. (3.7) are still valid, but now, coupling to boundary points with $i = 1$ has to be taken into account, for which

$$\{V\alpha_1\}_k = v_{xk}f_o(v_{xk}), \tag{3.10}$$

$$k = 1, \cdots, N/2.$$

The equilibrium Maxwellian f_o has already been defined in (2.31). At the right boundary no carriers are injected, and the following formula allows coupling to boundary points with $i = L$:

$$\{V\alpha_L\}_k = 0, \tag{3.11}$$

$$k = (N/2) + 1, \cdots, N.$$

One last issue still needs to be addressed, the boundary condition associated with large velocity, $|v_x| \to \infty$. If each basis function vanishes as $|v_x| \to \infty$, the boundary condition is automatically satisfied and no new boundary equations are necessary. If, however, a basis set is selected with functions that do not vanish as $|v_x| \to \infty$ (for example, a Fourier set) additional boundary equations are necessary. They are derived by truncating

the velocity domain to the finite interval $[v_{xk_{min}}, v_{xk_{max}}]$, where $v_{xk_{min}}$ and $v_{xk_{max}}$ denote minimum and maximum collocation point values, and forcing the distribution function to zero at its endpoints. Mathematically, the first and last components on the left side of vector equations (3.7) have to be replaced[7]:

$$\{-V\Delta_x^{\pm}\alpha_i - \frac{qE_{xi}}{m^*}A\alpha_i + C\alpha_i\}_k \longrightarrow \sum_{n=1}^{N}\{\alpha_i\}_n\phi_n(v_{xk}), \qquad (3.12)$$

$$k = 1, N.$$

This procedure is somewhat tedious, but has been carried out with success for Fourier and Tchebycheff basis sets over a finite interval (refer to Section 3.1.4.3).

3.1.2 The Collision Matrix

Of vital importance is linking the previous chapter's (x, v_x, t) problem to the problem currently at hand. This will allow direct comparison, providing an independent means through which the FD-spectral method can be validated. Obviously, the logical choice of scattering mechanism is the fictitious, quasi-elastic process described in Section 2.2.2.

3.1.2.1 Matrix Elements

Elements of the collision matrix C are evaluated using formulas (3.8) and collision term (2.35), noting that the collision operator affects only the velocity variable.

$$\{C\}_{kn} = S_{qe}[\phi_n(-v_{xk}) - \phi_n(v_{xk})]. \qquad (3.13)$$

As a reminder, (3.13) includes the combined effects of in- and out-scattering of carriers.

[7]The injected distribution should be vanishingly small at interval endpoints: $f_o(v_{xk}) \approx 0$ for $k = 1, N$.

3.1.3 Numerical Implementation

3.1.3.1 Space Discretization Line

FD-spectral equations are defined on a discretization line. In this study, the discretization line has been divided into a maximum of eighty ($L = 80$) uniform cells with centers x_i. Unlike Chapter 2's finite-difference method, the FD-spectral equations are solved directly, without iteration; thus, once specified, the cell size Δx is fixed for the entire calculation.

3.1.3.2 Basis Sets

The FD-spectral method relies upon *a priori* selection of a basis set. Basis sets comprising standard mathematical functions have been picked. In circumstances where closed-form analytical expressions are not available, extrema collocation points are calculated numerically (see Appendix C.3). On account of computational limitations, no greater than thirty functions (N=30) were included in the basis set.

Various representative basis sets are used in this thesis—Fourier, Tchebycheff, and Hermite-Gaussian. The first seven functions of each set are plotted in Appendix G, Figs. G.1 through G.3. Fourier and Tchebycheff sets are defined over a finite interval and require additional boundary equations (3.12). The Fourier extrema are distributed to provide uniform interpolatory resolution throughout the velocity domain. The Tchebycheff set has a nonuniform distribution of extrema with greater density near the interval endpoints and therefore provides enhanced interpolatory resolution near interval endpoints at the expense of decreased mid-interval resolution. Hermite-Gaussian functions are defined over an infinite interval. Also, these functions decay to zero for infinite argument magnitude, eliminating the need for additional boundary equations. In contrast to the Tchebycheff set, the Hermite-Gaussian set provides excellent mid-interval interpolatory resolution while suffering from poor resolution near endpoints.[8] In practice the first element of the Hermite-Gaussian set, a simple Gaussian, is matched to the equilibrium Maxwellian distribution. Appendix G covers the important mathematical properties of these three sets.

[8] Although Hermite-Gaussian functions are defined on the infinite interval, only the finite interval $[v_{xk_{min}}, v_{xk_{max}}]$ is considered here.

3.1.3.3 Solution of FD-Spectral Equations

Solution of the FD-spectral Eqs.—(3.7), (3.10), and (3.11), with the possible modification of (3.12)—proceeds by Gaussian elimination [15]. But, before discussing the finer points of this numerical technique, issues pertaining to calculation of the spectral matrices—V,A, and C—require examination.

Through proper arrangement of collocation point labels, that is the row subscripts k, the spectral matrices become two-fold symmetric. This symmetry can be exploited to reduce spectral matrix calculation time. The collocation points, as remarked earlier, are symmetrically located about $v_x = 0$ (see footnote 6). If the spectral matrices are row ordered $v_{xk+(N/2)} = -v_{xk}$ for $k = 1, \cdots, N/2$, then the last $N/2$ rows of each spectral matrix can be determined from the first $N/2$ rows by transposing rows, with possible inversion of sign. The matrix V contains elements $v_{xk}\phi_n(v_{xk})$ that transpose $[k \rightarrow k + (N/2),\ k = 1, \cdots, N/2]$ with parity opposite to that of ϕ_n (with odd parity if ϕ_n is even or with even parity if ϕ_n is odd). The matrix A contains elements $\phi'(v_{xk})$ that transpose the same way as V.[9] Next, the matrix C contains a linear superposition of elements $\phi_n(v_{xk})$ and $\phi_n(-v_{xk})$ that transpose individually according to the parity of ϕ_n.[10] Finally, the boundary vector (3.10) contains elements $v_{xk}f_o(v_{xk})$, and like the spectral matrices, are two-fold symmetric, transposing with odd parity.

After evaluation of the spectral matrices and boundary vector, the entire set of FD-spectral equations is ready for solution. The set constitutes a large,

[9]Functions ϕ_n and ϕ'_n always have opposite parity.

[10]Closer inspection of Eq. (3.13) reveals that $\{C\}_{k+(N/2)\,n} = -\{C\}_{kn}$ if ϕ_n is odd; if ϕ_n is even, $\{C\}_{kn} = 0$ for all k.

block tridiagonal matrix equation with the structure[11]

$$\begin{pmatrix} \boldsymbol{R}_2 & \boldsymbol{S}_2 & & & & & & & \\ \boldsymbol{Q} & \boldsymbol{R}_3 & \boldsymbol{S} & & & & & & \\ & \boldsymbol{Q} & \boldsymbol{R}_4 & \boldsymbol{S} & & & & & \\ & & \cdot & \cdot & \cdot & & & & \\ & & & \cdot & \cdot & \cdot & & & \\ & & & & \cdot & \cdot & \cdot & & \\ & & & & & \boldsymbol{Q} & \boldsymbol{R}_{L-3} & \boldsymbol{S} & \\ & & & & & & \boldsymbol{Q} & \boldsymbol{R}_{L-2} & \boldsymbol{S} \\ & & & & & & & \boldsymbol{Q}_{L-1} & \boldsymbol{R}_{L-1} \end{pmatrix} \begin{pmatrix} \boldsymbol{\alpha}_2 \\ \boldsymbol{\alpha}_3 \\ \boldsymbol{\alpha}_4 \\ \cdot \\ \cdot \\ \cdot \\ \boldsymbol{\alpha}_{L-3} \\ \boldsymbol{\alpha}_{L-2} \\ \boldsymbol{\alpha}_{L-1} \end{pmatrix} = \begin{pmatrix} \boldsymbol{\beta} \\ \mathbf{0} \\ \mathbf{0} \\ \cdot \\ \cdot \\ \cdot \\ \mathbf{0} \\ \mathbf{0} \\ \mathbf{0} \end{pmatrix}. \tag{3.14}$$

Expansion coefficient vectors $\boldsymbol{\alpha}_1, \cdots, \boldsymbol{\alpha}_L$ and boundary vector $\boldsymbol{\beta}$ are of length N. Matrix block elements—$\boldsymbol{R}_2, \cdots, \boldsymbol{R}_{L-1}$, $\boldsymbol{S}$, $\boldsymbol{S}_2$, $\boldsymbol{Q}$, and $\boldsymbol{Q}_{L-1}$—are of dimension $N \times N$. By inspection, matrix Eq. (3.14) has a large $LN^2 \times LN^2$ coefficient matrix; fortunately, the system is sparse—that is, most of the matrix entries are zero. This system can be solved efficiently using block Gaussian elimination, details of which are deferred to Appendix C.5. In short, block Gaussian elimination involves two steps. The first, forward elimination, converts the system of equations into one which is block upper-triangular. Forward elimination proceeds block row by block row for L rows, each row operation requiring an order N^3 matrix inversion [15].[12] Round-off error (see the next section) during matrix inversion is minimized through partial pivoting [15]. The second step, back substitution, involves a series of M, order N^2, matrix-vector recursions to construct the final solution vector $(\boldsymbol{\alpha}_2, \cdots, \boldsymbol{\alpha}_{L-1})^T$.

3.1.3.4 Numerical Errors

Round-off and discretization errors have been examined in Chapter 2 for Rees's method and the finite-difference method (see Section 2.1.3.4). The FD-spectral method is also subject to these errors.

Round-off error can be significant when the FD-spectral equations are solved directly, by Gaussian elimination. The principal contribution to round-

[11] Block elements derive directly from Eqs. (3.7), (3.10), and (3.11). Note, also, coefficient matrix entries off the three block diagonals are zero.

[12] "Order" refers here to number of multiplications. Multiplication is the dominant computational operation in these calculations.

off error occurs during forward elimination, this being an order LN^3 process once completed. Because the elimination proceeds from the top to bottom row, round-off error tends to "trickle" top to bottom, with the latter elements of the solution vector $(\alpha_{L-1}, \alpha_{L-2}, \cdots)$ accumulating the largest amount of error. This type of error can be monitored and in some cases controlled if calculations are carried out in double precision, in which the number of binary digits per variable is doubled.[13] Instead of resorting to double precision, round-off error in the present calculation was monitored by means of a consistency check. Once the solution vector is determined, the matrix-vector multiplication on the left side of (3.14) is performed, which is only an order MN^2 process. The result is then compared with the right side of (3.14). Any differences are attributable to round-off error. It has been found using this check that the magnitude of the vector difference between right and left sides is usually less than one part in one thousand (see Section 3.1.4.3 for typical simulation conditions).

Discretization error occurs because of the discrete representation of a continuous space variable in the finite-difference approximation, and from the finite, truncated representation of an infinite, mathematically complete basis set in the spectral approximation. Space and velocity discretization error can be monitored in the same spirit as that followed in Chapter 2. Distribution functions, calculated using formula (3.6), are compared for successively smaller space increment Δx and larger basis set number N. If the changes in the distribution function are small then discretization error is correspondingly small. Moreover, the question as to whether there are enough basis functions is readily answered by noting the behavior of the expansion vector elements $\{\alpha_i\}_n$. From general principles, adequate spectral resolution, or equivalently, low velocity discretization error is attained if only the high-order elements $(n \approx N)$ of each expansion vector $(\alpha_i,\ i = 2, \cdots, L-1)$ decay smoothly to zero. Last of all, the foregoing error monitoring procedures are limited only by the capabilities of the computer system, namely, memory size and execution rate.

[13]The HP-1000F minicomputer has as word length of sixteen bits. Two words are used to represent real variables, a twenty-four-bit mantissa and an eight-bit exponent, in single precision. Double precision uses four words, a fifty-six-bit mantissa and an eight-bit exponent.

3.1.4 Results and Discussion

3.1.4.1 Execution Rate

As usual, all computations were performed on an HP-1000F minicomputer (see Section 2.1.4.1). An entire FD-spectral calculation consists of two separate "subcalculations": spectral matrix evaluation and subsequent Gaussian elimination of the FD-spectral equations.

The spectral matrix calculation entails evaluation of four block elements in (3.14), S, S_2, Q, and Q_{L-1}; two constituent matrices for R_i,[14] A and C; and lastly, the boundary vector β. Thirty basis functions were used in most computations. To accommodate all the spectral matrices in computer memory, a disk-swapping virtual memory feature EMA (extended memory access) was implemented. Despite some of the inefficiencies associated with EMA, a thirty-basis-function spectral matrix evaluation executed in ten to fifteen seconds real time.

Overall calculation time was dominated by Gaussian elimination. Memory enhancement was achieved, as before, through EMA. An additional feature denoted VIS (vector instruction set) was used. This feature reduces matrix and vector operation times by means of microcoding.[15] Gaussian elimination of the FD-spectral equations typically took from one to two minutes of computer time, for an eighty-point space discretization line and a thirty-element basis set ($L = 80,\ N = 30$).

3.1.4.2 Solution Verification

Verification of FD-spectral solutions was carried out in much the same way as that for the (x, v_x, t) problem. A three-level scheme was implemented, encompassing tests without collisions (ballistic), tests with collisions, and tests based on qualitative physical reasoning. All calculations used a Tchebycheff basis set and were performed at maximum space and velocity resolution, $L = 80$ and $N = 30$. Whenever possible, comparisons with the steady-state solutions of Chapter 2's (x, v_x, t) problem were made for additional verification.

[14]The matrices R_i, $i = 2, \cdots, L-1$, are never stored, but calculated as needed from V, A, C, and qE_{xi}/m^*.

[15]In combination, the rate-reducing EMA and the rate-increasing VIS features result in an effective execution rate comparable to the baseline execution rate of 0.05 MFLOPS.

Under ballistic conditions, in which the collision term is dropped, and for constant electric fields, the FD-spectral solutions were compared with exact analytical solutions derived in Appendix F [Eqs. (F.13) and (F.14)] . As has been previously observed for the finite-difference calculations of Chapter 2, agreement between numerical and analytical solutions was good. Negative electric-field solutions agreed to within one percent. Positive electric-field solutions agreed less well to within ten percent, attributable to difficulties in the spectral resolution of ballistic shock discontinuities.

This discontinuity resolution issue deserves further attention. Figure 3.2 compares exact and numerical solutions for propagation of a boundary-injected step discontinuity under a ten-term Hermite-Gaussian spectral expansion. The distribution function is spatially constant and is plotted against v_x. Collocation points are depicted by circles. Collisions are neglected and the electric field is set to zero. Carriers are injected with Maxwellian distribution only at the boundary $x = 0$. The FD-spectral solution oscillates rapidly near the step discontinuity. This behavior is reminiscent of the Gibbs phenomenon encountered in Fourier theory [25]. Note, however, that the numerical solutions are extremely accurate near each collocation point.[16] This test not only examines resolution characteristics but also reveals the inherent mathematical robustness of the FD-spectral algorithm when subject to severe conditions.

Once the ballistic solutions of BTE (3.1) have been verified, the collision term Cf can be included for further verification. Although simple in form, the collision operator was checked for proper translation to computer code by numerical evaluation of the identity $\{C\}_{k1} = 0$ ($\phi_1 \propto f_o$, similar to that described in Section 2.2.4.2)

Additional verification by direct comparison with steady-state finite-difference solutions of Chapter 2 yielded acceptable results. Errors ranged from one to three percent over the entire (x, v_x) domain. These comparisons were made in a variety of cases—ballistic, collision-dominated conditions; uniform, nonuniform electric fields; and so forth.

To complete the verification process, FD-spectral equations were studied to see whether their properties concurred with those deduced from physical reasoning. Solutions were checked to ensure that they obeyed boundary conditions, the x component of current density was monitored for spatial

[16]This is expected because the residual $R(v_x)$ vanishes exactly at the collocation points $v_x = v_{xk}$.

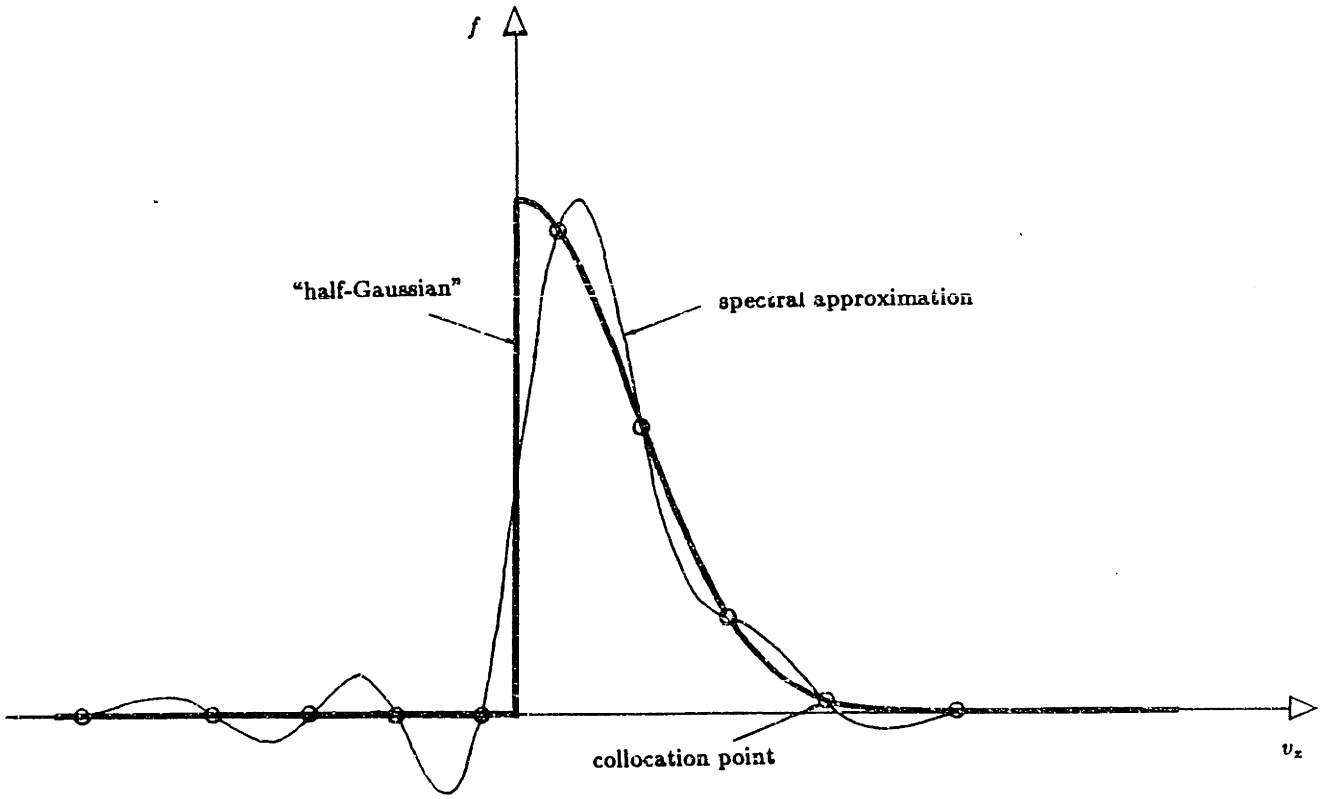

Figure 3.2. Exact and numerical solutions for ballistic propagation of a boundary-injected step discontinuity.

Quantity	*Value*	*Units*
Number of basis functions, N	30	—
Number of z points, L	80	—
Cell size, Δz	1.25×10^{-8}	meters
Average roundoff error in $\lvert\alpha_i\rvert$	$\sim 10^{-3}$	—

Table 3.1: Computational parameters for the (x, v_x) problem.

invariance (see the end of Section 2.2.4.3), and collisions were observed to symmetrize the distribution function. For the most part, all solutions varied in a continuous, systematic manner throughout their domain, as anticipated. Under circumstances where step discontinuities in the velocity dependence of the distribution function occur, physical arguments assert that increasing the scattering strength (S_{qe}) tends to attenuate and smooth the discontinuity. This tendency has been directly confirmed.

3.1.4.3 Numerical Solutions

Results from a typical FD-spectral calculation for solution of BTE (3.1) will be presented. Physical parameter, computational parameters, and the potential distribution were chosen so as to obtain exact correspondence with the finite-difference calculation of Section 2.2.4.3. Results from the Chapter 2 finite-difference calculation should therefore be compared with the ones given here.

Physical parameters are identical to those of Table 2.3. Table 3.1 displays the computational parameters. Results are for a Tchebycheff basis set, although Fourier and Hermite-Gaussian sets yielded similar results. Only fourteen basis set elements were needed in order to achieve an accuracy comparable to Chapter 2's finite-difference method, thus underscoring this method's numerical efficiency.

The electric field and potential distribution were the same as those used previously, and have been plotted in Fig. 2.6. The cusped form of the potential and the consequent step discontinuity in electric field will test the solution method under severe, though somewhat unphysical, conditions.

Plotted in Fig. 3.3 is the velocity dependence of the distribution function for a series of spatial positions, ranging from the entrance region $x \approx 0$ to the exit region $x \approx L_x$. As an initial comment, notice the close similarity

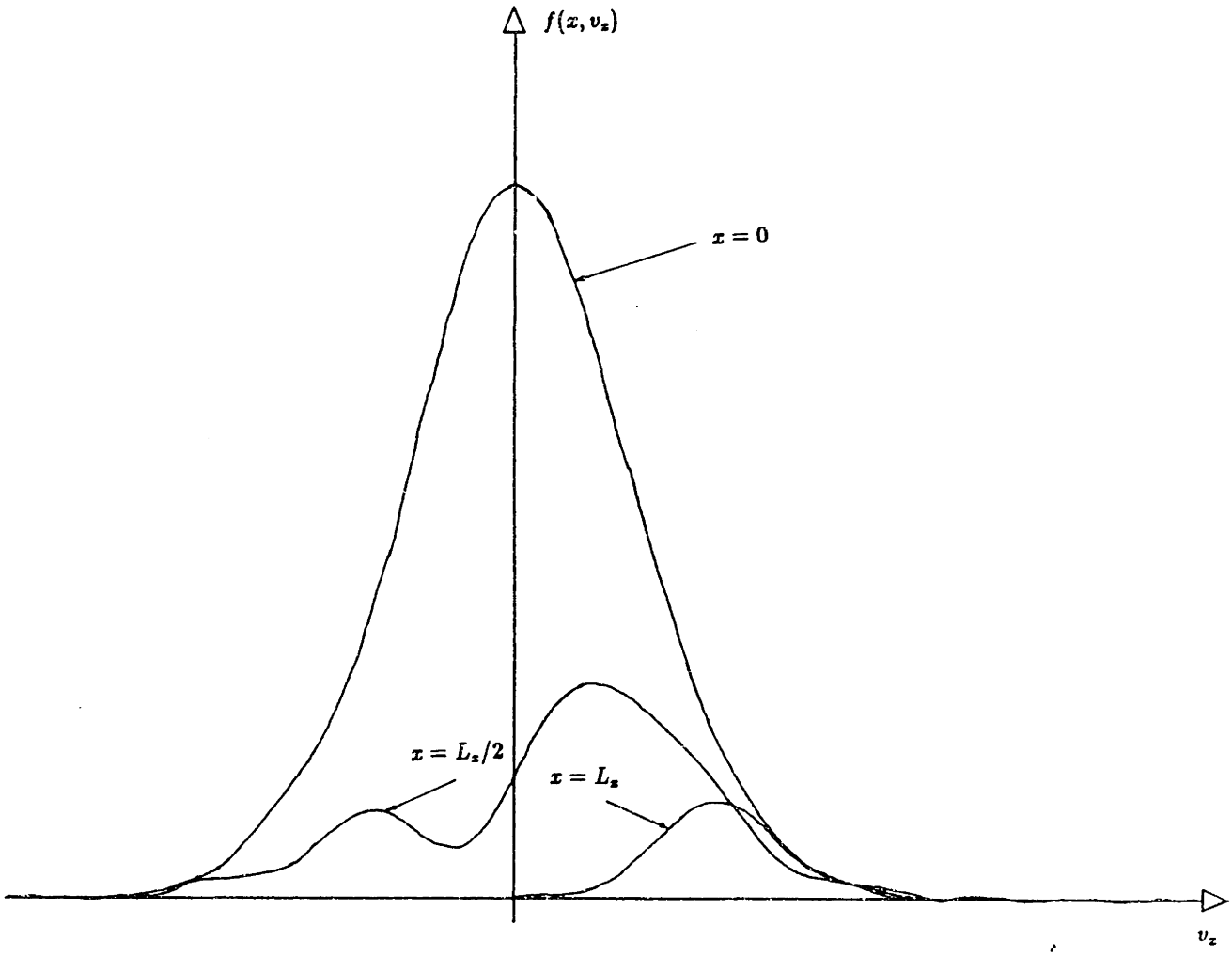

Figure 3.3. Carrier distribution versus v_x, parameterized from $x = 0$ to $x = L_x$.

between Fig. 3.3 and the finite-difference solution of Fig. 2.7. Direct comparison has shown that both solutions agree to within one percent at entrance and exit regions, while expectedly agreeing less well, to within three percent, in the transition region $x \approx L_x/2$. Boundary conditions are all satisfied. The distribution function vanishes at large positive and negative velocities; at the entrance $x = 0$ it is an equilibrium Maxwellian for $v_x > 0$, and at the exit $x = L_x$ no carriers are injected, so that it vanishes for $v_x < 0$. Similar to observations previously made in Section 2.2.4.3 for the (x, v_x, t) problem, the carrier velocity distribution changes shape from a quasi-equilibrium Maxwellian in the entrance region, to an nonequilibrium asymmetric function in the exit region, changing rapidly in the central transition region. The symmetrizing effect of scattering is clearly evidenced by the bimodal shape of the distribution in transition and exit regions. Section 2.2.4.3 contains a more complete discussion of the results described here, including details pertaining to the underlying microscopic physical processes that are involved.

Current density along the x direction was determined by evaluating the first moment of the distribution function according to Appendix I. Current densities varied, on average, three percent from the mean, with maximum deviation just after and minimum deviation just before the potential cusp, both within five percent of mean. This behavior supports the closing remarks of Chapter 2 and reflects the nonconservative nature of the FD-spectral algorithm. Increasing, singly or simultaneously, the number of space points and basis functions has been found to reduce current density variation[17]; nevertheless, these solutions are accurate enough for the purposes at hand. Moreover, current density variation serves as an indicator of absolute numerical error. These issues will be reexamined towards the end of this chapter.

To conclude this section, which represents the first application of the FD-spectral method, the carrier distribution will be viewed from a different, but equivalent, perspective—transform space. From (3.14), it is apparent that the FD-spectral method makes available the distribution function expansion coefficients at each discrete space point. These expansion coefficients are, by definition, the carrier distribution basis-function transform with respect to velocity. Figure 3.4 depicts the Tchebycheff transform of this section's sample calculation. Expansion coefficients of increasing order $(\alpha_1, \alpha_2, \cdots, \alpha_N)$ are depicted with bar lines at a space point in entrance, transition, and exit

[17] In theory, current density is exactly constant if $L \to \infty$ and $N \to \infty$.

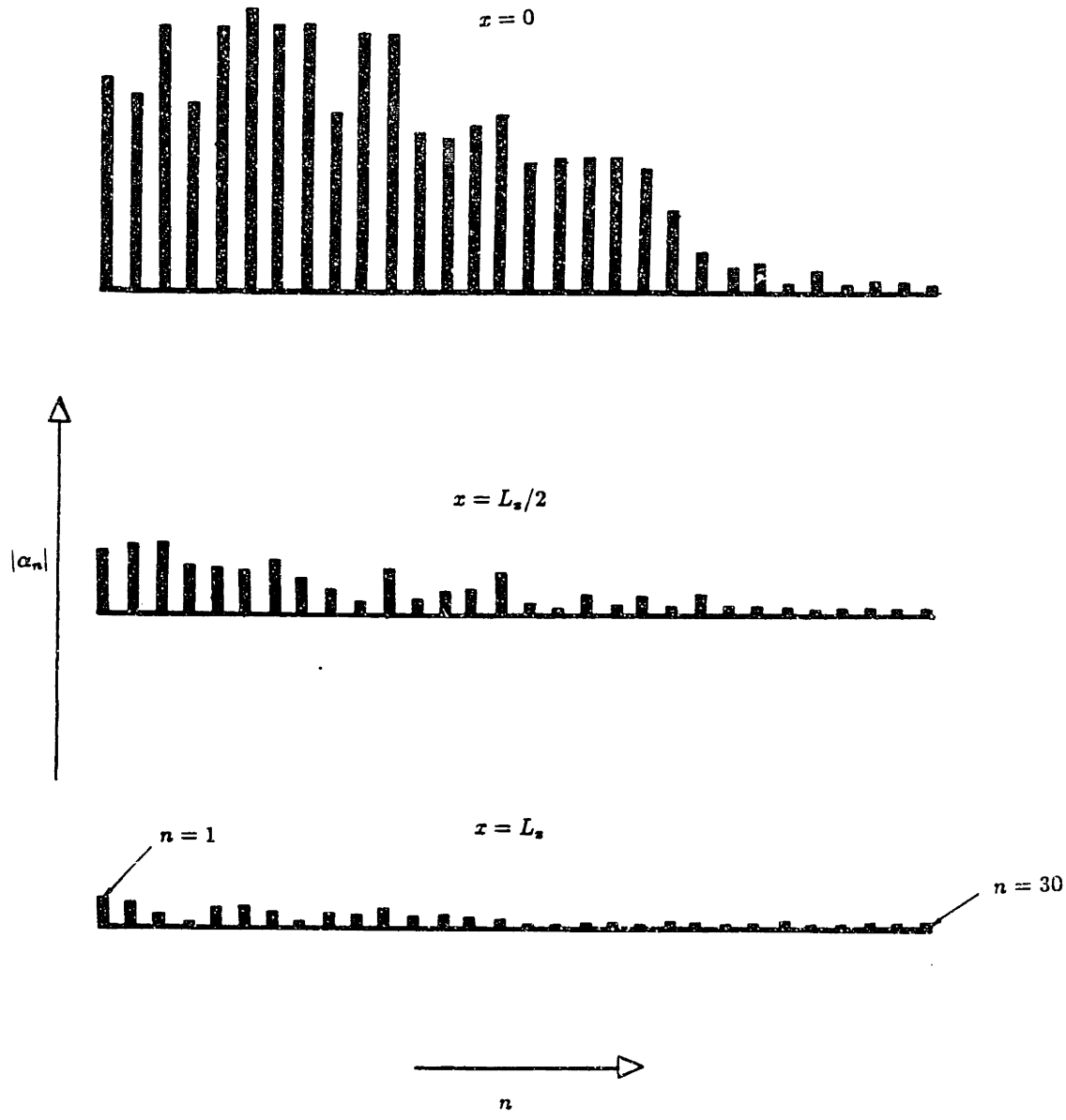

Figure 3.4. Tchebycheff transform of the carrier distribution in entrance, transition, and exit regions.

regions. In the entrance region, the carrier distribution is well approximated by a Gaussian (that is, an equilibrium Maxwellian) function. Correspondingly, the Tchebycheff set resolves this function with a Gaussian-like expansion coefficient distribution in transform space.[18] In transition and exit regions, the nonequilibrium character of the distribution function is manifested by an oscillation in transform space. As a final note, the decay in expansion coefficient magnitude with increasing order implies good spectral resolution and is therefore a positive indication of solution accuracy.

3.2 The (z, v_ρ, v_z) Problem

In the first half of this chapter the FD-spectral method has been established. The BTE was solved for a system with variation in a single space and velocity dimension, and included a simple fictitious scattering mechanism. In the second half of this chapter, the FD-spectral method will be extended to a system with variation in an additional velocity dimension, and also, physically realistic phonon scattering mechanisms will be included.

Introductory remarks of Section 2.1 conclude that a physically realistic,[19] spatially homogeneous system with a z-directed electric field has a carrier distribution that is cylindrically symmetric in velocity. The same can be concluded about a physically realistic system with additional variation along the z-axis. If such a system is time independent the distribution function takes the form $f = f(z, v_\rho, v_z)$ and the electric field can be written $\boldsymbol{E} = E_z(z)\hat{\boldsymbol{e}}_z$. The BTE for this system follows from general Eq. (1.2) and is similar to (3.1) in structure:

$$-v_z\frac{\partial f}{\partial z} - \frac{qE_z}{m^*}\frac{\partial f}{\partial v_z} + Cf = 0. \tag{3.15}$$

[18] An analogy can be made here with Fourier theory. The Fourier transform of a Gaussian is also a Gaussian, and the corresponding halfwidths are inversely related.

[19] The term "physically realistic" is used here to denote semiclassical systems where carriers are free to move in *three* spatial dimensions. In this work only the previous (x, v_x) problem and Chapter 2's (x, v_x, t) problem are not physically realistic owing to the fact that carriers are artificially constrained to move along a single spatial dimension.

3.2.1 The FD-Spectral Method

3.2.1.1 Velocity Discretization

As was done in the preceding (x, v_x) problem, the distribution function can be approximated with a spectral series expansion in N basis functions Φ_n, all dependent on the vector velocity variable $\boldsymbol{v} = v_\rho \hat{\boldsymbol{e}}_\rho + v_z \hat{\boldsymbol{e}}_z$,

$$f(z, \boldsymbol{v}) \approx \sum_{n=1}^{N} \alpha_n(z) \Phi_n(\boldsymbol{v}). \tag{3.16}$$

Spatial variation in this problem is expressed by the argument of each expansion coefficient α_n. Expansion (3.16) is somewhat indeterminate since it does not specify the mathematical structure of $\Phi_n(\boldsymbol{v})$. An obvious choice for these basis functions is a sequence of products generated from the monodimensional set of Section 3.1.1.1; hence, Eq. (3.16) is equivalent to the double series expansion[20]

$$f(z, \boldsymbol{v}) \approx \sum_{\ell=1}^{N_\ell} \sum_{m=1}^{N_m} \alpha_{\ell m}(z) \phi_{2\ell}(v_\rho) \phi_m(v_z). \tag{3.17}$$

The subscripts 2ℓ and m denote the order of each monodimensional basis element (see the end of Section 3.1.1.1). Because of the distribution function's inherent even parity in v_ρ, (3.17) includes only the first N_ℓ even v_ρ-dependent constituent functions. In addition, a direct connection between the global index n and the local indices ℓ and m can always be established: $\alpha_n = \alpha_{\ell(n)m(n)}$ or, inverting the index transformation, $\alpha_{\ell m} = \alpha_{n(\ell,m)}$.[21] Global and local index limits are further related by $N = N_\ell N_m$. Expansions (3.16) and (3.17) are simply the multi-dimensional generalization of (3.2). As a last remark, the basis set Φ_n is mathematically complete on account of the constituent functions $\phi_{2\ell}$ and ϕ_m being themselves complete.

Expansion (3.16) implies, for a given basis set, the distribution function is determined by a finite number of parameters, the expansion coefficients α_n. An N-element, spatially dependent vector made up of expansion coefficients

[20]This expansion is analogous to that found in the Fourier treatment of multi-dimensional functions [25].

[21]Many index transformations—$\ell(n), m(n)$, and $n(\ell, m)$—are conceivable, their sole requirements being that they map, in a one-to-one fashion, the N_ℓ elements of $\phi_{2\ell}$ and N_m elements of ϕ_m onto the N elements of Φ_n.

can represent the carrier distribution. Therefore, under spectral velocity discretization the distribution function transforms to a vector field as follows:

$$f(z,v) \longrightarrow \alpha(z), \tag{3.18}$$

$$\{\alpha(z)\}_n = \alpha_n(z),$$
$$n = 1, \cdots, N.$$

3.2.1.2 Space Discretization

Space discretization is carried through using the finite-difference method (compare with Section 3.1.1.2). The variable z is sampled at L finite-difference points z_i. The carrier distribution, and thus the coefficient vector $\alpha(z)$, is assumed constant within an interval Δz about each sampled point. Expressed in mathematical form,

$$\alpha(z) \longrightarrow \alpha_i, \tag{3.19}$$

$$z_i = z_o + i\Delta z,$$
$$i = 1, \cdots, L.$$

Along with this discretization, samples of the electric field must be taken:

$$E_z(z) \dashrightarrow E_{zi}. \tag{3.20}$$

Once space and velocity have been discretized, the discrete version of the continuous distribution function follows from

$$f_i(v) = \sum_{n=1}^{N} \{\alpha_i\}_n \Phi_n(v). \tag{3.21}$$

Alternatively, formula (3.21) can be written in double series form with the use of (3.17).

3.2.1.3 FD-Spectral Equations

Equations for the α_i, the FD-spectral equations, are developed exactly as described earlier in Section 3.1.1.3, with the exception of a few minor modifications. Expansion (3.16) is substituted into the governing equation (3.15). Collocation sets the vector velocity residual $R(v_k)$ to zero at N points[22] $(v_{\rho k}, v_{zk})$, $k = 1, \cdots, N$, defined by the positive extrema of $\phi_{2N_\ell}(v_\rho)$ and the positive and negative extrema of $\phi_{N_m}(v_z)$. To avoid the collection point $v_z = 0$, N_m is taken even.

Before writing the FD-spectral equations, their numerical domain deserves brief attention. Schematized in Fig. 3.5 is the numerical mesh that pertains to this problem. It comprises finite-difference and collocation points. The mesh exists in a three-dimensional region, and is depicted by an aggregate of planes, defined by the collocation points and positioned at each finite-difference point. There are only two types of mesh points, boundary points, on planes associated with space-velocity boundaries ($i = 1$ and $i = L$), and internal points, on all other remaining planes.

Since (3.1) and (3.15) have similar form, their resulting FD-spectral equations are also similar. For each internal point, using the notation of Section 3.1.1.3,

$$-V\Delta_z^{\pm}\alpha_i - \frac{qE_{zi}}{m^*}A\alpha_i + C\alpha_i = 0, \qquad (3.22)$$
$$i = 2, \cdots, L-1,$$

where $\Delta_z^{\pm}$ is defined like $\Delta_z^{\pm}$ in (3.9) but with v_{zk} replaced by v_{zk}. This set of coupled vector difference equations is identical in form to that of (3.7). In terms of the global index n,

$$\begin{aligned} \{V\}_{kn} &= v_{zk}\Phi_n(v_{zk}), \\ \{A\}_{kn} &= \frac{\partial \Phi_n}{\partial v_z}(v_{zk}), \\ \{C\}_{kn} &= C[\Phi_n(v_{zk})], \end{aligned} \qquad (3.23)$$
$$k, n = 1, \cdots, N.$$

Elements of matrix A can be further simplified by resorting to local indices, which gives $\partial\Phi_n(v_{zk})/\partial v_z = \phi_{2\ell(n)}(v_{\rho k})\phi'_{m(n)}(v_{zk})$. The integrals involved in

[22] Collocation points are located by vectors v_k for which $v_k = v_{\rho k}\hat{e}_\rho + v_{zk}\hat{e}_z$.

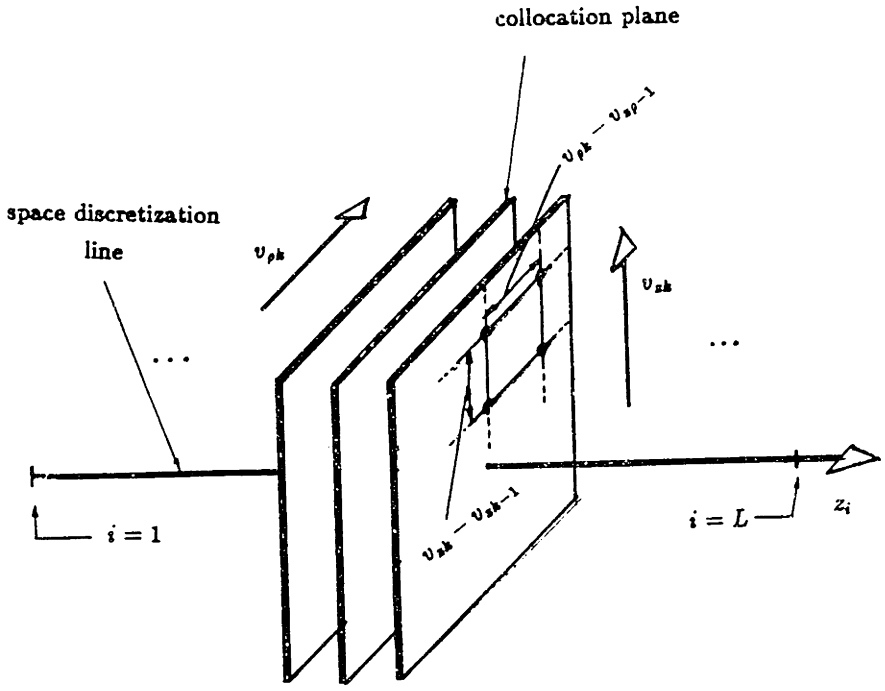

Figure 3.5. FD-spectral discretization mesh for the (z, v_ρ, v_z) problem.

$C[\Phi_n(v_{zk})]$ will be approximated in Section 3.2.2.2 by a Gaussian quadrature, thus converting the continuous operator C into a discrete operator C_d.

Alternate equations apply for coupling to boundary points with $i = 1$ and $i = L$. An equilibrium Maxwellian distribution of carriers is injected from the left boundary (refer to Fig. 3.5 for orientation), while no carriers are injected from the right boundary. Therefore, coupling to boundary points is effected through

$$\{V\alpha_1\}_k = v_{zk} f_o(v_k), \tag{3.24}$$

$$k = 1, \cdots, (N/2),$$

and

$$\{V\alpha_L\}_k = 0, \tag{3.25}$$

$$k = (N/2) + 1, \cdots, N,$$

where

$$f_o(v_k) = \mathcal{N} \exp\left(-\frac{m^*}{2k_B T} v_k^2\right). \tag{3.26}$$

Here, $v_k = (v_{\rho k}^2 + v_{zk}^2)^{1/2}$ is the magnitude of v_k and $\mathcal{N}$ is a suitable normalization constant. Also, an even number of symmetrically located collocation points labeled $k = 1, \cdots, N/2$ for $v_{zk} > 0$ and $k = (N/2) + 1, \cdots, N$ for $v_{zk} < 0$ has been assumed.

Before beginning the next section, attention must be paid to one final detail. All through this treatment, boundary equations for large velocity regions, or more precisely for points at the plane edges in Fig. 3.5, were purposefully neglected (see the end of Section 3.1.1.3 for comparison). If a basis set is selected with the property that all its elements vanish for infinite velocity magnitude, the corresponding boundary conditions will always be satisfied and no additional boundary equations are required. It is this assumption, $\Phi_n(v) \to 0$ as $v \to \infty$, that has been implicit in the foregoing treatment and will be adhered to for the remainder of this work.

3.2.2 The Collision Matrix

Elements of the collision matrix, C, have to be evaluated in order to implement the FD-spectral method. To obtain approximate correspondence to

a single-valley model for silicon, scattering due to (intra-valley[23]) deformation-potential acoustic and nonpolar optic phonons will be taken into account. This will also test the performance of the FD-spectral method when multiple scattering mechanisms are present. Nonpolar optic and deformation-potential acoustic scattering arise from lattice distortions accompanying optic and acoustic lattice waves, respectively. Although similar in physical origin to polar-optic phonon scattering, presented in Section 2.1.2.1, these scattering mechanisms are not predicated upon lattice ion polarization. Appendix E, from which all of this section's formulas are taken, should be consulted for additional information concerning these scattering mechanisms.

3.2.2.1 Deformation-Potential Acoustic and Nonpolar Optic Scattering Rates

The probability-scattering rate associated with deformation-potential acoustic phonons is given in Appendix E and is rewritten here [Eq. (E.6)]:

$$S_a(\boldsymbol{v}, \boldsymbol{v}') = \frac{(m^*)^3 k_B T \Xi_a^2}{(2\pi)^2 \rho u^2 \hbar^4} \delta(\varepsilon' - \varepsilon), \tag{3.27}$$

Some of the above quantities have been defined previously; Ξ_a is the acoustic-deformation-potential interaction constant, ρ is the crystal density, and u is the acoustic wave speed (the speed of sound) in the semiconductor. The collision process is approximated as being elastic, which means initial and final carrier kinetic energies are assumed equal[24]; thus phonon absorption and emission processes can be combined. Notice, too, that unlike polar-optic phonon scattering, the collisions are isotropic and therefore the orientation of the scattered vector velocity is uncorrelated with respect to the initial orientation.

Nonpolar optic phonon scattering is an inelastic, isotropic process which, like polar-optic phonon scattering, includes both phonon absorption and phonon emission terms. From Appendix E [Eq. (E.14)] the scattering prob-

[23]Scattering processes can can be either intra- or inter-valley. Because of the single-valley assumption, all inter-valley processes transform into effective intra-valley processes.

[24]Actually, $|\varepsilon' - \varepsilon| = \hbar\omega_a(q)$ where $\hbar\omega_a(q)$ is the energy of the acoustic phonon of wavevector q involved in the collision (see footnote 10, Chapter 2, and references [8,10]).

ability rate is

$$S_o(\boldsymbol{v},\boldsymbol{v}') = \frac{(m^*)^3\Xi_o^2}{8\pi^2\rho\omega_o\hbar^3}\begin{cases} N_o\delta(\varepsilon'-\varepsilon-\hbar\omega_o) & \text{(absorption)} \\ (N_o+1)\delta(\varepsilon'-\varepsilon+\hbar\omega_o) & \text{(emission).}\end{cases} \tag{3.28}$$

The expression Ξ_o is the nonpolar optic phonon interaction constant, ω_o is the optic phonon angular frequency, and $\hbar\omega_o$ is the associated phonon energy. The Bose-Einstein occupancy factors depend on temperature and optic phonon energy: $N_o = [\exp(\hbar\omega_o/k_BT)-1]^{-1}$.

Total acoustic and optic scattering rates ensue after integration of (3.27) and (3.28) over all final velocity states $\boldsymbol{v}'$. For acoustic phonon scattering [Eq. (E.7)]

$$\lambda_a(\varepsilon) = \frac{\sqrt{2}(m^*)^{3/2}k_BT\Xi_a^2}{\pi\rho u^2\hbar^4}\sqrt{\varepsilon} \quad \text{(absorp. and emission)}, \tag{3.29}$$

and for optic phonon scattering [Eq. (E.15)]

$$\lambda_o(\varepsilon) = \frac{(m^*)^{3/2}\Xi_o^2}{\sqrt{2}\pi\rho\omega_o\hbar^3}\begin{cases} N_o\sqrt{\varepsilon+\hbar\omega_o} & \text{(absorption)} \\ (N_o+1)\sqrt{\varepsilon-\hbar\omega_o}\;u(\varepsilon-\hbar\omega_o) & \text{(emission)}\end{cases} \tag{3.30}$$

These total scattering rates, like those for polar optic scattering, depend only on initial carrier kinetic energy, $\varepsilon = m^*v^2/2$. The total acoustic scattering rate varies as the square root of energy and hence is proportional to the magnitude of initial carrier velocity. This indicates a constant-mean-free-path collision process for which $\ell_{mfp} = \sqrt{2m^*}k_BT\Xi_a^2/\rho u^2\hbar^2$ [8]. In contrast, the mathematical form of (3.30) does lend itself to a simple constant-mean-free-path description; in fact, the optic-phonon mean free path is noticeably energy dependent.

3.2.2.2 Matrix Elements

Scattering rates (3.27) through (3.30) specify the action of the, up until now, generic collision operator C. The action of the collision operator on a basis set element, taking into account cylindrical velocity symmetry, is

$$
\begin{aligned}
C[\Phi_n(v)] &= S_a \int_{-v}^{v} d\xi\ \phi_{2\ell(n)}(\sqrt{v^2-\xi^2})\phi_{m(n)}(\xi) \\
&+ S_o^-(v) \int_{-(v^2-v_o^2)^{1/2}}^{(v^2-v_o^2)^{1/2}} d\xi\ \phi_{2\ell(n)}(\sqrt{v^2-v_o^2-\xi^2})\phi_{m(n)}(\xi) \\
&+ S_o^+ \int_{-(v^2+v_o^2)^{1/2}}^{(v^2+v_o^2)^{1/2}} d\xi\ \phi_{2\ell(n)}(\sqrt{v^2+v_o^2-\xi^2})\phi_{m(n)}(\xi) \\
&- \lambda_a(\varepsilon)\Phi_n(v) - \lambda_o^-(\varepsilon)\Phi_n(v) - \lambda_o^+(\varepsilon)\Phi_n(v), \qquad (3.31)
\end{aligned}
$$

where $v_o = (2\hbar\omega_o/m^*)^{1/2}$ is the carrier velocity corresponding to the optic-phonon energy. Scattering factors S_a, S_o^-, and S_o^+ are written out in Appendix E [Eqs. (E.8), (E.9), (E.16), (E.18) and (E.19)]. The first three members on the right side of (3.31) represent acoustic and optic phonon in-scattering contributions, and the remaining members represent the corresponding out-scattering contributions in which λ_o^- and λ_o^+, respectively, designate the absorption and emission entries of (3.30).

Closed-form expressions for the integrals in (3.31) are generally not available. To overcome this difficulty, Gaussian quadrature integration is performed (see Appendix C.2). The net effect is to convert a continuous collision operator into a discrete one, C_d, whereupon the working formula for the collision matrix elements becomes

$$
\begin{aligned}
\{C\}_{kn} &= C_d[\Phi_n(v_k)] \\
&= S_a \sum_\mu w_\mu \phi_{2\ell(n)}(\sqrt{v_k^2-\xi_\mu^2})\phi_{m(n)}(\xi_\mu) \\
&+ S_o^-(v_k) \sum_\mu w_\mu \phi_{2\ell(n)}(\sqrt{v_k^2-v_o^2-\xi_\mu^2})\phi_{m(n)}(\xi_\mu) \\
&+ S_o^+ \sum_\mu w_\mu \phi_{2\ell(n)}(\sqrt{v_k^2+v_o^2-\xi_\mu^2})\phi_{m(n)}(\xi_\mu) \\
&- \lambda_a(\varepsilon_k)\Phi_n(v_k) - \lambda_o^-(\varepsilon_k)\Phi_n(v_k) - \lambda_o^+(\varepsilon_k)\Phi_n(v_k). \qquad (3.32)
\end{aligned}
$$

Above, $\varepsilon_k = m^* v_k^2/2$, and quadrature is over an interval centered with respect to the origin $\xi = 0$, with weights w_μ and samples ξ_μ. Sum limits are determined through correspondence with integral limits in (3.31).

3.2.3 Numerical Implementation

3.2.3.1 Space Discretization Line

FD-spectral solution of this (z, v_ρ, v_z) problem was carried out in essentially the same way as that of the previous (x, v_x) problem. Specification of the space discretization line is identical to that of Section 3.1.3.1: the discretization line is divided into a maximum of eighty ($L = 80$) uniform, fixed cells with width Δz and centered at z_i $(1 = 1, \cdots, L)$.

3.2.3.2 Basis Set

Experience gained from solution of the (x, v_x) problem suggests that Hermite-Gaussian functions form a particularly desirable basis set. As opposed to Fourier and Tchebycheff sets, a Hermite-Gaussian set provides good mid-interval velocity resolution (see Section 3.1.3.2). This is a key requirement for approximating the more important distribution function features commonly found in semiconductor devices. The Hermite-Gaussian set has an added benefit in that large velocity ($v \to \infty$) boundary conditions are automatically satisfied. And further, this set is especially effective when the carrier distribution is near thermal equilibrium.[25] For these reasons and an additional one of standardization, Hermite-Gaussian functions constitute the set of choice, here and in the next chapter.

In subsequent numerical calculations, thirty basis functions are used, generated from combination of the first three even, v_ρ-dependent, and ten, even and odd, v_z-dependent Hermite-Gaussian constituent functions.

3.2.3.3 Solution of FD-Spectral Equations

Equations (3.22) and boundary equations (3.24) and (3.25) make up a system of coupled vector difference equations. Solution proceeds, as before, by direct Gaussian elimination. Elaboration of the solution technique, how-

[25] A sequence of Hermite-Gaussian functions can have any independent variable scale (see Appendix G). To determine a specific scale factor, the first-order element Φ_1, itself a Gaussian, is matched to the equilibrium Maxwellian function. Choosing the independent variable scale in this way is by no means obligatory. In theory, any fixed scale factor will do; however, a poor choice will necessitate a comparatively large number of basis set elements to achieve sufficient accuracy.

ever, will be postponed until the the topic of spectral matrix evaluation has been covered.

Collocation mesh symmetry must first be examined. The collocation mesh is defined by the N coordinate pairs $(v_{\rho k}, v_{zk})$. The collocation domain encompasses the semi-infinite plane $0 < v_\rho < +\infty$ and $-\infty < v_z < +\infty$, where the collocation points are symmetrically located about the line $v_z = 0$. If the spectral matrices—V, A, and C—are row ordered $(v_{\rho k+(N/2)}, v_{zk+(N/2)}) = (v_{\rho k}, -v_{zk})$ for $k = 1, \cdots, N/2$, then their two-fold row-symmetric structure is clearly exposed.

The symmetry of each spectral matrix manifests itself in much the same way as that already discussed in Section 3.1.3.3 for the (x, v_x) problem and, therefore, will lead to a joint savings in computer memory storage and calculation time. Each spectral matrix possesses a symmetry in which elements from the first $N/2$ rows transpose to the last $N/2$ rows ($k \rightarrow k + (N/2)$, $k = 1, \cdots, N/2$) according to a definite parity rule. Elements of matrix V, $v_{zk}\phi_{2\ell}(v_{\rho k})\phi_m(v_{zk})$, transpose with parity opposite to $\phi_m(v_{zk})$. Elements of matrix A, $\phi_{2\ell}(v_{rk})\phi'_m(v_{zk})$, transpose, like elements of V, with parity opposite to $\phi_m(v_{zk})$. Elements of matrix C, $C_d[\phi_{2\ell}(v_{\rho k})\phi_m(v_{zk})]$, depend only on velocity magnitude and thus always transpose with even parity.[26] Lastly, the boundary vector on the right side of (3.24), $v_{zk}f_o(\boldsymbol{v}_k)$, is also two-fold symmetric and transposes with odd parity.

Once these symmetries are taken into account and all the spectral matrices, including the boundary vector, are evaluated, the next step is to perform Gaussian elimination on the FD-spectral equations. Fortunately, the equations have a structure identical to that of the preceding (x, v_x) problem.[27] And so, the method outlined in Section 3.1.3.3, forward elimination and back substitution of a block tridiagonal system, can be followed.

3.2.3.4 Numerical Errors

Error analysis is virtually the same as that for the (x, v_x) problem, and is fully discussed in Section 3.1.3.4. A few remarks are nevertheless in order.

[26] Additional advantage can be taken from the fact that the integrands of Eq. (3.31) have the same parity as ϕ_m. Consequently, when ϕ_m has even parity, $C_d[\bar{\Phi}_{n(\ell,m)}(\boldsymbol{v}_k)] = 0$; and when ϕ_m has odd parity, summations in (3.32) need only be performed over half the original sample variable domain and then doubled.

[27] Additional similarities emerge if (x, v_x) and (z, v_ρ, v_z) problems are compared in terms of the global index n as opposed to the local indices ℓ and m.

As noted in Section 3.1.3.4, round-off and discretization errors can be monitored by performing various tests: back substitution of the solution vector $(\alpha_2, \cdots, \alpha_{L-1})^T$ into (3.14) and calculating the vector error, or changing the parameters Δz and N (that is, N_ℓ or N_m, or both), and observing the roll-off in the transform domain. Round-off error in actual calculations was comparable to that obtained in the (x, v_x) problem because the same number of mathematical operations were involved.[28] Surprisingly, actual calculations confirmed that the velocity discretization error was comparable to that obtained in the (x, v_x) problem even though significantly fewer basis modes per dimension were used. This reflects a combination of factors: the superior effectiveness of Hermite-Gaussian functions in resolving typical carrier distributions and the relative unimportance of high-order (2ℓ and m large) basis functions in the expansion (3.17).

3.2.4 Results and Discussion

3.2.4.1 Execution Rate

Numerical computations were performed on an HP-1000F minicomputer. Enhancement features such as EMA and VIS were used whenever possible. For a thirty-element ($N = 30, N_\ell = 3$, and $N_m = 10$) Hermite-Gaussian basis set and an eighty-point space discretization line ($L = 80$), typical calculation times were on the order of ten seconds for spectral matrix evaluation and one minute for Gaussian elimination.[29]

3.2.4.2 Solution Verification

FD-spectral solutions were verified by means of the standard, previously established, testing scheme—ballistic tests, tests with collisions, and then qualitative tests based on physical reasoning.

Under ballistic conditions and for fixed v_ρ, the (z, v_z) dependence of solutions to the (z, v_ρ, v_z) problem is identical to the (x, v_x) dependence of solu-

[28]Here, the parameters L and N are assumed close, if not equal, for both (x, v_x) and (z, v_ρ, v_z) problems.

[29]The reader is directed to Section 3.1.4.1 for review and should note that much of the its discussion pertains equally well to the (z, v_ρ, v_z) problem except for a few obvious minor modifications (for example, E_{xi} becomes E_{zi}).

tions to the ballistic (x, v_x) problem.[30] Verification of ballistic solutions was therefore performed through direct comparison with solutions to the already verified (x, v_x) problem. Both problems incorporated a Hermite-Gaussian basis set and relevant computational parameters were placed at limits governed by the (z, v_ρ, v_z) problem: $L = 80$, $N = N_m = 10$. Agreement between solutions was monitored for a variety of electric-field distributions. All solutions to (x, v_x) and (z, v_ρ, v_z) problems concurred to within one part in one million, the HP-1000F's maximum (single precision) numerical resolution.

Verification of the full—collision term included—(z, v_ρ, v_z) problem was carried through after ballistic tests were passed. Proper computer coding of acoustic and optic scattering-probability-rate functions was checked using the self-consistent integration technique described in Section 3.1.4.2. Since no closed-form or independently calculated numerical solutions to this problem are available, confirmation of the solution validity was left to the final verification test.

Boundary regions were checked for correct behavior: $f \to 0$ as $v \to \infty$ at the exit $z = L_z$, and $f = f_o$ at the entrance $z = 0$. Spatial invariance of the z component of current density (see Appendix I) was also checked. Current density variation was minimal and inversely correlated with basis set number. Observations relating to the overall shape of the carrier distribution, as mediated by each scattering mechanism, were consistent with physical reasoning. Acoustic phonon scattering tends to couple equi-energy states and thus, under certain conditions, a circularly symmetric ridge in the carrier velocity distribution was observed (see Section 3.2.4.3) On the other hand, optic phonon scattering tends to mix states with different energy so that no circularly symmetric structure was observed; instead, general heating or spreading of the carrier velocity distribution was observed (see Section 3.2.4.3). All in all, the FD-spectral solutions corroborated physical intuition, not only for the cases just discussed, but in many other respects, some of which have been already discussed in connection with the (x, v_x) problem (see Section 3.1.4.2).

[30] If $Cf = 0$ the independent variable v_ρ in (3.15) is merely a parameter; otherwise (3.15) has the same form as (3.1). Note, also, that comparison between these equations implies the correspondences $x \sim z, v_x \sim v_z$, and $E_x \sim E_z$.

Quantity	*Value*	*Units*
Carrier effective mass, m^*	2.99×10^{-31}	kilograms
Crystal density, ρ	2.33×10^{3}	kilograms/meters^3
Speed of sound, u	6.33×10^{3}	meters/second
Deformation-potential acoustic phonon interaction constant, Ξ_a	1.44×10^{-18}	joules
Optic phonon frequency, ω_o	8.38×10^{13}	seconds^{-1}
Nonpolar optic phonon interaction constant, Ξ_o	1.60×10^{-8}	joules/meter

Table 3.2: Physical parameters for equivalent spherical, parabolic X valley of silicon, with deformation-potential acoustic and nonpolar optic scattering.

Quantity	*Value*	*Units*
Number of ϕ_ℓ constituent functions, N_ℓ	3	—
Number of ϕ_m constituent functions, N_m	10	—
Number of z points, L	80	—
Cell size, Δz	1.25×10^{-8}	meters
Average roundoff error in $\lvert\alpha_i\rvert$	$\sim 10^{-3}$	—

Table 3.3: Computational parameters for the (z, v_ρ, v_z) problem.

3.2.4.3 Numerical Solutions

In this final section, results of two representative FD-spectral calculations will be presented and commented upon.

Tables 3.2 and 3.3 list the physical and computational parameters which were employed in the calculations. Based on data from the literature, physical parameters have been adjusted to agree as closely as possible with those for the silicon semiconductor system [8,9]. Electric field and potential distributions are plotted in Fig. 3.6. The piecewise-linear electric field and corresponding cusped, piecewise-quadratic potential distribution resembles those used in Sections 2.2.4.3 and 3.1.4.3.

In the following plotted results only acoustic phonon scattering has been included. This way, the weaker, more unusual effects of acoustic scattering will be revealed and at the same time much of the basic transport physics can still be covered.

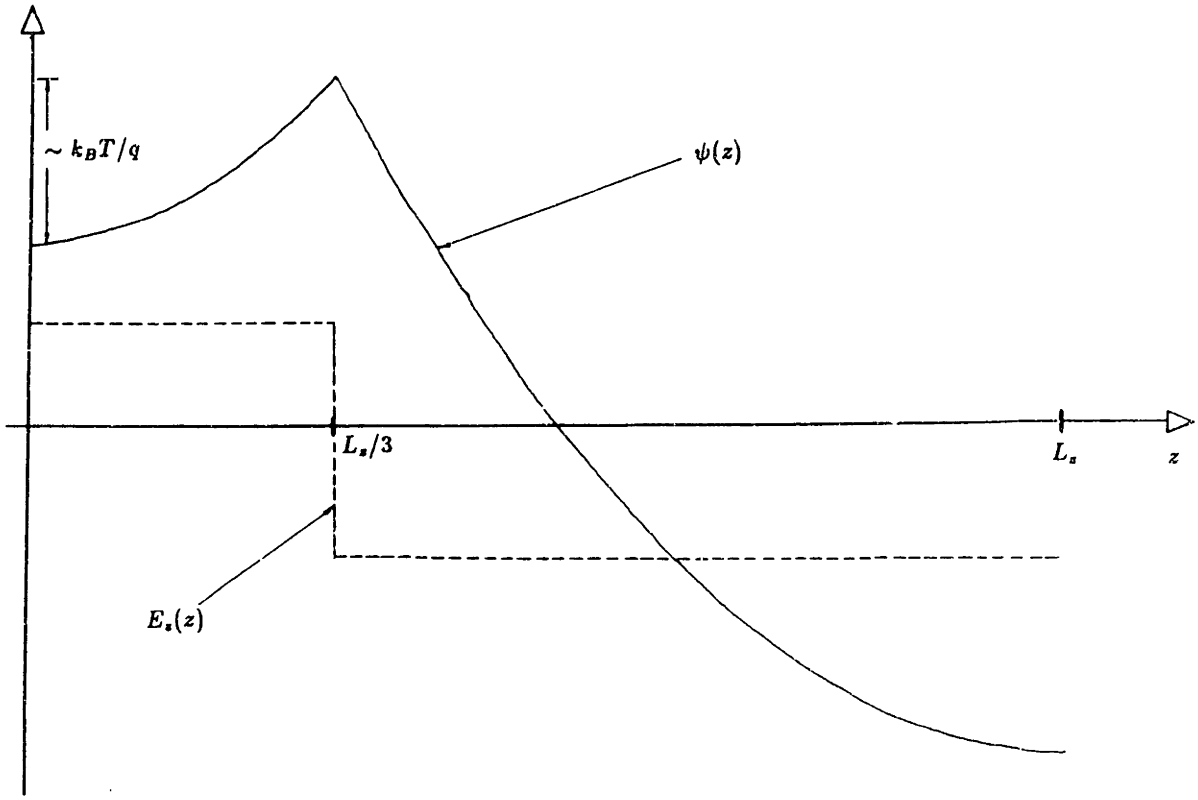

Figure 3.6. Potential and electric field versus z.

Carrier distributions have been plotted with spatial position z as a parameter. Figure 3.7 portrays the variation of the distribution function with velocity component parallel to the electric field, v_z, for a fixed normal velocity component $v_\rho = 0$. Figure 3.8 portrays the inverse case, in which v_ρ and v_z are interchanged.[31] It is evident that large velocity boundary conditions, $f \to 0$ as $v_\rho \to \infty$ and $v_z \to \pm\infty$, are satisfied. Boundary conditions associated with spatial regions are also satisfied: $f = f_o$ for $z = 0$ and $v_z > 0$; $f = 0$ for $z = L_z$ and $v_z < 0$. Moreover, as has been seen in previous calculations, the carrier distribution can be characterized in three distinct spatial regions. In the entrance region, $z \approx 0$, near-equilibrium conditions prevail and the distribution function closely resembles the symmetric Maxwellian distribution. The transition region, near the potential cusp, $z \approx L_z/3$, is typified by a rapidly varying distribution function in all three independent variables (z, v_ρ, v_z). Here, the distribution function departs from a symmetric Maxwellian shape. By the time carriers have progressed to the exit region, $z \approx L_z$, the distribution function is strongly out of equilibrium as confirmed by its highly asymmetric v_z dependence. Notice Fig. 3.8 implies that in this latter region the distribution function becomes smaller toward the exit, eventually vanishing completely at $z = L_z$ and $v_z = 0$ for all v_ρ. This is consistent with the fact that the distribution function is zero at the point $z = L_z, v_\rho = v_z = 0$ in both Figs. 3.7 and 3.8.[32]

Asymmetries in the carrier distributions shown in Fig. 3.7 are caused by the diffusion gradient along the z direction, the accelerating action of the z-directed electric field, and the symmetrizing influence of acoustic scattering. The overall spatial behavior of these asymmetrical velocity distributions can be intuitively understood using a current conservation argument. Since the z component of current density, that is, the carrier distribution's first moment,

[31]Note that, for reasons of aesthetics, the domain $0 < v_\rho < \infty$ has been extended to $-\infty < v_\rho < \infty$ where $f(z, v_\rho, v_z) = f(z, -v_\rho, v_z)$.

[32]Closer examination of Figs. 3.7 and 3.8 in the exit region shows that the distribution function actually becomes slightly negative. This has a small effect on calculated distribution moments, and is a consequence of velocity discretisation error in approximating the piecewise-smooth solution at $z = L_z$. The three-dimensional distribution plots which will be presented later will clarify the nature of this error. The error is usually manifested as an oscillation (with period on the order of the inter-collocation spacing) which in ordinary Fourier analysis is known as a Gibbs oscillation [25]. Hereafter, this phenomenon will be designated as "Gibbs ringing" despite the fact that it originates from a Hermite-Gaussian set.

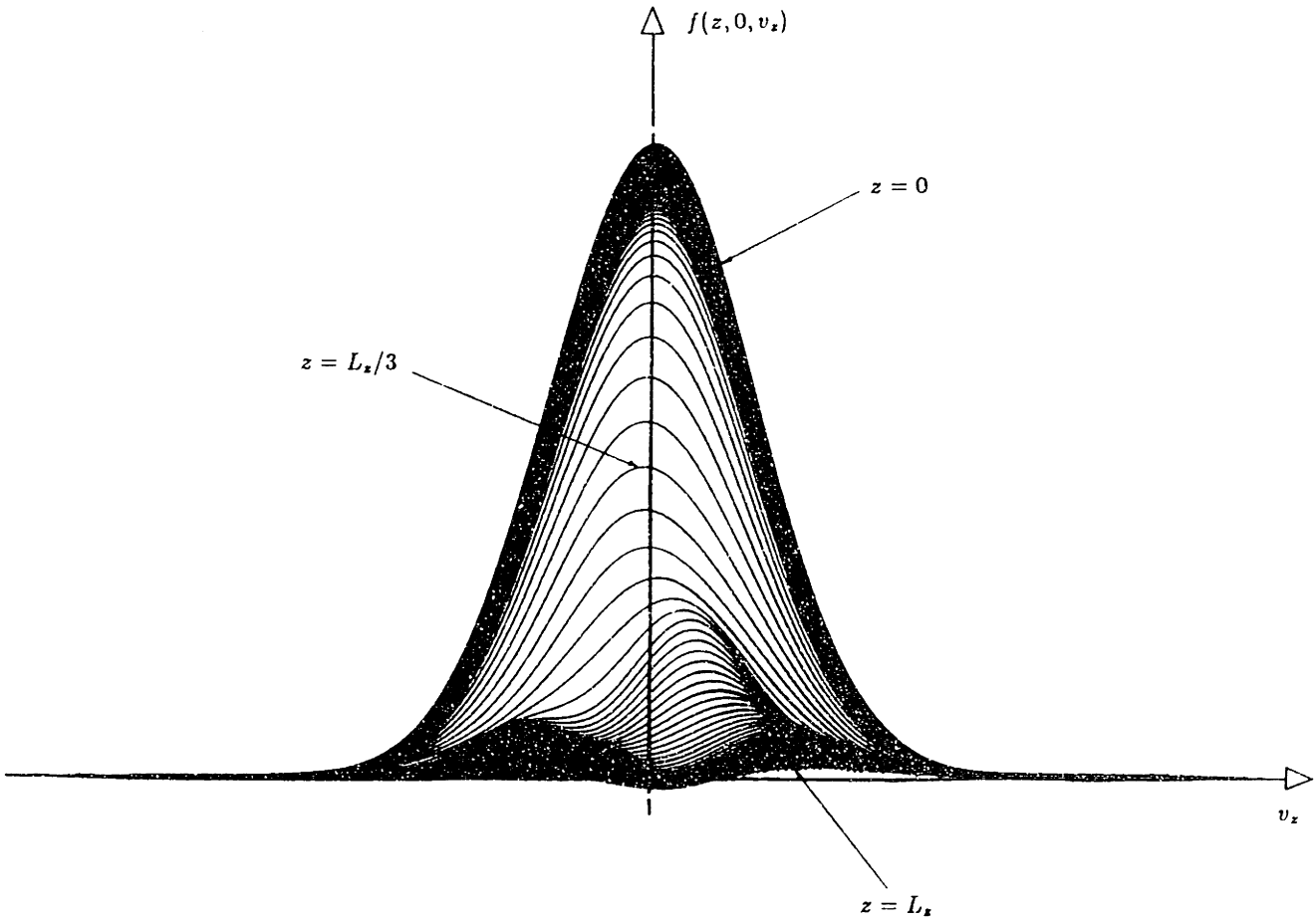

Figure 3.7. Carrier distribution versus v_z for $v_\rho = 0$, parameterized from $z = 0$ to $z = L_z$.

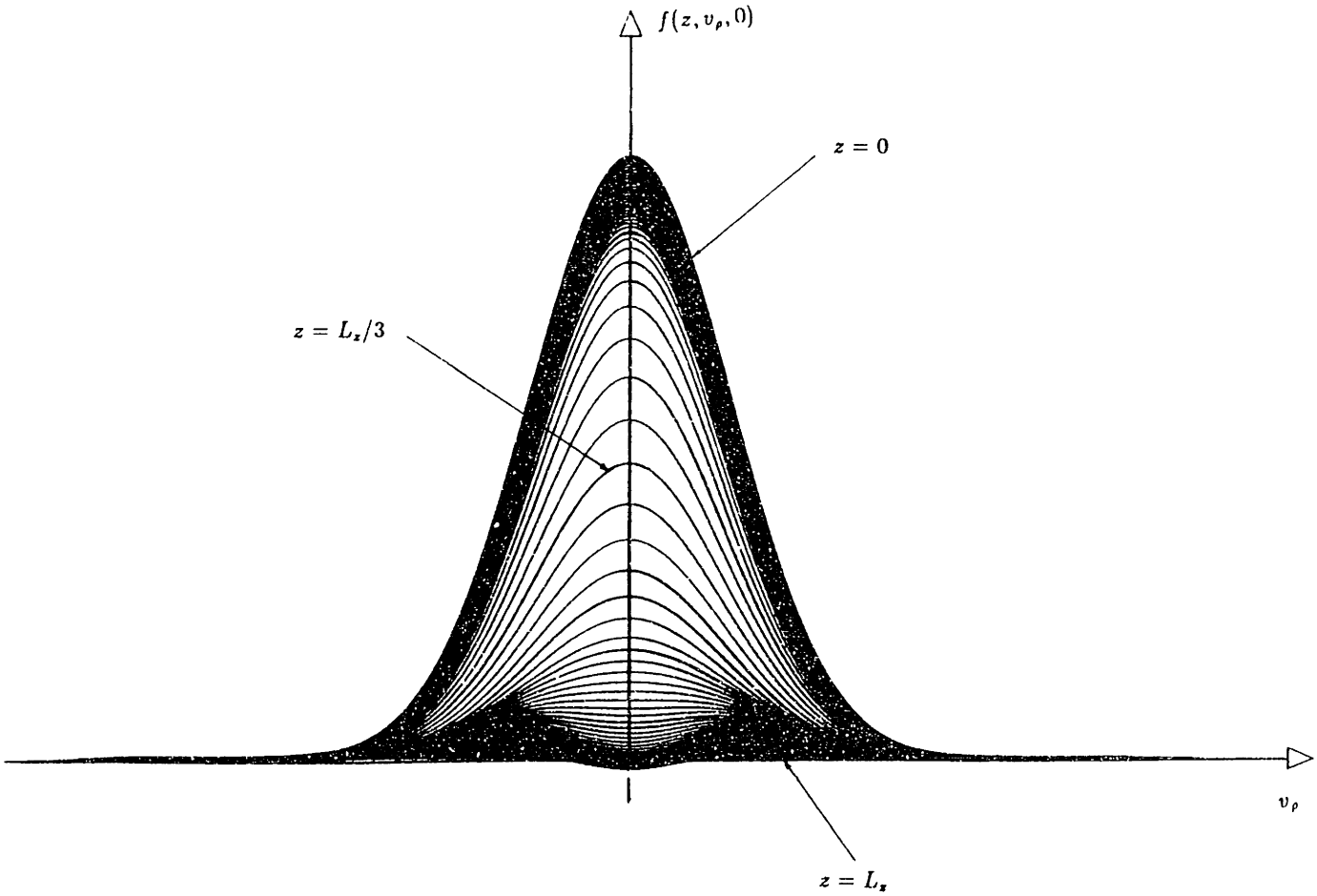

Figure 3.8. Carrier distribution versus v_ρ for $v_z = 0$, parameterized from $z = 0$ to $z = L_z$.

is conserved, an inverse relation between average velocity and concentration is expected to exist. The curves of Fig. 3.7 illustrate this relationship. It is worth noting that the carrier distributions of Figs. 3.7 and 3.8 are in a sense "coupled" by the collision processes. Coupling is evidenced in Fig. 3.8 where significant heating perpendicular to the electric field is seen to occur. This happens because of scattering from electric-field-accelerated states with large v_z to ones with large v_ρ.

A better visualization of the carrier velocity distribution can be attained with the aid of Figs. 3.9 and 3.10. Figure 3.9 depicts the carrier distribution in the entrance region as a function of v_ρ and v_z. The distribution function resembles a bell-shaped equilibrium Maxwellian, in accordance with previous remarks. The shape of the distribution function is primarily determined by the injective boundary condition at $z = 0$ and subsequent drift and diffusion of carriers up and then down the potential cusp's left side (refer to the Fig. 3.9 inset). On account of the near spherical symmetry of the distribution function, acoustic scattering effects roughly cancel and are of minor importance.[33] Now, in the exit region the distribution function is heavily out of equilibrium. Figure 3.10 shows that the carrier distribution has a peculiar "crater-like" structure. Inside the crater undulations exist due to Gibbs ringing. The circular form of the crater rim is a direct consequence of the the equi-energy coupling of acoustic scattering. Notice, too, that the crater-like distribution is somewhat slanted. This behavior is explained by the fact that the left half ($v_z < 0$) of the distribution must smoothly and systematically vanish approaching the exit $z = L_z$, in accordance with boundary conditions.[34]

It is informative to examine the two-dimensional Hermite-Gaussian transform of the distribution function. A simpler one-dimensional transform has been an earlier topic in Section 3.1.4.3; in this case generalization is straightforward. The transform of the carrier velocity distribution is displayed for

[33]The term "spherical symmetry" means that the velocity distribution has a dependence $f(z, v) \approx f(z, \epsilon)$. Also note that spherical symmetry is not in general sufficient to ensure cancellation of effects arising from an arbitrary scattering mechanism. What is sufficient to ensure cancellation, however, is that near-equilibrium conditions prevail, for which $f \approx f_o$ and then $Cf \approx Cf_o = 0$.

[34]To think that the slanting is primarily a result of the positive electric field in the exit region is misleading. For instance, the large positive field just beyond the potential cusp (towards the exit) strongly perturbs the carrier distribution well before the exit, but no asymmetric slanting is apparent there.

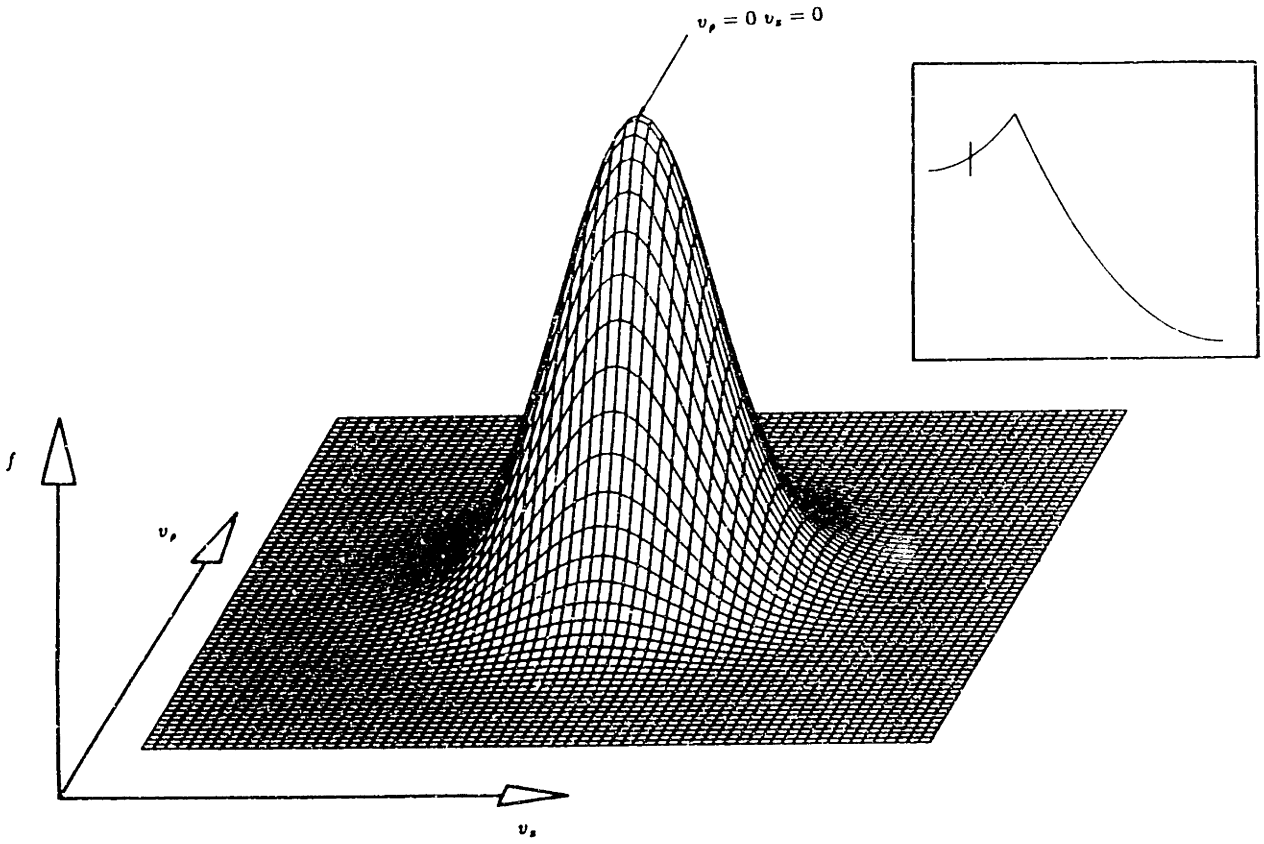

Figure 3.9. Three-dimensional plot of the carrier distribution versus (v_ρ, v_z) in the entrance region.

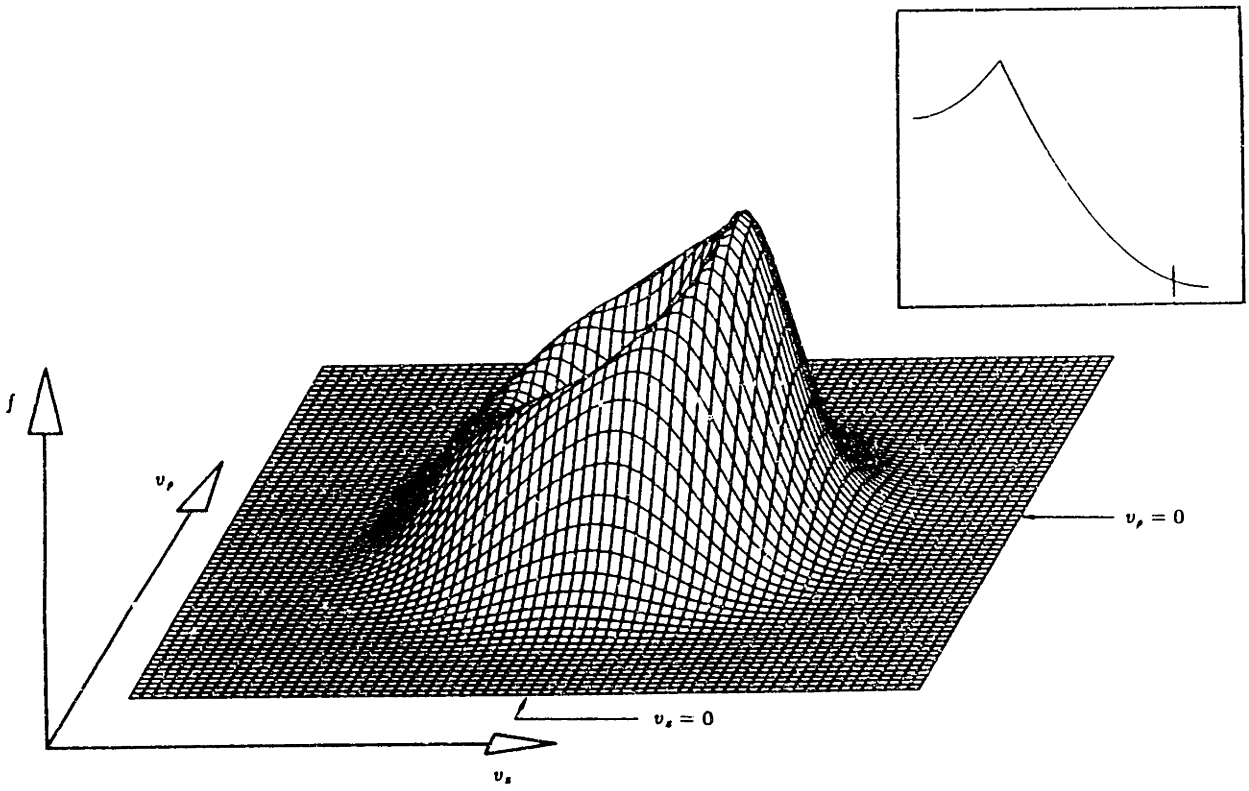

Figure 3.10. Three-dimensional plot of the carrier distribution versus (v_ρ, v_z) in the exit region.

entrance and exit region in Figs. 3.11 and 3.12, respectively. Expansion coefficient vectors are represented with solid bars and arranged according to increasing local indices ℓ and m. In Fig. 3.11 quasi-equilibrium conditions prevail and the Maxwellian character of the distribution function is confirmed by the large Gaussian function coefficient α_{11}. The other coefficients $\alpha_{\ell m}$ $(\ell \neq 1, m \neq 1)$ are extremely small. Their nonzero values are not related to numerical errors, however, but signify small, real deviations from an exact Maxwellian distribution.[35] The transform plot of Fig. 3.12 illustrates the nonequilibrium situation in the exit region. In order to approximate the carrier distribution, contributions from basis functions with higher-order constituents ($\phi_{2\ell}$ and ϕ_m) are required. As a final comment, both Figs. 3.11 and 3.12 show a gradual decay, or roll-off, in expansion coefficient magnitude with increasing local index ℓ or m. This behavior, which relates to issues of accuracy and resolution, has been observed in the (x, v_x) problem and is typical of convergent spectral approximations.

In a device simulation context it is often necessary to evaluate various macroscopic physical quantities. These quantities depend on integrals, or more precisely, velocity moments of the distribution function. A few relevant quantities are plotted against space coordinate in Fig. 3.13. The plots are generated from the distribution function obtained in the foregoing example calculation. Displayed are the carrier concentration $n(z)$, the z component of current density $J_z(z)$, and the average z component of velocity $\bar{v}_z(z)$. And, included for reference is the electric potential $\psi(z)$. Carrier concentration and current density are just the zeroth and first moments, respectively, of the distribution function, while average velocity is determined through the simple relation $\bar{v}_z = J_z/qn$. Moments of the distribution function were evaluated numerically by means of the efficient method described in Appendix I. Overall, concentration is seen to decrease monotonically with a concomitant monotonic increase in average velocity. This behavior follows from the fact that current density is roughly constant, to within ten percent of average, throughout the device structure.

Upon closer inspection, minor peculiarities which appear as step discontinuities can be seen in Fig. 3.13. The discontinuities are coincident with the potential cusp and occur because of the step discontinuity in electric field

[35]Of course, deviations must exist or there would be no net current and no measurable heating of the carrier distribution.

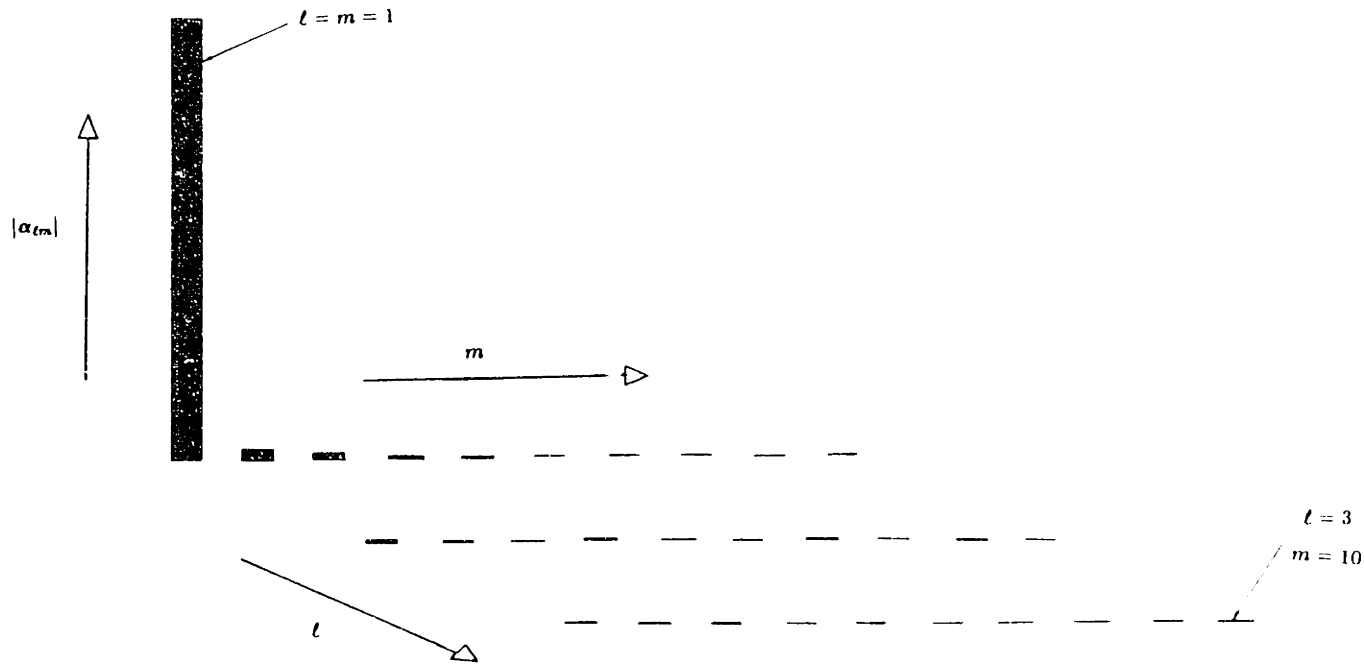

Figure 3.11. Hermite-Gaussian transform of the carrier distribution in the entrance region.

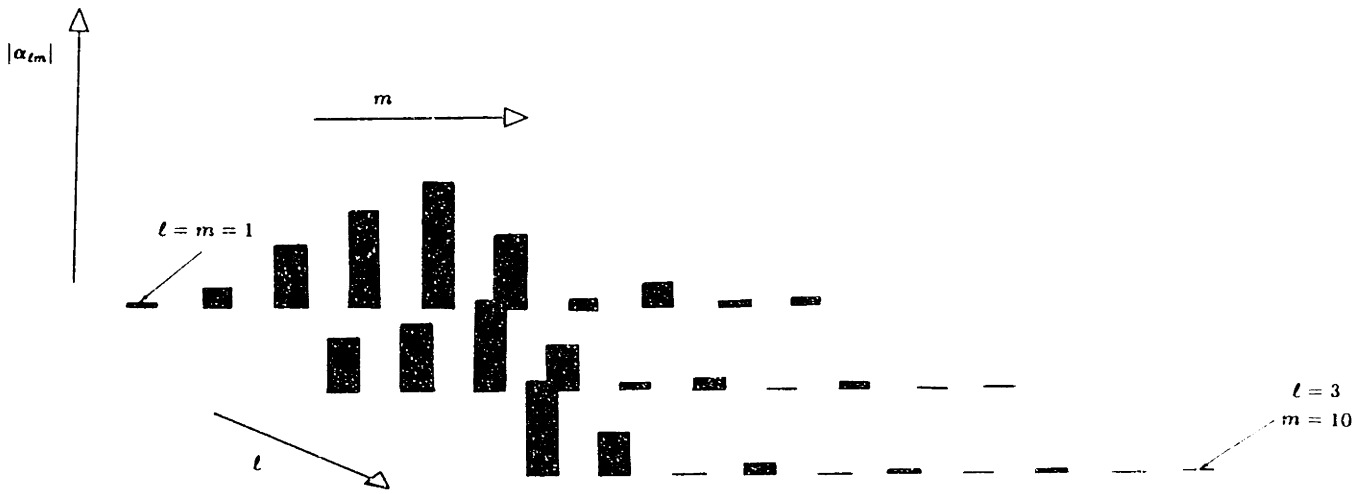

Figure 3.12. Hermite-Gaussian transform of the carrier distribution in the exit region.

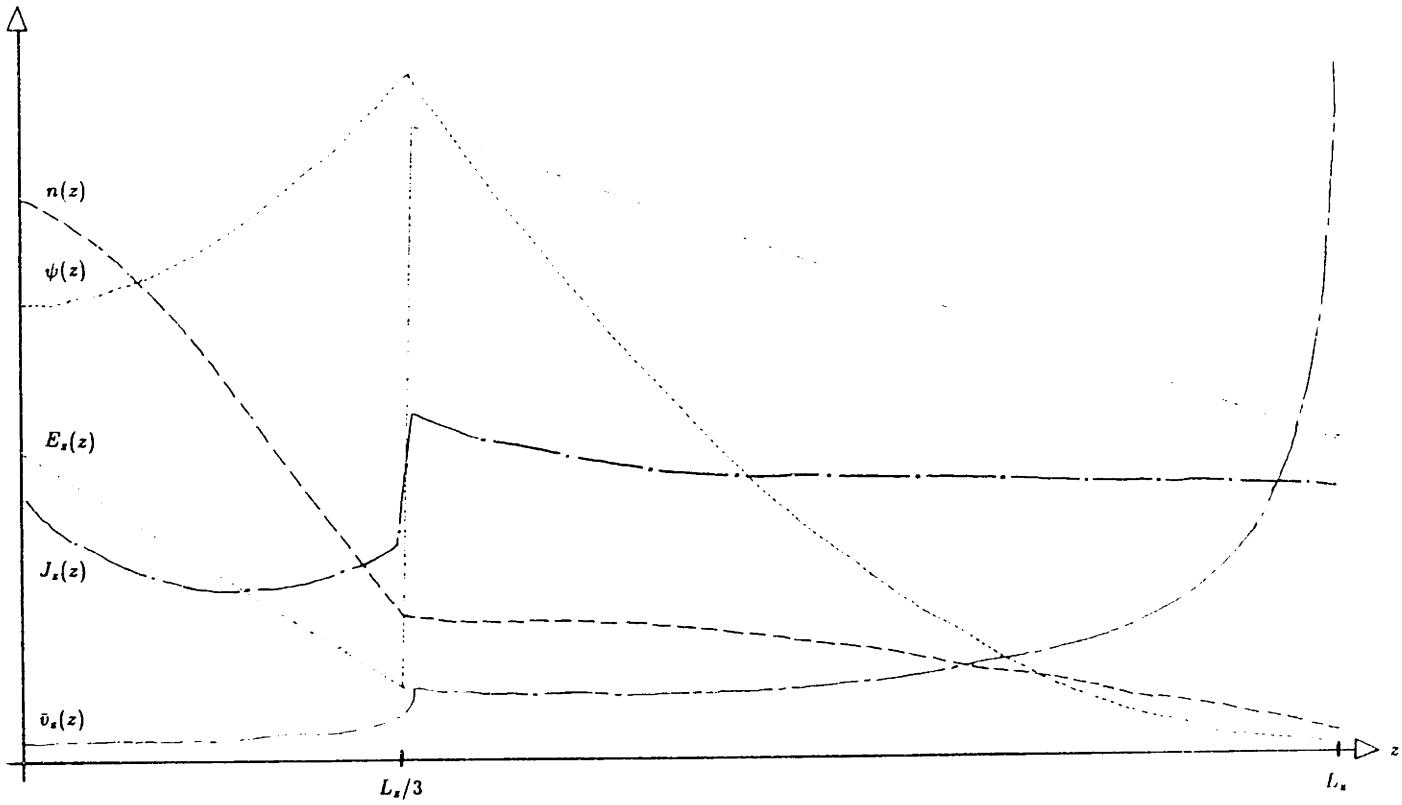

Figure 3.13. Carrier concentration, mean z component of velocity, and current density versus z (potential and electric field included for reference).

there.[36] In addition, there is an apparent increase and decrease in current density about the potential cusp. Most of the variation in current density is accounted for near the cusp itself. Such variation is believed to be caused by the difficulty in resolving the rapidly changing distribution function when the electric field reverses direction.[37]

Fundamentally, exact constancy of current density for low-order FD-spectral approximations (N small) is never realized because the zeroth moment of BTE (3.15), the current continuity equation, is approximated by what amounts to be a quadrature integration with samples located at the N collocation points.[38] From the remarks at the end of Section 3.1.4.3, the variation in current density associated with this nonconservative solution method is not necessarily unfortunate—in fact, it can be used to advantage. First of all, at the expense of additional computation, current density can be kept within arbitrary bounds if a sufficient number of basis functions are included in the basis set. Once current density has been constrained to acceptable limits, it can be statistically averaged over the space discretization points z_i, $i = 1, \cdots, L$. The statistical mean of the $J_z(z_i)$ therefore represents the "best" numerical approximation to the true current density, while the corresponding statistical variance not only indicates the relative error in current density but also the total absolute numerical error (round off and discretization) in the distribution function $f_i(\boldsymbol{v})$ itself.

Up to now optic phonon scattering has not been included in the calculations. For the sake of completeness, a quick overview covering the salient properties of carrier distributions under the dominant influence of optic

[36]Discontinuities have been completely eliminated by using a smoother electric-field distribution. Interestingly enough, it has been found that at the potential barrier peak any discontinuity in the electric field or its derivatives $[E_z'(z), E_z''(z), \cdots]$ is directly reflected with a corresponding discontinuity or derivative discontinuity in carrier distribution moments.

[37]Not only field reversals of sudden, discontinuous nature are referred to here, but also those which occur in a smooth and gradual fashion, albeit over a relatively narrow spatial region.

[38]If necessary, a conservative FD-spectral scheme can be formulated. Spectral matrices would be determined through evaluation of of N successive moments of the velocity residual: $\int d^3v\ R(\boldsymbol{v}) v_\rho^{p-1} v_z^{q-1}$, $p = 1, \cdots, N_\ell$, and $q = 1, \cdots, N_m$. This integral method suffers, however, from an increased computational burden in performing moment integrations and a loss of symmetry in the resulting spectral matrices. (For example, calculation of the collision matrix would entail the arduous task of numerically integrating over four or more dimensions.) These disadvantages can be disastrous when attempting to solve high-dimensionality problems.

phonon scattering will be given. Calculations have carried out in which acoustic and optic scattering have been both included. Scattering parameters, acoustic and optic, are listed in Table 3.2. In large part the strong influence of optic phonon scattering resulted in bell-shaped, Gaussian-like carrier distributions. In the entrance region the carrier distribution closely resembled the equilibrium Maxwellian. Towards the transition and exit regions the carrier distribution has been found to become progressively broader because of carrier heating, yet still Gaussian-like in shape.[39] Unlike the the previous calculations (including only acoustic phonon scattering), no unusual crater-like distributions were observed. The three-dimensional plot of Fig. 3.14 is a good example of the relatively featureless carrier distribution in an optic phonon dominated system. This plot shows the velocity distribution in the exit region and exactly corresponds to the situation depicted in Fig. 3.10 for the optic-phonon-free case. It is apparent that that the optic phonon scattering process has a "crater-filling" effect that comes about from a large amount of inelastic "energy mixing" during collisions. Energy mixing tends to smooth out any features in the distribution function that vary rapidly in velocity.[40] Observe also that a certain amount of Gibbs ringing is evident. Similar to what was seen in the acoustic scattering case, Gibbs ringing arises from the difficulty in satisfying the exit boundary condition $f = 0$ for $z = L_z$ and $v_z < 0$ between collocation points. Finally, it should be mentioned that additional properties of the carrier distribution in this model silicon system can be inferred from the next chapter's closely related problem.

[39]This behavior is typical in silicon systems and has been independently observed by other investigators [26].

[40]Indirectly, by means of diffusion (or more precisely, convection), features which vary rapidly in space are smoothed as well.

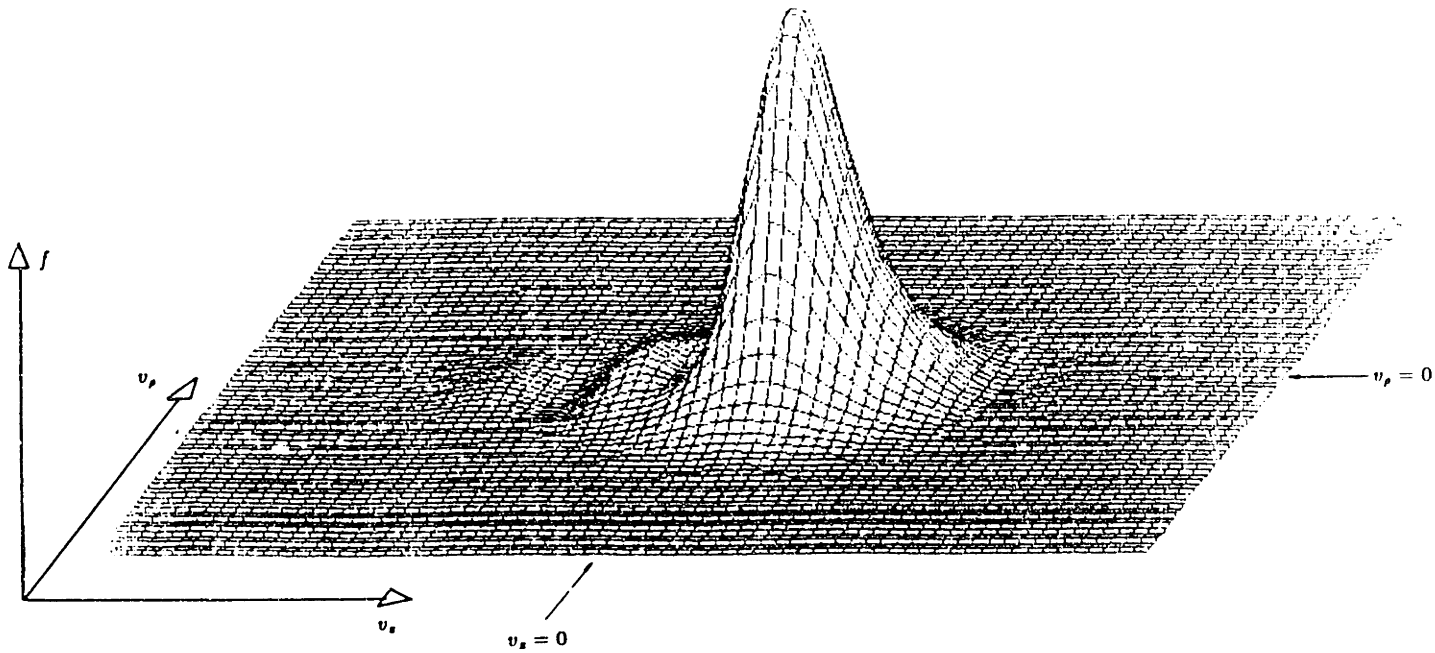

Figure 3.14. Three-dimensional plot of the carrier distribution versus (v_ρ, v_z) in the entrance region with optic scattering included.

Chapter 4

Spectral Solution of the High-Dimensionality BTE

In the previous chapter the FD-spectral method was applied to systems with relatively few independent variables. As a consequence, the resulting FD-spectral equations could be solved directly, by means of Gaussian elimination. But many semiconductor devices of current interest do not fall into the category of low-dimensionality systems; to the contrary, they are inherently high-dimensionality systems, with at least four independent variables.[1] FD-spectral equations for high-dimensionality systems are efficiently solved using iterative techniques. Direct solution techniques, such as Gaussian elimination, quickly become inefficient on account of the large FD-spectral equation coefficient matrix and the concomitant loss of tridiagonal symmetry.[2]

This chapter is solely concerned with solution of the steady-state (time-independent) BTE. The iterative pseudo-transient methods first introduced in Chapter 2 will be extended to solve FD-spectral equations. A five-dimensional (x, y, v_x, v_y, v_z) problem, which includes both acoustic and optic phonon scattering, will be treated. The (x, y, v_x, v_y, v_z) problem will be set up to describe transport in a device structure periodic and mirror-symmetric in x and should be a good basic model of the silicon permeable-base transistor

[1] The maximum number of independent variables is seven (per band): in Cartesian coordinates, three space (x, y, z), three velocity (v_x, v_y, v_z), and time t.

[2] The coefficient matrix associated with FD-spectral solution of high-dimensionality systems is generally block banded. Refer to Section 4.2.3 for an example.

[4], a device that is presently under active research and development. Therefore, this chapter's results provide a true test of the FD-spectral method when it comes to simulation of real, two-dimensional semiconductor devices.

4.1 The (x, y, v_x, v_y, v_z) Problem

In contrast to Chapter 3's (z, v_ρ, v_z) problem, variation is now permitted throughout a two-dimensional spatial plane. Velocity variation is intertwined with spatial variation and thus any physically realistic system with two space variables must also possess three velocity variables. The distribution function for this system is $f = f(x, y, v_x, v_y, v_z)$ in Cartesian coordinates. Two-dimensional spatial variation further implies that the velocity dependence of the carrier distribution is mirror symmetric about the (v_x, v_y) plane: $f(\cdots, v_z) = f(\cdots, -v_z)$[3]; hence, for calculation purposes the phase-space domain will be restricted to $v_z > 0$. In line with the assumed distribution function dependencies, the electric field can vary with x and y only; vectorially, $\boldsymbol{E} = E_x(\boldsymbol{r})\hat{\boldsymbol{e}}_x + E_y(\boldsymbol{r})\hat{\boldsymbol{e}}_y$ where $\boldsymbol{r} = x\hat{\boldsymbol{e}}_x + y\hat{\boldsymbol{e}}_y$. The continuous version of the BTE can be expressed

$$\frac{\partial f}{\partial \tau} = -\boldsymbol{v} \cdot \nabla_r f - \frac{q}{m^*}\boldsymbol{E} \cdot \nabla_v f + Cf. \tag{4.1}$$

Here, $\boldsymbol{v} = v_x\hat{\boldsymbol{e}}_x + v_y\hat{\boldsymbol{e}}_y + v_z\hat{\boldsymbol{e}}_z$ is the vector velocity variable and C is the usual collision operator. More precisely, Eq. (4.1) is simply the steady-state BTE, modified for pseudo-transient evolution. The parameter τ, pseudo time, can be envisioned mathematically as a time variable for a time-dependent distribution $f = f(\boldsymbol{r}, \boldsymbol{v}; \tau)$. Nevertheless, τ has no physical significance in representing actual time; its introduction merely facilitates iterative numerical solution of the steady-state, time-independent BTE—that is, (4.1) with

[3]Symmetries in the distribution function can be clearly understood by considering individual carrier trajectories. (The following argument applies to time-dependent systems as well.) Drift and diffusive effects only alter the v_x and v_y components of carrier velocity. The influence of collisions is to alter not only the v_x and v_y components of carrier velocity but also the v_z component. Thus, all three velocity variables are coupled through the BTE's integral collision term. Actual scattering processes change a carrier's z-directed velocity by amounts that have an equal likelihood of being positive or negative. Any ensemble of carriers therefore possesses a mirror symmetric velocity distribution about the (v_x, v_y) plane, at all points in space. (The discussion of Appendix H may be helpful in better understanding the relationship between carrier trajectories and the distribution function.)

$\partial f/\partial\tau = 0$. [See Sections 2.1.3.3 and 2.2.3.3 for a discussion of the pseudo-transient method in the context of the (v_ρ, v_z, t) and (x, v_z, t) problems.]

4.2 The FD-Spectral Method

4.2.1 Velocity Discretization

Application of the FD-spectral method to BTE (4.1) requires spectral decomposition of the distribution's velocity dependence:

$$f(\boldsymbol{r}, \boldsymbol{v}; \tau) \approx \sum_{n=1}^{N} \alpha_n(\boldsymbol{r}; \tau)\Phi_n(\boldsymbol{v}), \tag{4.2}$$

in which elements of the velocity basis set and space- and pseudo-time-dependent expansion coefficients are denoted Φ_n and α_n, respectively. Upon generalization of the arguments presented in Section 3.2.1.1, the basis functions can be expressed in terms of monodimensional products; therefore,

$$f(\boldsymbol{r}, \boldsymbol{v}; \tau) \approx \sum_{\kappa=1}^{N_\kappa} \sum_{\ell=1}^{N_\ell} \sum_{m=1}^{N_m} \alpha_{\kappa\ell m}(\boldsymbol{r}; \tau)\phi_\kappa(v_x)\phi_\ell(v_y)\phi_{2m}(v_z). \tag{4.3}$$

The the above triple-series expansion is a three-dimensional generalization of (3.17). Constituent functions ϕ_κ, ϕ_ℓ, and ϕ_{2m} derive, respectively, from the first N_κ (even and odd), N_ℓ (even and odd), and N_m (even) elements of a monodimensional basis set; even v_z-dependent constituent functions are included, in accordance with comments made in the previous section. An assortment of transformation functions link the global index n of (4.2) with the local indices κ, ℓ, and m of (4.3). In complete analogy with what was done for the low-dimensionality problem in Section 3.2, a relationship exists between the expansion coefficients: $\alpha_n = \alpha_{\kappa(n)\ell(n)m(n)}$ and $\alpha_{\kappa\ell m} = \alpha_{n(\kappa,\ell,m)}$. Upper limits on global and local indices are connected through $N = N_\kappa N_\ell N_m$. Notice, also, that the basis functions Φ_n are mathematically complete because the constituent functions belong to a mathematically complete set themselves.

It is evident that the distribution function $f(\boldsymbol{r}, \boldsymbol{v}; \tau)$ and the expansion coefficients $\alpha_n(\boldsymbol{r}; \tau)$ contain equivalent information. Spectral discretization of velocity thereby transforms the distribution function to a pseudo-time-dependent vector field:

$$f(\boldsymbol{r}, \boldsymbol{v}; \tau) \longrightarrow \boldsymbol{\alpha}(\boldsymbol{r}; \tau), \tag{4.4}$$

$$\{\alpha(\mathbf{r};\tau)\}_n = \alpha_n(\mathbf{r};\tau),$$
$$n = 1, \cdots, N.$$

4.2.2 Space and Pseudo-Time Discretization

The remaining variables $\mathbf{r}$ and τ are discretized through the customary finite-difference procedure. Here, solutions to the BTE are sought over a fixed rectangular space mesh, L points in x by M points in y. Hence,

$$\alpha(\mathbf{r};\tau) \longrightarrow \alpha_{ij}(\tau), \tag{4.5}$$

$$x_i = x_o + i\Delta x,$$
$$y_j = y_o + j\Delta y,$$
$$i = 1, \cdots, L,$$
$$j = 1, \cdots, M.$$

Along with discretization of the distribution function's independent space variables the electric field transforms as

$$E(\mathbf{r}) \longrightarrow E_{zij}\hat{\mathbf{e}}_x + E_{yij}\hat{\mathbf{e}}_y. \tag{4.6}$$

As touched upon earlier, pseudo time τ aids in iterative solution of the time-independent BTE. Pseudo time can be treated like a real physical time variable for purposes of numerical algorithm development. Along the semi-infinite pseudo-time axis the expansion coefficients further discretize according to

$$\alpha_{ij}(\tau) \longrightarrow \alpha_{ij}^h, \tag{4.7}$$

$$\tau_h = \tau_o + \sum_{u=1}^{h} \Delta\tau^u,$$
$$h = 0, 1, 2, \cdots.$$

In this case a finite-difference discretization of pseudo time has been performed with a variable sample interval $\Delta\tau^h$.

Evaluation of the discrete distribution function is now possible starting from either expansions (4.2) or (4.3). From (4.2)[4]

$$f_{ij}^h(v) = \sum_{n=1}^{N} \{\alpha_{ij}^h\}_n \Phi_n(v). \tag{4.8}$$

4.2.3 FD-Spectral Equations

To develop a set of FD-spectral equations, substitution of expansion (4.2) into governing equation (4.1) is carried out. This procedure has already been outlined in Section 1.2.3 and is a direct extension of what was done for the (z, v_ρ, v_z) problem. In this instance, the residual $R(\boldsymbol{v}_k)$ is forced to vanish at a set of N collocation points (v_{xk}, v_{yk}, v_{zk}), $k = 1, \cdots, N$, where the $\boldsymbol{v}_k$ are now three dimensional. Collocation points are determined by all possible combinations of extrema from constituent functions $\phi_{N_\kappa}, \phi_{N_\ell}$, and ϕ_{2N_m} (positive extrema only). As is usual practice, N_κ and N_ℓ are taken even to avoid collection points $v_x = 0$ and $v_y = 0$.

The FD-spectral equations are defined over a hybrid finite-difference-collocation mesh. Figure 4.1 illustrates this numerical domain. It consists of a "finite-difference plane" in which each finite-difference point $\boldsymbol{r}_{ij}$ connects to a "collocation cube" comprising the $\boldsymbol{v}_k$. There are basically two types of mesh points: internal and boundary. Boundary points are associated with the collocation cubes that emanate from finite-difference points at spatial boundaries, $i = 1, L$ and $j = 1, M$. The majority of mesh points, however, are designated internal points, which includes all the remaining nonboundary collocation cubes, $i = 2, \cdots, L-1$ and $j = 2, \cdots, M-1$.

At each internal mesh point the FD-spectral equations have the vector-difference structure for a single pseudo-time step shown below:

$$\dot{\boldsymbol{f}}_{ij}^h = -\boldsymbol{V}\boldsymbol{\Delta}_x \boldsymbol{\alpha}_{ij}^h - \boldsymbol{W}\boldsymbol{\Delta}_y \boldsymbol{\alpha}_{ij}^h - \frac{qE_{zij}}{m^*}\boldsymbol{A}\boldsymbol{\alpha}_{ij}^h - \frac{qE_{yij}}{m^*}\boldsymbol{B}\boldsymbol{\alpha}_{ij}^h + \boldsymbol{C}\boldsymbol{\alpha}_{ij}^h \tag{4.9}$$

and

$$\boldsymbol{\alpha}_{ij}^{h+1} = \boldsymbol{\alpha}_{ij}^h + \Delta\tau^h \boldsymbol{T}\dot{\boldsymbol{f}}_{ij}^h, \tag{4.10}$$

[4]It will be seen later that the time-independent distribution function is approximated by $f_{ij}^h(v)$ for $h \to \infty$, the "steady-state" discrete distribution function. Therefore, the discrete distribution function in (4.8) should be thought as being independent of pseudo-time index h in an asymptotic sense.

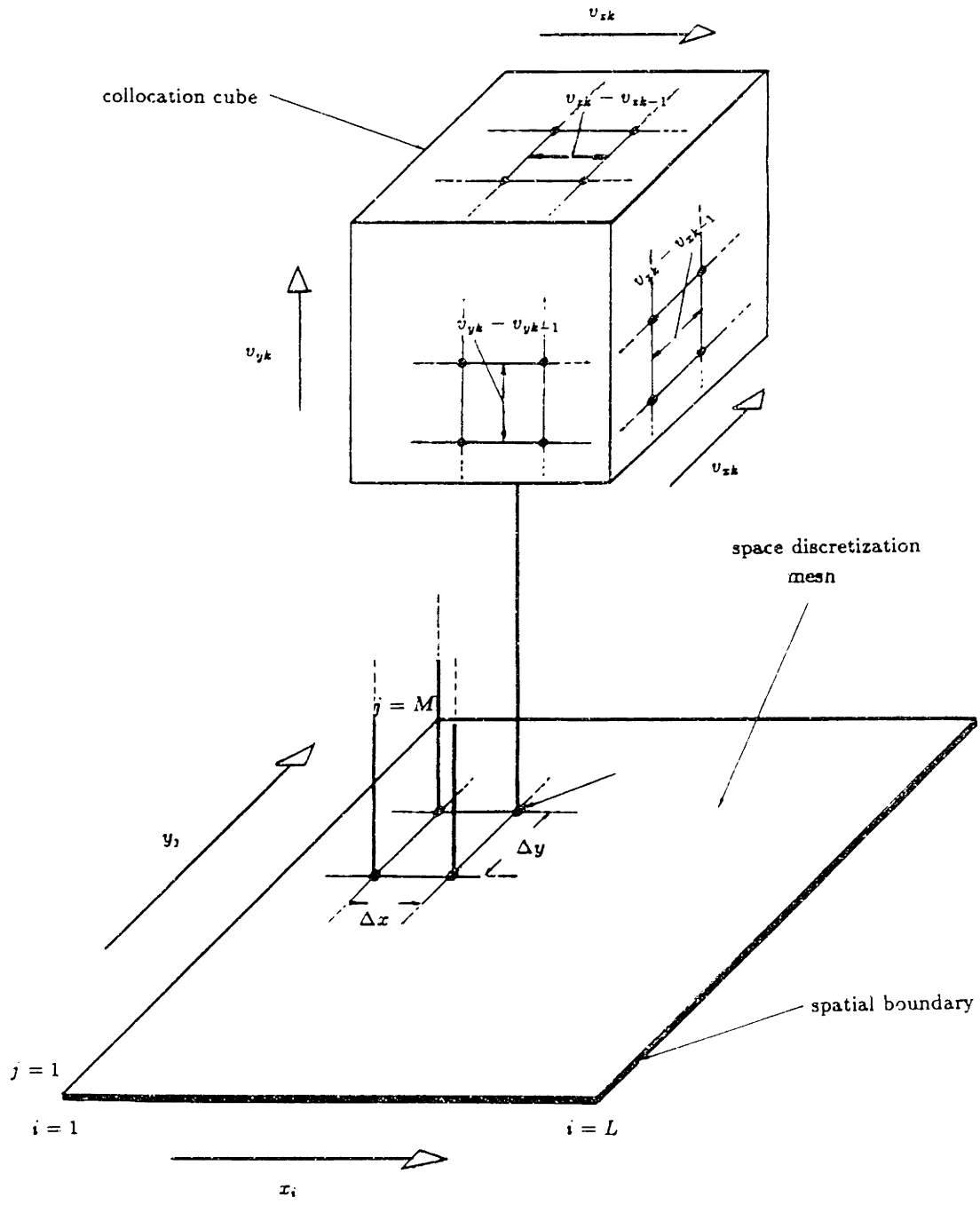

Figure 4.1. FD-spectral discretization mesh for the (x, y, v_x, v_y, v_z) problem.

$$i = 2, \cdots, L-1,$$
$$j = 2, \cdots, M-1.$$

A single pseudo-time step requires two "subcalculations": (4.9) for $\dot{f}_{ij}^{h}$ given α_{ij}^{h}, and then (4.10) for α_{ij}^{h+1}. These vector equations are a generalization of (3.22), and presently incorporate additional space and pseudo-time variables. The vector quantity $\dot{f}_{ij}^{h}$ represents the action of drift, diffusion, and collision terms on the right side of original BTE (4.1). Improved second-order accuracy in spatial finite-difference derivatives is attained through central differencing [15], whereby

$$\Delta_x \alpha_{ij}^{h} \doteq \frac{1}{2\Delta x}(\alpha_{i+1j}^{h} - \alpha_{i-1j}^{h}), \tag{4.11}$$

$$\Delta_y \alpha_{ij}^{h} \doteq \frac{1}{2\Delta y}(\alpha_{ij+1}^{h} - \alpha_{ij-1}^{h}). \tag{4.12}$$

Both of these formulas have a spatial discretization error which is second order in each respective increment variable, Δx or Δy. Written out in full, the spectral matrix elements are

$$\begin{aligned} &\{V\}_{kn} = v_{xk}\Phi_n(\boldsymbol{v}_k), \quad \{W\}_{kn} = v_{yk}\Phi_n(\boldsymbol{v}_k), \\ &\{A\}_{kn} = \frac{\partial \Phi_n}{\partial v_x}(\boldsymbol{v}_k), \quad \{B\}_{kn} = \frac{\partial \Phi_n}{\partial v_y}(\boldsymbol{v}_k), \\ &\{C\}_{kn} = C[\Phi_n(\boldsymbol{v}_k)] \end{aligned} \tag{4.13}$$

$$k, n = 1, \cdots, N.$$

Elements of matrices $\boldsymbol{A}$ and $\boldsymbol{B}$ can be further reduced by converting to local indices: $\partial\Phi_n(\boldsymbol{v}_k)/\partial v_x = \phi'_{\kappa(n)}(v_{xk})\phi_{\ell(n)}(v_{yk})\phi_{2m(n)}(v_{xk})$ and $\partial\Phi_n(\boldsymbol{v}_k)/\partial v_y = \phi_{\kappa(n)}(v_{xk})\phi'_{\ell(n)}(v_{yk})\phi_{2m(n)}(v_{xk})$. The collision operator will be expounded upon later in Section 4.3.2, and a discrete form labeled C_d will be introduced.

The update equation for the expansion coefficient vectors, (4.10), needs additional explanation. First of all, the matrix $\boldsymbol{T}$ is called the transformation matrix. This $N \times N$ matrix enables transformation from an N vector, whose elements are the the distribution function evaluated at each collocation point, to the expansion coefficient vector, for any discrete space point and pseudo time $(i, j; h)$:

$$\alpha_{ij}^{h} = \boldsymbol{T} f_{ij}^{h}, \tag{4.14}$$

$$\{f_{ij}^h\}_k = f_{ij}^h(v_k),$$
$$k = 1, \cdots, N.$$

The transformation matrix is readily determined from formula (4.8), which gives its inverse:

$$\{T^{-1}\}_{kn} = \Phi_n(v_k). \tag{4.15}$$

It is therefore evident the discrete distribution function can be equivalently represented with either of two vector fields, α_{ij}^h or f_{ij}^h. These representations will be called, for sake of brevity, α and f representations. Update equation (4.10) is simply the first-order forward-Euler formula (see Section 2.2.1.2) for a single, variable pseudo-time step in the α representation of the carrier distribution.[5]

Second, the forward-Euler pseudo-time stepping scheme has a discretization error of order $\Delta\tau^h$ for the hth pseudo-time step. This does not match the second-order spatial derivative accuracy of difference formulas (4.11) and (4.12). Since the large-h behavior of the distribution function is of sole concern, evolution of the pseudo transient is irrelevant (as long as a stable steady state is achieved). Thus, a first-order pseudo-time stepping scheme is, in fact, desirous because of its simplicity and relative insensitivity to numerical instability (when compared with higher-order, explicit or implicit, schemes). In addition, the variable pseudo-time step feature can enhance convergence rates if comparatively large step sizes are used during the initial pseudo transient.

To completely specify the FD-spectral equations, boundary conditions must be incorporated. Along the front spatial boundary (refer to Fig. 4.1) a carrier distribution corresponding to an equilibrium Maxwellian is injected. Along the rear spatial boundary no carriers are injected. Coupling to boundary points with $j = 1$ and $j = M$ is effected by setting

$$\{W\alpha_{i1}^h\}_k = \begin{cases} v_{yk} f_o(v_k) & k = 1, \cdots, N/2, \\ \{W\alpha_{i2}^h\}_k & k = (N/2)+1, \cdots, N, \end{cases} \tag{4.16}$$
$$i = 1, \cdots, L,$$

[5] On substitution of (4.2) into (4.1), the continuous pseudo-time derivative yields the rate of change of the distribution function at each collocation point (for $v = v_k$). These derivatives can be arranged in vector form; after forward-Euler discretization they become $(f_{ij}^{h+1} - f_{ij}^h)/\Delta\tau^h$. Multiplying the residual equation through by T produces the desired result, (4.10).

where the equilibrium Maxwellian is

$$f_o(v_k) = \mathcal{N} \exp\left(-\frac{m^*}{2k_BT} v_k^2\right), \tag{4.17}$$

and

$$\{W\alpha_{iM}^h\}_k = \begin{cases} \{W\alpha_{iM-1}^h\}_k & k = 1, \cdots, N/2, \\ 0 & k = (N/2)+1, \cdots, N, \end{cases} \tag{4.18}$$

$$i = 1, \cdots, L.^6$$

The quantity $\mathcal{N}$ is a suitable normalization constant and v_k is the velocity magnitude, $(v_{xk}^2 + v_{yk}^2 + v_{zk}^2)^{1/2}$, at the kth collocation point. All the above equations have been written assuming an even number of symmetrically located collocation points labeled $k = 1, \cdots, N/2$ for $v_{yk} > 0$ and $k = (N/2)+1, \cdots, N$ for $v_{yk} < 0$, which will be adhered to throughout the rest of this chapter. Additional equations are needed when conditions at the left and right spatial boundaries are incorporated (refer again to Fig. 4.1 for orientation). For this problem spatially periodic symmetry in the x direction will be presumed, with the left and right spatial boundaries being planes of mirror symmetry. This implies that no net carrier flow across these boundaries can occur. Mathematically, carriers are regarded as being specularly reflected upon interaction with either the left or right boundary. Appendix H contains a thorough analysis of the this mirror-symmetric boundary condition. The essential result of the analysis is that the carrier distribution possesses even v_x parity at left and right boundaries [see boundary condition (H.3)] It is convenient to situate the actual physical boundaries half-way between the boundary (mesh) points at x_1 and x_L and the internal points x_2 and x_{L-1}, respectively. In this case (4.9) and (4.10)—modified by boundary Eqs. (4.16) through (4.18)—remain valid for indices $i = 2, L-1$ and $j = 1, \cdots, M$. Coupling to boundary points can still occur, for which the

[6]The second line $[k = (N/2)+1, \cdots, N]$ of (4.16) and the first line $(k = 1, \cdots, N/2)$ of (4.18) are artificial boundary conditions. They arise from using a second-order-correct finite-difference formula (4.11) or (4.12) to approximate continuous first-order spatial derivatives. They are purely a manifestation of the numerical approximation process and are not associated with any of the "physically correct" conditions that would be applied in an analytical treatment of the continuous BTE (4.1). The artificial boundary conditions are expected to have a minimal effect on solution accuracy (at least much smaller than the improvement obtained by replacing first-order differencing formulas with those of second order).

(v_x-symmetry) expansion coefficient relations

$$\{\alpha^h_{1j}\}_n = \{\alpha^h_{2j}\}_n(-1)^{\kappa(n)-1} \tag{4.19}$$

and

$$\{\alpha^h_{Lj}\}_n = \{\alpha^h_{L-1j}\}_n(-1)^{\kappa(n)-1} \tag{4.20}$$

$$n = 1, \cdots, N,$$
$$j = 1, \cdots, M,$$

must hold.[7]

Boundary conditions for large velocity regions that do not include any spatial boundaries—that is, the collocation cube faces at internal mesh points in Fig. 4.1—have been neglected. This is permitted, because it is assumed that the basis functions decay to zero for large (infinite) velocity magnitude. A similar situation has been faced in connection with the (z, v_ρ, v_z) problem (see the end of Section 3.2.1.3).

Bulk iteration equations (4.9) and (4.10), along with boundary equations (4.16) through (4.20), are incomplete without initial conditions in pseudo time. Only a first-order pseudo-time derivative appears in BTE (4.1); hence, a single initial condition is sufficient. Given no *a priori* information with regard to the form of the final steady-state distribution function, an equilibrium Maxwellian distribution offers a reasonable starting condition at $h = 0$. In terms of vector expansion coefficients,

$$\boldsymbol{\alpha}^0_{ij} = \boldsymbol{T}\boldsymbol{f}_o, \tag{4.21}$$

$$\{\boldsymbol{f}_o\}_k = f_o(\boldsymbol{v}_k),$$
$$i = 1, \cdots, L,$$
$$j = 1, \cdots, M,$$
$$k = 1, \cdots, N.$$

Of course, an alternate initial condition could prove superior if information concerning the form of the final steady-state distribution function is available. For example, once the steady-state distribution function has been calculated

[7] The above relations follow directly from boundary condition (H.3) and expansion (4.3).

using initial condition (4.21), it (or any of its transient pseudo-time samples) can be used as an initial condition for any subsequent, closely related calculation. From actual experience, this procedure has been found to greatly enhance steady-state convergence rates for pseudo-transient iteration of the FD-spectral equations.

4.3 The Collision Matrix

Collision phenomena are incorporated into this iterative formulation of the FD-spectral method through the collision matrix C in (4.9). Elements of the collision matrix depend on the collision operator C through (4.13). In following with the analysis of the (z, v_ρ, v_z) problem, the same single-valley model of the silicon semiconductor system, which includes deformation-potential acoustic and nonpolar optic phonon scattering, will be used. Details of this model have been covered in Section 3.2.2; supplementary information can be found in Appendix E.

4.3.1 Deformation-Potential Acoustic and Nonpolar Optic Scattering Rates

Deformation-potential acoustic and nonpolar optic phonon scattering rates have already been presented in Section 3.2.2.1, Eqs. (3.27) through (3.30), and will not be rewritten here. The primary point of difference between the collision term for Section 3.2's (z, v_ρ, v_z) problem and the present problem is that the velocity vectors $\boldsymbol{v}$ and $\boldsymbol{v}'$ now depend on three Cartesian variables v_x, v_y, and v_z.[8]

4.3.2 Matrix Elements

The action of the collision operator on a basis set element involves integration over constant-energy "shells" in velocity space [according to (3.27), (3.28), and general formulas (1.3) and (1.4)]. In this instance

[8]For instance, $\varepsilon = m^* v^2/2$ where $v^2 = v_x^2 + v_y^2 + v_z^2$ in scattering rates (3.27) through (3.30).

$$
\begin{aligned}
C[\Phi_n(v)] &= \int_{-v}^{v}\int_{-(v^2-\eta^2)^{1/2}}^{(v^2-\eta^2)^{1/2}} d\xi d\eta\ S_a(\xi,\eta,v) \\
&\times \phi_{\kappa(n)}(\xi)\phi_{\ell(n)}(\eta)\phi_{2m(n)}(\sqrt{v^2-\xi^2-\eta^2}) \\
&+ \int_{-(v^2-v_o^2)^{1/2}}^{(v^2-v_o^2)^{1/2}}\int_{-(v^2-v_o^2-\eta^2)^{1/2}}^{(v^2-v_o^2-\eta^2)^{1/2}} d\xi d\eta\ S_o^-(\xi,\eta,v) \\
&\times \phi_{\kappa(n)}(\xi)\phi_{\ell(n)}(\eta)\phi_{2m(n)}(\sqrt{v^2-v_o^2-\xi^2-\eta^2}) \\
&+ \int_{-(v^2+v_o^2)^{1/2}}^{(v^2+v_o^2)^{1/2}}\int_{-(v^2+v_o^2-\eta^2)^{1/2}}^{(v^2+v_o^2-\eta^2)^{1/2}} d\xi d\eta\ S_o^+(\xi,\eta,v) \\
&\times \phi_{\kappa(n)}(\xi)\phi_{\ell(n)}(\eta)\phi_{2m(n)}(\sqrt{v^2+v_o^2-\xi^2-\eta^2}) \\
&- \lambda_a(\varepsilon)\Phi_n(v) - \lambda_o^-(\varepsilon)\Phi_n(v) - \lambda_o^+(\varepsilon)\Phi_n(v). \qquad (4.22)
\end{aligned}
$$

Complete expressions for the scattering factors S_a, S_o^-, and S_o^+ are given in Appendix E [Eqs. (E.10), (E.11), (E.17), (E.20), and (E.21)]. The first three members on the right side of (4.22) are the acoustic and optic in-scattering contributions, while the remaining three members are the corresponding out-scattering contributions (see Section 3.2.2.2). Advantage of the mirror velocity symmetry has been taken in writing (4.22) since its integrals are actually performed over constant-energy half-shells ($v_z > 0$) and the result then doubled. Clearly, (4.22) is nothing more than a generalization of the (z, v_ρ, v_z) problem's (3.31).

The chances of evaluating the integrals of (4.22) in closed form are slim, if at all possible. In practice, numerical evaluation by means of double Gaussian quadrature (after Appendix C.2) has proved effective. The collision operator is therefore converted to discrete form C_d, from which elements of the collision matrix can be calculated [compare with (3.32)]:

$$
\begin{aligned}
\{C\}_{kn} &= C_d[\Phi_n(v_k)] \\
&= \sum_{\nu,\mu} w_\mu w_\nu S_a(\xi_\mu,\eta_\nu,v_k)\phi_{\kappa(n)}(\xi_\mu)\phi_{\ell(n)}(\eta_\nu)\phi_{2m(n)}(\sqrt{v_k^2-\xi_\nu^2-\eta_\mu^2}) \\
&+ \sum_{\nu,\mu} w_\mu w_\nu S_o^-(\xi_\mu,\eta_\nu,v_k)\phi_{\kappa(n)}(\xi_\mu)\phi_{\ell(n)}(\eta_\nu)\phi_{2m(n)}(\sqrt{v_k^2-v_o^2-\xi_\nu^2-\eta_\mu^2}) \\
&+ \sum_{\nu,\mu} w_\mu w_\nu S_o^+(\xi_\mu,\eta_\nu,v_k)\phi_{\kappa(n)}(\eta_\nu)\phi_{\ell(n)}(\xi_\mu)\phi_{2m(n)}(\sqrt{v_k^2+v_o^2-\xi_\nu^2-\eta_\mu^2}) \\
&- \lambda_a(\varepsilon_k)\Phi_n(v_k) - \lambda_o^-(\varepsilon_k)\Phi_n(v_k) - \lambda_o^+(\varepsilon_k)\Phi_n(v_k). \qquad (4.23)
\end{aligned}
$$

Quadrature is over the (v_x', v_y') plane, centered with respect to the origin, with weights (w_μ, w_ν) and samples (η_μ, ξ_ν). Outer and inner sum limits are prescribed by correspondence with integral limits in (4.22)

4.4 Numerical Implementation

4.4.1 Space Discretization Mesh

Equations derived in the foregoing section are defined throughout a two-dimensional space discretization mesh.[9] The mesh is made up of a planar, uniform array of of rectangular cells with centers located at (x_i, y_j) for $i = 1, \cdots, L$ and $j = 1, \cdots, M$ (not counting virtual mesh points). Cell dimensions Δx and Δy are fixed to simplify computation, but could be made to vary, in an optimal fashion, every pseudo-time step. This was not possible for the direct solution method of Chapter 3. A maximum mesh size of fifteen points along x $(L = 15)$ and thirty points along y $(M = 30)$ has been set so as not to unduly prolong computation times. At this maximum resolution, half as many points were needed in x as compared with y in order to maintain spatial isotropy.[10]

4.4.2 Basis Set

Predicated on the work of Chapter 3, a fixed Hermite-Gaussian basis set has been selected for all calculations in this chapter. Thirty-six basis functions are employed, resulting from combinations of constituent functions—six each in v_x and v_y, and one in v_z.[11]

---

[9]The terms "space discretization mesh" and "finite-difference mesh" are employed interchangeably.

[10]To see this better, refer to Fig. H.1 in Appendix H. Figure H.1 illustrates the infinite transverse-periodic geometry of the system at hand. On account of this geometry the distribution function needs only to be solved only in a half-unit cell (see the discussion of Appendix H).

[11]Only one v_z constituent function is used because of the computational limitations of the HP-1000F computer.

4.4.3 Solution of FD-Spectral Equations

Two steps are involved in solving the FD-spectral equations: calculation of the spectral matrices—V, W, A, B, and C—and subsequent iteration for the expansion coefficient vectors α_{ij}^h $(h \to \infty)$. Spectral matrix evaluation will be taken up first. It has been shown in Sections 3.1.3.3 and 3.2.3.3 that proper collocation point ordering reduces spectral matrix calculation time and storage requirements. The same is true here, although the collocation domain differs slightly. The domain forms a collocation cube in velocity space, as earlier noted, bounded as follows: $-\infty < v_{xk}, v_{yk} < +\infty$ and $0 < v_{zk} < +\infty$. Collocation point components v_{xk} and v_{yk} are distributed throughout the (v_x, v_y) plane with four-fold symmetry.[12] Thus, collocation point components are related by changes in sign from quadrant to quadrant in the (v_x, v_y) plane. To clearly elicit symmetries, spectral matrices are row ordered as follows: Matrix rows $k = 1, \cdots, N/4$, $k = (N/4)+1, \cdots, N/2$, $k = (N/2)+1, \cdots, 3N/4$, and $k = (3N/4)+1, \cdots, N$ are associated, in the order just written, with the first $(v_{xk}, v_{yk} > 0)$, second $(v_{xk} < 0, v_{yk} > 0)$, third $(v_{xk}, v_{yk} < 0)$, and fourth $(v_{xk} > 0, v_{yk} < 0)$ quadrant collocation points.[13] Row ordering is then accomplished through the correspondences $(v_{xk+(3N/4)}, -v_{yk+(3N/4)}, v_{zk+(3N/4)}) = (-v_{xk+(N/2)}, -v_{yk+(N/2)}, v_{zk+(N/2)}) = (-v_{xk+(N/4)}, v_{yk+(N/4)}, v_{zk+(N/4)}) = (v_{xk}, v_{yk}, v_{zk})$ for $k = 1, \cdots, N/4$.

Additional symmetries are revealed if the spectral matrices are column ordered.[14] Column ordering merely involves specification of a transformation rule between basis function global and local indices. Spectral matrix columns, labeled with the global indices $n = 1, \cdots, N/4$, correspond to all basis functions that have ϕ_κ and ϕ_ℓ both of even parity. The remaining columns are ordered similarly, with global indices $n = (N/4)+1, \cdots, N/2$, $n = (N/2)+1, \cdots, 3N/4$, and $n = (3N/4)+1, \cdots, N$ corresponding, as written, to constituent function parities ϕ_κ odd and ϕ_ℓ even, ϕ_κ and ϕ_ℓ both odd, and lastly, ϕ_κ even and ϕ_ℓ odd.[15]

---

[12]Fundamentally, this property is due to symmetries in extrema locations of ϕ_κ about $v_x = 0$ and ϕ_ℓ about $v_y = 0$.

[13]The total number of basis functions, N, is assumed divisible by four.

[14]Spectral matrices in Chapter 3 were not column ordered because the eventual savings in computational effort did not justify the increase in numerical "book keeping". With regard to the present high-dimensionality problem, however, the numerical book keeping is well justified by a major savings in computational effort.

[15]Notice the parity of ϕ_m is irrelevant, just as the sign of v_{zk} during row ordering. All

Arrays (D.1) and (D.2) in Appendix D portray the internal symmetries in each spectral matrix brought about from the foregoing row- and column-ordering procedures (refer to Section D.1). Each spectral matrix is partitioned into sixteen $N/4 \times N/4$ block matrices. For spectral matrices depicted by (D.1), the four block columns are identical save for changes in sign of the last three block rows. Such matrices will be denoted c symmetric in accordance with the "column symmetry" just described. Spectral matrices $\boldsymbol{V}$ and $\boldsymbol{W}$ have a sign pattern given by the upper symbols, while lower symbols pertain to the spectral matrices $\boldsymbol{A}$ and $\boldsymbol{B}$. These sign patterns can be verified upon examination of spectral matrix element equations (4.13), noting collocation quadrants along block rows and constituent function parities along block columns [refer to array (D.1)]. The collision matrix $\boldsymbol{C}$ has a particularly simple structure. According to (D.2), most of the elements of $\boldsymbol{C}$ are zero. Those that are not constitute the left-most block column, each block being identical. The structure of the collision matrix sparse can be understood if collision operator equation (4.22) is closely examined. Equation (4.22) implies that elements of $\boldsymbol{C}$ are a function of velocity magnitude (or energy) only. Consequently, the four block rows of $\boldsymbol{C}$ must be the same.[16] The basis function constituents, moreover, in (4.22) possess either even or odd parity, and so only when ϕ_κ and ϕ_ℓ are both even functions is there a nonzero in-scattering contribution.[17]

The spectral matrices, after proper row and column ordering, are c symmetric. These types of matrices can be efficiently put into computer memory simply by storing the nonzero matrix blocks of the top block row along with an associated sign pattern for matrix blocks in the last three block rows. The so-called boundary vector with elements given by the right side of (4.16)

---

this stems from the fact that the distribution's velocity dependence is mirror symmetric about the (v_x, v_y) plane.

[16]Remember that element rows that make up each block row differ from block row to block row by (v_x, v_y) collocation quadrant. Components of velocity are squared in determining velocity magnitude, so that it follows immediately that $\boldsymbol{C}$ is c symmetric.

[17]In terms of local indices, nonzero in-scattering contributions occur when κ and ℓ are both odd, whereas all other contributions with combinations of odd and even indices (κ, ℓ) cancel exactly to zero after integrals in (4.22) are evaluated. Incidentally, to further economize computational effort the sum limits and the scattering factors in (4.23) should be altered when calculating nonzero matrix entries. The scattering factors S_a, S_o^-, and S_o^+ should be multiplied by four, and the discrete lower limits should each be made to correspond with continuous lower limits $\xi = 0$ and $\eta = 0$.

$[k = 1, \cdots, N/2]$ can be similarly handled. Inspection of the boundary vector reflects the fact that only the first $N/4$ elements ($k = 1, \cdots, N/4$) need be stored. The second half of this vector $[k = (N/4) + 1, \cdots, N/2]$ can always be determined from its first half with the rule $v_{yk+(N/4)} f_o(v_k) = v_{yk} f_o(v_k)$ for $k = 1, \cdots, N/4$.

To finish this discussion of preliminary matrix evaluation, the symmetry of the transformation matrix $\boldsymbol{T}$ will be explored. The inverse transformation matrix $\boldsymbol{T}^{-1}$ is obviously c symmetric and possesses a sign pattern in accordance with the parity of ϕ_κ and ϕ_ℓ [see definition (4.15) with Φ_n replaced by $\phi_{\kappa(n)}\phi_{\ell(n)}\phi_{2m(n)}$]. Array (D.3) depicts $\boldsymbol{T}^{-1}$ with $N/4 \times N/4$ block elements $\boldsymbol{T}_1^{-1}, \pm\boldsymbol{T}_2^{-1}, \pm\boldsymbol{T}_3^{-1}$, and $\pm\boldsymbol{T}_4^{-1}$. In Section D.1, it is shown that there is a relationship between block elements of $\boldsymbol{T}$ and $\boldsymbol{T}^{-1}$. Array (D.10) depicts this relationship. Block elements of $\boldsymbol{T}$ and $\boldsymbol{T}^{-1}$ are themselves related through matrix inversion. The transformation matrix therefore possesses a symmetry along each block row—hereby denoted r symmetry—that is in a sense complementary to c symmetry. Again, as has been made clear for the c-symmetric case, the block elements and sign pattern can be stored efficiently in computer memory.

After ordering and evaluating the spectral matrices, the transformation matrix, and the boundary vector, the FD-spectral equations are ready for iterative solution. Iteration commences with an initial condition, (4.21) for instance, and in each subsequent pseudo-time step (4.9) and (4.10) are scanned throughout the space-discretization mesh ($i = 2, \cdots, L-1$ and $j = 2, \cdots, M-1$)—subject, of course, to the boundary equations (4.16) through (4.20). Similarities do exist between this iterative procedure and the one used in Section 2.2.3.3; however, this time iteration is for the vector quantity $\boldsymbol{\alpha}_{ij}^h$ as opposed to the scalar quantity f_{ij}^h (the latter quantity in Section 2.2.1.2's notation). To minimize asymmetric accumulation of numerical error over the space discretization mesh, two antisymmetric scanning patterns were used in alternating fashion for each pseudo-time step. With reference to Fig. 4.1, the first scanning pattern begins at the rear-left mesh point and proceeds left-to-right, rear-to-front. The second scanning pattern begins at the front-right mesh point and proceeds right-to-left, front-to-rear. The iterative procedure outlined here is by no means unique. For example, a Jacobi iteration procedure (see Section 2.1.3.2) is also possible.[18]

[18]This type of iterative procedure was not selected because it offers a lesser degree of

Apart from increased storage efficiency, ordering of the spectral and transformation matrices permits a significant reduction in steady-state calculation time when performing the numerous vector-matrix multiplications demanded by the iterative equations (4.9) and (4.10). Normally a vector-matrix multiplication is an order N^2 process (referring to the number of scalar multiplications) for an N vector and an $N \times N$ matrix. But, since all the matrices in (4.9) and (4.10) are either c or r symmetric, the vector-matrix multiplications can be optimized through temporary storage of intermediate vector products. Specifics of an optimized vector-matrix multiplication algorithm are left to Appendix D.2. Actual tests have shown that the optimized multiplication algorithm reduces steady-state calculation time by a factor of four.

4.4.4 Numerical Errors

The fundamental origins of round-off and discretization errors have been remarked upon in Section 2.1.3.4. Round-off and discretization errors are manifested in different ways and in varying degrees of importance depending on the problem at hand. Generally, round-off error tends to be unimportant when numerical equations are solved iteratively. This is the case the iterative solution of the (x, y, v_x, v_y, v_z) problem. Round-off error usually does not accumulate to intolerable levels on account of the intrinsic error-canceling effect of iteration. Any round-off error that does accumulate is primarily connected with the order N^2 matrix-vector multiplications in (4.9) and (4.10) at each space mesh point.[19] When the FD-spectral equations are solved iteratively, numerical error is dominated by discretization error. This was observed for the iterative calculation in Chapter 2. In order to quantify the effects of finite-difference and spectral discretization errors, the parameters Δx and Δy, and N_κ, N_ℓ, and N_m, respectively, can be varied for a series of otherwise identical calculations. Changes in the carrier distribution function (either in f or α representations) are then monitored in much the same way as described for Chapter 2's (x, v_x, t) problem (see

numerical stability and requires roughly twice as much computer memory storage as the presently used Gauss-Siedel procedure. While on the subject of iterative procedures, Jacobi iteration of the FD-spectral equations would be exactly equivalent to solution of the time-dependent BTE [(4.1) where τ is replaced with t] by means of first-order, forward-Euler time-stepping.

[19] In contrast, round-off error in Chapter 3's direct solution method, Gaussian elimination, is associated with an order N^3 matrix-inversion process per space point.

Section 2.2.3.5). Spectral discretization error can further be assessed after resorting to the transform domain (see Sections 3.1.3.4 and 3.2.3.4) and determining whether the distribution function in the α representation decays sufficiently quickly with increasing local basis function indices κ, ℓ, and m. The finite size of the pseudo-time step $\Delta\tau^h$ contributes to discretization error as well. This error can be monitored like the finite-difference and spectral discretization errors above. Only the large-h, steady-state step size needs to be varied—the smaller the step size the smaller the associated discretization error. Step sizes throughout the initial pseudo transient have no bearing on discretization error, as long as they are not too large as to produce an numerical instability.

4.4.5 Numerical Stability

At the end of the previous section it was alluded that step size can effect numerical stability. The strategy behind efficient pseudo-transient iteration is to take relatively large pseudo-time steps initially in order to converge rapidly to a steady-state solution. Unfortunately, the step size cannot be made arbitrarily large, but is constrained according to CFL stability criteria (see Appendix B.1). Time-dependent calculations of Chapter 2 were also constrained by CFL stability criteria (see Sections 2.1.3.3 and 2.2.3.4). In point of fact, the (x, y, v_x, v_y, v_z) problem represents a vector, quasi-hyperbolic system [20], first-order in pseudo time; hence, the resulting FD-spectral equations must satisfy CFL stability criteria:

$$\sqrt{|v_{xk}|^2_{max} + |v_{yk}|^2_{max}} \leq \sqrt{\left(\frac{\Delta x}{\Delta\tau^h}\right)^2 + \left(\frac{\Delta y}{\Delta\tau^h}\right)^2} \tag{4.24}$$

and

$$\frac{|q|}{m^*}\sqrt{|E_{xij}|^2_{max} + |E_{yij}|^2_{max}} \leq \sqrt{\left(\frac{|v_{xk}|_{max}}{N_\kappa \Delta\tau^h}\right)^2 + \left(\frac{|v_{yk}|_{max}}{N_\ell \Delta\tau^h}\right)^2}. \tag{4.25}$$

CFL relations (4.24) and (4.25) are extensions of (2.14), (2.37) and (2.38). Here, grid velocities and accelerations are two-dimensional vector quantities whose magnitudes are to be compared with corresponding physical velocity and acceleration magnitudes. The maximum collocation velocity components are to be taken over all indices $k = 1, \cdots, N$. The maximum electric

field components are to be taken over the entire space-discretization mesh $i = 1, \cdots, L$ and $j = 1, \cdots, M$. Mesh accelerations, on the right side of (4.28), follow in analogy from those of Chapter 2, whereby velocity cell size is replaced with the mean velocity interval between collocation point components. The above CFL criteria establish necessary, but not sufficient, conditions for numerical stability.[20]

It is no new fact that numerical solution of first-order hyperbolic systems may lead to an unconditional numerical instability when (pseudo) time stepping is explicit and nontemporal derivatives are approximated with central difference formulas [Eqs. (4.11) and (4.12), for example], even if CFL criteria (4.24) and (4.25) are satisfied [20,21,23]. Stabilization can be achieved through introduction of small "diffusion" terms in the FD-spectral equations.[21] This procedure is frequently used in the numerical analysis of fluid flow, where it it commonly denoted pseudo-viscous stabilization [20]. According to Appendix B.2, pseudo-viscous stabilization of the present vector hyperbolic system can be achieved if the vector expansion coefficient α^h_{ij} in FD-spectral Eq. (4.10) is replaced with a weighted average of itself and its eight nearest neighbors:

$$\begin{aligned}
\alpha^h_{ij} \quad \longrightarrow \quad & (1 - \sigma_x - \sigma_y - \sigma_{xy})\alpha^h_{ij} \\
+ \quad & \sigma_x \left(\frac{\alpha^h_{i+1j} + \alpha^h_{i-1j}}{2} \right) \\
+ \quad & \sigma_y \left(\frac{\alpha^h_{ij+1} + \alpha^h_{ij-1}}{2} \right) \\
+ \quad & \sigma_{xy} \left(\frac{\alpha^h_{i+1j+1} + \alpha^h_{i-1j+1} + \alpha^h_{i+1j-1} + \alpha^h_{i-1j-1}}{4} \right).
\end{aligned} \tag{4.26}$$

Pseudo viscosities σ_x, σ_y, and σ_{xy} should be kept positive to avoid unsta-

[20]The CFL stability relations (4.24) and (4.25), have been obtained through semi-quantitative, semi-intuitive reasoning. A rigorous theoretical treatment of CFL stability would conclude that additional factors appear in (4.24) and (4.25). These factors depend on eigenvalues of matrices derived from the spectral and transformation matrices in combination with the discrete electric field. A mathematically rigorous stability analysis of a similar, but simpler, vector hyperbolic system has been carried out in Appendix B.1. (See also reference [20].)

[21]Assuming, of course, that CFL stability criteria are met.

ble "anti-diffusion". Generally speaking, the larger the pseudo viscosity the greater the stabilizing influence, until the sum of all the pseudo viscosities surpasses unity, at which point instability will occur (see Section B.2). "Diffusion errors" brought about by the use of substitution (4.26) can be minimized if pseudo viscosities are made as small as possible, just enough to ensure stabilization.[22]

4.5 Results and Discussion

4.5.1 Execution Rate

All numerical computations were implemented on an HP-1000F minicomputer.[23] Whenever possible EMA and VIS enhancement features (see Section 3.1.4.1) were used to increase memory storage and speed up arithmetic execution rates.

A fixed, thirty-six element ($N = 36, N_\kappa = N_\ell = 6, N_m = 1$) Hermite-Gaussian basis set consumed roughly two and one-half minutes calculation time in evaluating spectral matrices $\boldsymbol{V}$, $\boldsymbol{W}$, $\boldsymbol{A}$, $\boldsymbol{B}$. Approximately ten hours was spent performing double Gaussian quadrature for elements of the collision matrix $\boldsymbol{C}$ (to a numerical accuracy of one part in one hundred). Another two and one-half minutes, typically, was required to perform matrix inversions necessary in evaluating the transformation matrix $\boldsymbol{T}$. Full advantage of matrix symmetries was taken during this initial matrix evaluation phase, including the efficient matrix (and vector) storage scheme explained in Section 4.4.3.

Iterating (4.9) and (4.10) took on average one-half second per mesh point for every pseudo-time step. Nearly all this time was spent executing vector-matrix multiplications that have been optimized according to Appendix D.2. Pseudo-viscous stabilization entailed relatively little calculation time since it involved only vector operations.

All calculations were performed with a fixed space discretization mesh size of $L = 5$ and $M = 10$. Variable-sized pseudo-time steps were adjusted so as to minimize steady-state convergence time. A convergence criterion of

[22]Diffusion errors are expected to be vanishingly small, no greater than round-off or discretization errors, if pseudo viscosities are kept small.

[23]Because of hardware problems, some calculations were performed on a Digital Equipment Corporation VAX-750, set up to emulate the HP-1000F.

no more than one part in ten-million maximum variation (over the entire space mesh) in $|\alpha_{ij}^h|$ per pseudo-time step was chosen. Under this criterion, convergence was usually achieved after a few thousand complete space-mesh scans. Relatively little iteration time was spent evolving the initial, rapidly changing portion of the pseudo transient; in fact, most of the iteration time was spent during the large-h, asymptotic portion of the pseudo transient.

4.5.2 Solution Verification

By the convention established in Chapters 2 and 3, FD-spectral solutions were verified in three ways: tests without the collision term (ballistic), tests with the collision term, and finally, tests based on qualitative physical reasoning.

Ballistic tests were first performed for the case of vanishing x-directed electric field, that is, $E_{xij} = \{C\}_{kn} = 0$. In addition, the y-directed electric field was assumed independent of transverse position x. These conditions imply that solutions to the (x, y, v_x, v_y, v_z) problem are independent of x. For any x and fixed v_z the (x, v_x, v_y) dependence of solutions to the (x, y, v_x, v_y, v_z) problem corresponds exactly with ballistic solutions of Section 3.2's (z, v_ρ, v_z) problem.[24] Verification can then proceed through comparison with the previously verified, ballistic (z, v_ρ, v_z) problem. Relevant computational parameters for both problems were set to limits appropriate to the (x, y, v_x, v_y, v_z) problem. For example, the (x, y, v_x, v_y, v_z) problem used $M = 10$ and $N = 36$ ($N_\kappa = N_\ell = 6$), and so, in Chapter 3's notation, the (z, v_ρ, v_z) problem was set to use $L = 10$ and $N = 36$ ($N_\ell = N_m = 6$). All solutions to (z, v_ρ, v_z) and (x, y, v_x, v_y, v_z) problems agreed to within one part in one thousand.[25]

Ballistic tests were completed after allowing for full two-dimensional variation in space. Exact, analytical solutions to this ballistic problem are gen-

[24] If $Cf = 0$, the independent variable v_z in BTE (4.1) is just a parameter. Furthermore, the solution to (4.1) does not vary with x (given the x-independent boundary conditions of Section 4.2.3), so that the term $v_x \partial f/\partial x$ vanishes ($\{V\}_{kn} = 0$). Hence, the following correspondence exists between the (z, v_ρ, v_z) and (x, y, v_x, v_y, v_z) problems: $(y, v_x, v_y, E_y) \sim (z, v_\rho, v_z, E_z)$.

[25] The small discrepancy between solutions is greater than observed previously for the similar verification test in Section 3.2.4.2. This is not surprising because iterative and direct solution methods are used here, in contrast to solely direct solution methods used in Section 3.2.4.2.

erally too complex to warrant their use in verification. Instead, verification consisted of extensive and systematic "proof-reads" of the program code in conjunction with an extensive series of "real-time variable consistency checks", whereby each computer program variable is monitored during program execution. Computer program routines that execute vector-matrix multiplications involving V and A were especially scrutinized and were compared directly with the similar routines involving W and B.[26]

Tests that included acoustic and optic phonon collision terms were next performed. No closed-form analytical or independently calculated numerical solutions were available for comparison. Proper installation of acoustic and optic scattering rates [Eq. (4.23)] in the computer program was checked using the self-consistent integration technique already described in Section 3.1.4.2, but now extended to a three-dimensional velocity domain (v_x, v_y, v_z).

Final verification of the full (x, y, v_x, v_y, v_z) problem is predicated on qualitative physical reasoning. Solutions were examined near boundaries for correct behavior: $f \to 0$ for $v \to \infty$, $f \approx f_o$ in the entrance region $y \approx 0$, $f \approx 0$ in the exit region $y \approx L_y$, and $f(\cdots, v_x, \cdots) = f(\cdots, -v_x, \cdots)$ at left and right reflective boundaries $x = 0$ and $x = L_x$. Spatial invariance of the integrated y component of current density (see Appendix I), $\int_0^{L_x} dx\, J_y(x, y)$, was checked. This integrated quantity varied minimally (less than ten percent of mean, typically) in a manner reminiscent of current density $J_z(z)$ in Chapter 3's (z, v_ρ, v_z) problem. The influence of acoustic and optic scattering on the overall shape of the distribution function agreed well with physical expectation. Both distribution spherical symmetrization and carrier heating effects due to acoustic and optic scattering, respectively, were observed.[27]

4.5.3 Numerical Solutions

Physical parameters employed in these calculations are identical to those listed in Table 3.2. Computational parameters are listed in Table 4.1 and should all be self-explanatory. A contour plot of the electric potential is displayed in Fig. 4.2. The selection of this "saddle-shaped" potential was conditioned by an analytical model developed for the permeable-base transistor [27].

[26]Computer routines involving W and B are at this point considered verified, as the verification process described in the preceding paragraph has been carried through.

[27]A physical explanation of these effects is given in Section 3.2.4.3.

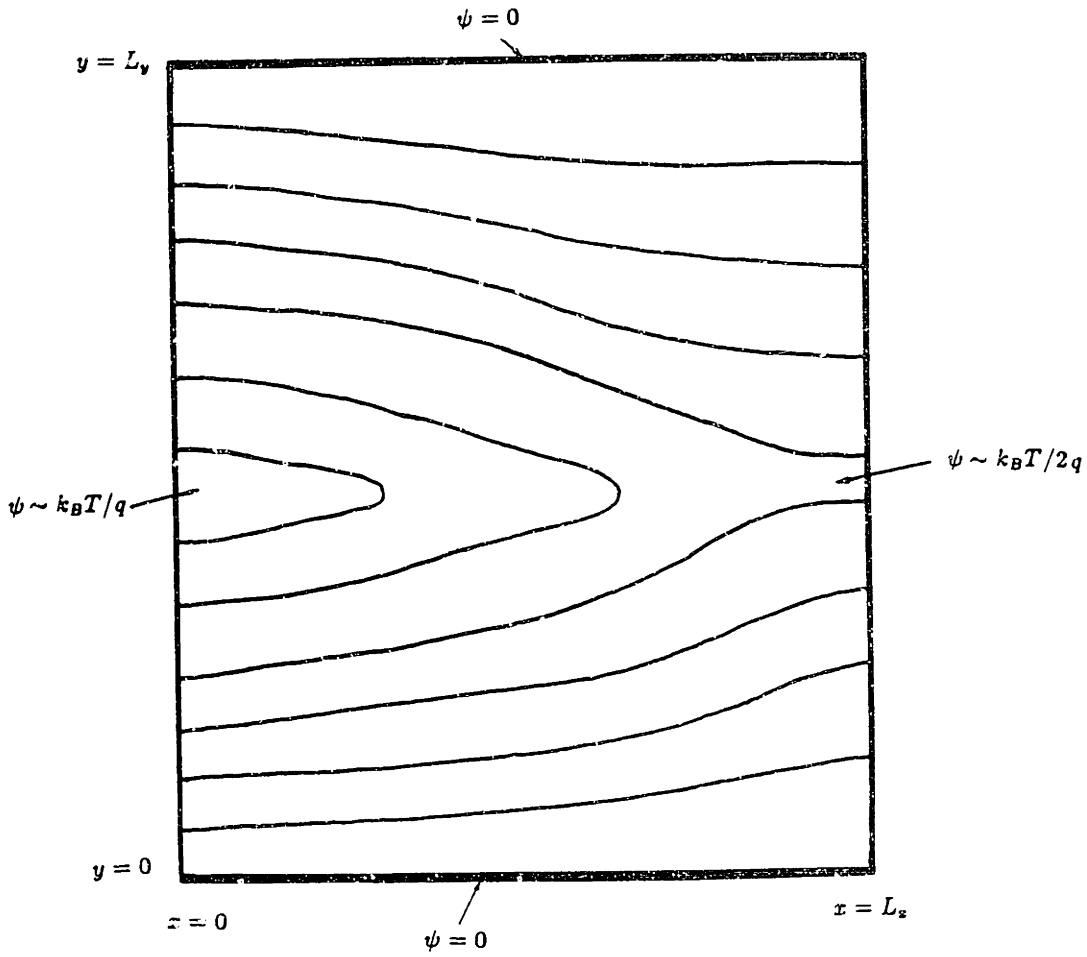

Figure 4.2. Contour plot of potential versus (x, y).

Quantity	*Value*	*Units*
Number of ϕ_κ constituent functions, N_κ	6	—
Number of ϕ_ℓ constituent functions, N_ℓ	6	—
Number of ϕ_m constituent functions, N_m	1	—
Number of x points, L	5	—
Number of y points, M	10	—
Cell size, Δx	1.00×10^{-9}	meters
Cell size, Δy	5.00×10^{-10}	meters
Pseudo-time step (minimum), $\Delta\tau^h$	1.00×10^{-15}	seconds
Number of iterative scans	~ 2500	—
Average change in $\lvert\alpha_{ij}^h\rvert$ per iterative scan (steady state)	$\sim 10^{-7}$	—

Table 4.1: Computational parameters for the (x, y, v_x, v_y, v_z) problem.

In all forthcoming results optic phonon scattering has not been suppressed as was done previously in Section 3.2.4.3. In addition, spatial scales have been purposely reduced to elicit ballistic effects.[28]

The y-dependence of the carrier distribution versus v_y has been found to behave in a manner similar to Fig. 3.7 for the (z, v_ρ, v_z) problem. The distribution function is characterized by three spatial regions: an entrance ($y \approx 0$) region, an exit ($y \approx L_y$) region, and a transition ($y \approx L_y/2$) region that encompasses the saddle point in potential. The carrier distribution is spherically symmetric and near equilibrium in the entrance region, whereupon it becomes a relatively rapidly varying function of y and v_y in the transition region (because of large fields and concentration gradients), and finally it becomes highly asymmetric in the exit region. The detailed account given in Section 3.2.4.3 provides an explanation of the behavior just described. In referring back to Section 3.2.4.3, it should be kept in mind that the additional degrees of freedom (independent variables) in space and

[28]Spatial scales have been chosen extremely small and are, to a degree, "physically unrealistic" given the potential of Fig. 4.2. Under this ballistic regime, with weak acoustic and optic scattering, the thirty-six-element basis set should provide sufficient accuracy. Calculations in which scattering is more prominent should be performed using larger basis sets (at least $N_\kappa = 8$, $N_\ell = 10$, $N_m = 3$, $N = 240$). This is estimated to require eighty times the present computational effort, without any algorithm optimisation. (See Section 5.3 concerning array processors.)

velocity associated with this problem only affects the mathematics but does not alter the underlying physical processes. It has also been observed that the y-dependence of the carrier distribution versus v_x, for fixed v_y and v_z, is analogous to Fig. 3.8. The general behavior of the carrier distribution in the entrance, transition, and exit regions agrees with that described above.

A better feel for the spatial variation of the distribution function can be obtained by noting Fig. 4.3. Plotted are contours of constant carrier concentration n as a function of discrete position (x_i, y_j). Carrier concentration was determined through zeroth moment evaluation of the distribution function in accordance with the prescription laid out in Appendix I. Carriers are seen to reside in greatest number near regions of local minima in potential, as expected. Notice that there is a rapid decrease in carrier concentration just beyond the potential saddle point and towards the device exit. This behavior is a direct consequence of current continuity in the steady state ($\nabla_r \cdot \boldsymbol{J} = 0$) and the fact that the carriers acquire progressively larger field-directed velocity passing through the transition region (refer to Fig. 4.4 and the discussion of the next paragraph).

The velocity field associated with the carrier distribution is pictured in Fig. 4.4. Proportionally scaled, mean velocity vectors $(\bar{v}_x, \bar{v}_y)$ have been drawn at selected points in the spatial domain. These vectors were determined via first moment evaluation of the carrier distribution (after Appendix I) and subsequent division by the local carrier concentration. It is readily seen that carrier flow is directed from entrance to exit, with an initially small $\bar{v}_y$ component in the quasi-equilibrium entrance region and an increasingly larger $\bar{v}_y$ component beyond the the saddle point and into the nonequilibrium transition and exit regions. There is an inverse correlation between carrier concentration and average velocity magnitude (compare Figs. 4.3 and 4.4) as might be guessed from a current continuity argument.[29]

For completeness a few closing remarks will be made concerning flux correction. The iterative FD-spectral method presented in this chapter is

[29]Current density is related to concentration and velocity by $\boldsymbol{J} = qn(\boldsymbol{r})\bar{\boldsymbol{v}}(\boldsymbol{r})$. Steady-state current continuity asserts $\nabla_r \cdot \boldsymbol{J} = 0$. The inverse correlation mentioned above is only qualitative and therefore approximate. If the continuity equation is integrated with respect to x from 0 to L_x, then $J_x(L_x, y) - J_x(0, y) + \int_0^{L_x} dx\ \partial J_y(x, y)/\partial y = 0$, where $\boldsymbol{J} = J_x(x, y)\hat{\boldsymbol{e}}_x + J_y(x, y)\hat{\boldsymbol{e}}_y$. At the left and right reflective boundaries (refer to Fig. 4.1 or H.1) the distribution function is mirror symmetric about the (v_y, v_x) plane, so that $J_x(0, y) = J_x(L_x, y) = 0$ and $d(\int_0^{L_x} dx\ J_y)/dy = 0$, which implies $\int_0^{L_x} dx\ J_y = \text{constant}$.

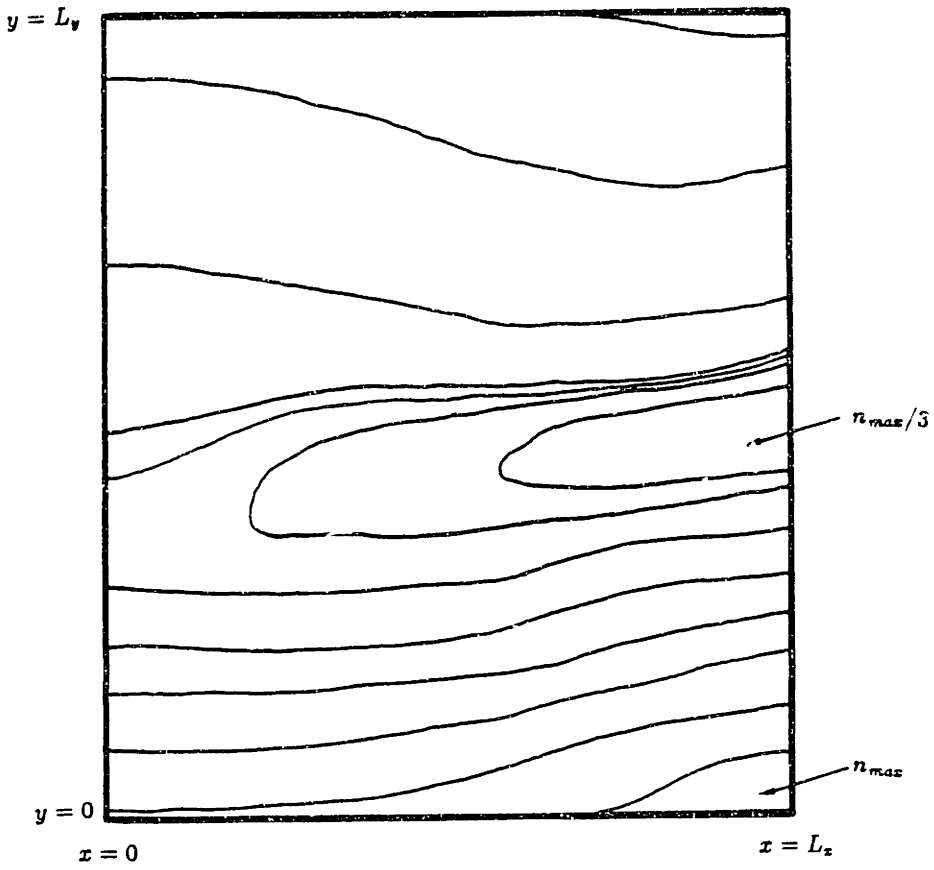

Figure 4.3. Contour plot of carrier concentration versus (x, y).

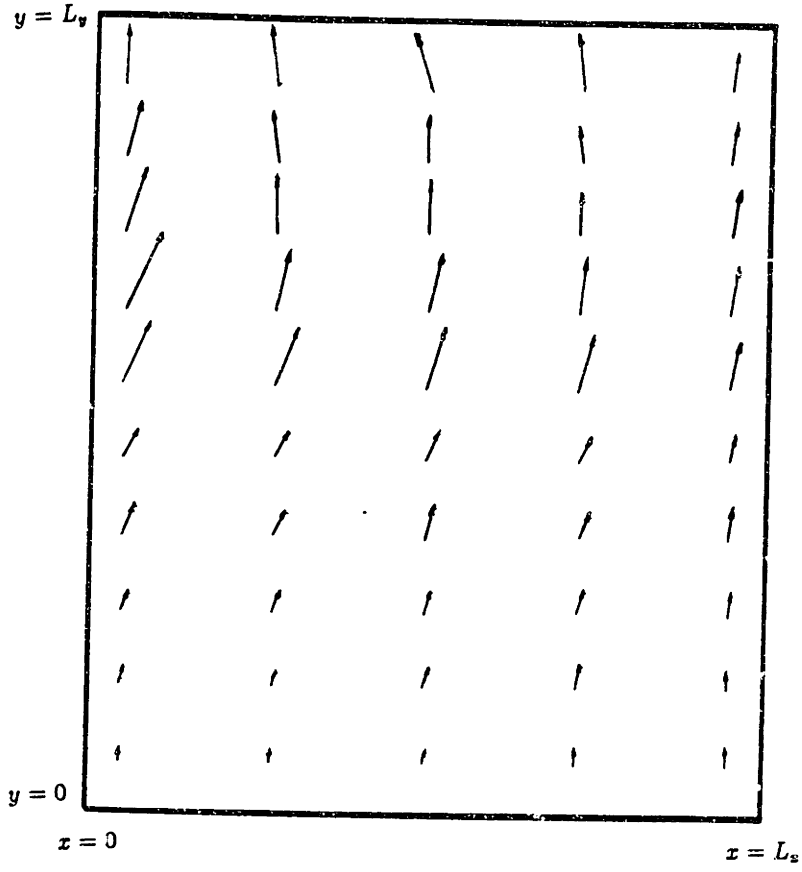

Figure 4.4. Vector plot of mean (x, y) velocity versus (x, y).

nonconservative ($\nabla_r \cdot J$ only approximately zero). The simplest (and recommended) option is to adopt Section 3.2.4.3's procedure, and statistically average the net transverse flux, $\int_0^{L_x} dx\, J_y$, over the y_j. Another option is to extend the conservative integral method that has been described in Chapter 3, footnote 38. But unfortunately, this approach suffers from various disadvantages, as has been noted. A last possible option is to formulate a computationally efficient, iterative flux-correction scheme.

Chapter 5

Conclusion

5.1 Summary

The main thesis objective is the development of a numerical solution method, the FD-spectral method, for the BTE. Particular emphasis has been placed on solving the time-independent BTE in the context of semiconductor device simulation. This main objective, along with the secondary objectives outlined in Section 1.3, has been successfully met through completion of a hierarchical sequence of numerical calculations.

At first, preliminary investigative calculations were performed. The BTE was solved in relatively simple systems by means of two established numerical methods, the Rees integral and the finite-difference methods (see Chapter 2). These calculations were invaluable in exposing many important issues that were relevant to the subsequent FD-spectral calculations. More practically, solutions obtained from these preliminary calculations were essential in order to establish benchmark solutions for future solution verification.

This next level of calculation hierarchy involved FD-spectral solution of the low-dimensionality BTE. These calculations represent a major thesis contribution and consequently will be reviewed here in greater detail. The FD-spectral calculations, in order of increasing complexity, have been denoted the (x, v_x) and (z, v_ρ, v_z) problems, and have been carried out for a one-dimensional, cusped-barrier device structure (see Chapter 3). A variety of spectral basis sets, derived from standard mathematical functions—Fourier, Tchebycheff, and Hermite-Gaussian—have been incorporated in the calculations. Overall computational efficiency was achieved through collocation

residual weighting. A mixed, first-order finite-difference scheme was implemented in order to convert spatial derivatives to discrete form. The FD-spectral equations generated for these two problems possessed a large block-tridiagonal coefficient matrix. For the sake of computational efficiency, these FD-spectral equations were solved directly via Gaussian elimination. The computational effort associated with this direct solution procedure scales as N^3 per space discretization-line point (where N is the number of basis functions.)

The last, most complex level in the calculation hierarchy dealt with FD-spectral solution of the high-dimensionality BTE. Calculations undertaken at this level represent the most significant thesis contribution in connection with the simulation of real, modern-day semiconductor devices. A two-dimensional transversally periodic and mirror-symmetric device structure was simulated, which has been denoted the (x, y, v_x, v_y, v_z) problem (see Chapter 4). Spectral collocation was performed in conjunction with a Hermite-Gaussian basis set, resulting in good overall computational efficiency. A highly accurate centered, second-order space differencing scheme was also used; instabilities relating to this differencing scheme were effectively removed upon inclusion of pseudo viscosities. Discretization of the pseudo-time derivative was handled with a first-order, variable-step-sized forward-Euler scheme, modified for "Gauss-Siedel" iteration. The FD-spectral equations for the (x, y, v_x, v_y, v_z) problem possess a very large banded block-tridiagonal coefficient matrix, thereby precluding the the possibility of a computationally efficient direct solution procedure. To overcome this difficulty, the FD-spectral equations have been solved by iterative pseudo-transient evolution. This iterative solution procedure scales in computational effort as N^2 per space discretization-mesh point per pseudo-time step.

5.2 Assessment of the FD-Spectral Method

Based on the results of this thesis it is now possible to assess realistically the FD-spectral method, not only as a means of solving the BTE for device simulation, but also as a general numerical solution technique applicable to a wide class of mathematical problems. Here are some of the more noteworthy features of the FD-spectral method:

- *Computationally robust*—The FD-spectral method is computationally robust. Fourier, Tchebycheff, and Hermite-Gaussian basis sets result in well-conditioned FD-spectral equations. Whether the FD-spectral equations are solved directly or iteratively, they are relatively insensitive to reasonably small numerical errors (round off and discretization).[1]

- *High accuracy and fast execution*—Compared with other general numerical solution techniques, such as the finite-difference and finite-element methods, the FD-spectral method achieves equivalent if not superior accuracy, depending on the specific problem being solved, for a fixed execution time (in other words, computational effort). It is evident, however, that when it comes to solution of the BTE in semiconductor device structures the FD-spectral method is definitely of superior accuracy, comparable with that of the Monte Carlo method, for example. This is largely because of the excellent interpolatory characteristics of the spectral basis set.

  It is estimated that the FD-spectral method would execute ten to twenty times slower than a conventional drift-diffusion approach of equivalent accuracy. The large FD-spectral execution time reflects a "true" increase in computational effort as warranted by the additional sophistication in transport physics. Relative to the Monte Carlo method the FD-spectral method is judged, on a basis of equal accuracy, to be ten to one-hundred times faster in execution rate.[2]

- *Low storage*—Computer memory storage requirements for FD-spectral variables are minimal. This follows from the compact spectral representation of the distribution function in combination with the low number of space-point couplings associated with the finite-differencing of space derivatives. The FD-spectral equations constitute a block-sparse system; furthermore, storage requirements for individual blocks (which make up spectral and transformation matrices) can be greatly reduced through proper row- and column-ordering.

---

[1] This behavior has also been observed in various tests, where, for example, the effect of adding a small perturbation to collocation point locations was studied.

[2] Coupling of Poisson's equation is not anticipated to affect significantly the relative execution rates quoted above.

- *Ballistic effects*—Ballistic effects are readily simulated using the FD-spectral method. Unlike the "spectral" method previously developed by Rees (see Section 1.2.3), there is no minimum length-scale constraint. In addition, tests performed in Sections 3.1.4.2 and 4.5.2 have demonstrated that the FD-spectral method is capable of resolving ballistic shock discontinuities.

- *Extension to higher dimensions*—Great interest lies in the extension of numerical solution methods to systems with many independent variables. As exemplified in Chapter 4, the FD-spectral method can be extended in an easy, straightforward manner. Increasing dimensionality will, of course, imply an increase in computational effort.

In all fairness, the FD-spectral method has some shortcomings:

- *Specificity of basis set*—The FD-spectral method has to be "customized" to the particular problem at hand through selection of an "optimal" basis set. Selecting an arbitrary, mathematically complete basis set will result in a workable algorithm but not necessarily a computationally efficient one. Basis set selection should be conditioned by any *a priori* knowledge of the carrier distribution, but otherwise is largely a matter of intuition along with trial and error. Finite-difference and finite-element methods offer greater mathematical generality.

- *Stabilization*—Numerical stabilization of the FD-spectral equations may be called for during iterative solution (see Section 4.4.5). This necessitates introduction of stabilizing pseudo-viscosity terms, causing a slight increase in overall complexity of the FD-spectral method.

- *Flux correction*—In Section 3.1.4.3 it has been noted that the FD-spectral method, when applied to the BTE, is not strictly conservative. A reformulation of the FD-spectral method or the use of a flux-correction algorithm may, in some cases, be required. Again, this would lead to an unwanted increase in complexity with, perhaps, a marked decrease in computational efficiency.

On balance, the desirable features of the FD-spectral method more than make up for its shortcomings.

5.3 Future Work

This thesis represents a foundation from which a multitude of applications, improvements, and extensions are possible. In this final section, suggestions for several promising areas of future investigation will be made.

The most obvious area of future investigation is simulation of real semiconductor devices. Of immediate necessity would be the establishment of an efficient numerical procedure for coupling Poisson's equation to the BTE. To keep things simple, initial device simulations should focus on semiconductor systems in which it is adequate to treat carriers as if they were in single spherical, parabolic bands, and in which only monopolar transport need be considered. A prime candidate for such a study is the silicon permeable-base transistor. Bipolar transport could be dealt with next through the inclusion of an additional spherical, parabolic band. The narrow-base silicon bipolar transistor would make a logical device choice at this point. Additional simulations can be carried through for devices in semiconductor systems with complicated multivalley band structures. Devices fabricated in III-V semiconductor materials fall into this category. For instance, the gallium arsenide permeable-base and metal-semiconductor field-effect transistors along with the heterojunction bipolar transistor are ideal for these types of studies. Another interesting advanced application of the FD-spectral method entails simulation of the high electron mobility transistor, particularly at low temperatures where it behaves as a quasi two-dimensional device. Provisions should be made to adequately model subband scattering in this device.

Nonlinear processes can also be included in future device simulations: carrier-carrier scattering (degenerate systems), high-field breakdown (Zener and avalanche), as well as direct and indirect, radiative and nonradiative band-to-band transitions. It should be said that nonlinear processes are not always bulk phenomena but may be associated with device boundaries and interfaces. Interface state generation, free-surface charge trapping, and diffuse surface scattering are all examples of nonlinear surface phenomena.

An alternative area of future investigation is the adaptation of the FD-spectral method to a computer system known as an array processor. Array processors are specialized computer systems with internal architecture optimized for high-speed execution of highly concurrent mathematical operations. FD-spectral equations can be efficiently solved on an array processor. An enormous savings in total computation time can be achieved

when the FD-spectral equation are solved iteratively. The long series of vector-matrix multiplications required for solution are ideally suited for array processing. With use of an array processor, extremely accurate solution of high-dimensionality problems (which entail a large number of basis functions and space-mesh points) can be brought within the realm of practicality.

The FD-spectral method is fundamentally a general numerical technique, from a purely mathematical viewpoint. There are many ways in which this general numerical technique can be modified and possibly improved. Variably sized finite-difference cells can be used, either continuously varying from point to point or in discontinuous "jumps" from region to region. The number of basis set elements can likewise be made variable. Other types of basis sets, such as Legendre or Gram polynomials [15,24] could be used, possibly in conjunction with a transformation of coordinate geometry. In fact, constituent functions need not be limited to a single class of mathematical functions; hybrid basis sets of this sort may be advantageous for some mathematical problems. Further, it is possible to customize the basis set by direct modification of the original set or by a formal mathematical optimization procedure such as that developed by Karhunen and Loeve [28]. Residual-weighting procedures like those covered in Section 1.2.2 (other than collocation) can be tested. Different methods can be developed through hybridization of the spectral method with the triangular finite-difference or finite-element methods [20,29]. Pseudo-transient iteration of vector-hyperbolic systems can be sped up by taking different-sized pseudo-time steps for each scalar FD-spectral equation [that is, each element of vector equations (4.9) and (4.10)] in accordance with CFL stability criteria for each corresponding collocation point. Fully time-dependent calculations can be performed through extension of the first-order, forward-Euler pseudo-time-stepping scheme to an explicit, second-order predictor-corrector time-stepping scheme [22]. Note also that pseudo-transient iteration naturally lends itself to solution of nonlinear problems (including those remarked upon in the previous discussion on device simulation applications). Lastly, powerful multigrid techniques [30] can be used to enhance the convergence rate for iterative solution of FD-spectral equations.

The final, and probably the most important area of future investigation that will be mentioned here, is FD-spectral solution of transport equations that govern quantum-mechanical semiconductor devices. Devices such as these violate many of the assumptions stated in Section 1.1.3 for quasi-

classical transport. Failure of quasi-classical transport theory is expected to occur in systems characterized with extremely small space scales (on the order of a few lattice constants or less) and extremely short time scales (on the order of a collision interaction time or less), particularly at low temperatures. A general, quantum-statistical transport theory predicated on the density-matrix formalism is then required. A quantum-mechanical analog of the BTE follows directly from this formalism and is commonly called the Wigner-Boltzmann transport equation [31]. Many issues remain unresolved in assessing the suitability of the FD-spectral method for solving the Wigner-BTE; nevertheless, with exciting advances being made in quantum-device technology[3] these issues are well worth exploring.

[3]See, for example, references [3,32] concerning the high electron mobility transistor and the resonant-tunneling diode.

Appendix A

The Rees Integral Method

Rees has developed an iterative integral method for solution of the BTE in spatially homogeneous systems. A complete derivation of the method's working equations has been carried out in Rees's original paper [12]. The key result is that the distribution function at discrete time h, $f^h(\boldsymbol{v})$, evolves in two steps: first, by application of the collision operator,

$$g^h(\boldsymbol{v}) = [(\Delta t^h)^{-1} + C] f^h(\boldsymbol{v}), \tag{A.1}$$

and second, by projection along a collision-free trajectory,

$$f^{h+1}(\boldsymbol{v}) = \int_0^\infty d\eta \ \exp\left(-\frac{\eta}{\Delta t^h}\right) g^h(\boldsymbol{v} - \frac{q}{m^*}\boldsymbol{E}^h\eta). \tag{A.2}$$

Equations (A.1) and (A.2) are entirely general and thus valid for any space-independent problem. If reference to the (v_ρ, v_z, t) problem of Chapter 2 is desired, the identification $\boldsymbol{v} = v_\rho\hat{\boldsymbol{e}}_\rho + v_z\hat{\boldsymbol{e}}_z$ and $\boldsymbol{E}^h = E_z^h\hat{\boldsymbol{e}}_z$ should be made.

A.1 Equivalence to the Finite-Difference Method

Before proceeding to a derivation of the velocity-discretized versions of (A.1) and (A.2) in the next section, the relationship between the Rees and finite-difference methods will be examined. The integration variable in (A.2) can be changed to ξ, $\xi = \eta/\Delta t^h$, so that

$$f^{h+1}(\boldsymbol{v}) = \Delta t^h \int_0^\infty d\xi \ \exp(-\xi) g^h(\boldsymbol{v} - \frac{q\Delta t^h}{m^*}\boldsymbol{E}^h\xi). \tag{A.3}$$

Expansion of (A.3) for small Δt^h implies

$$f^{h+1}(v) \approx \Delta t^h [g^h(v) - \frac{q\Delta t^h}{m^*} E^h \cdot \nabla_v g^h(v)], \tag{A.4}$$

after integrating over ξ. On elimination of $g^h(v)$ with the use of (A.1),

$$f^{h+1}(v) \approx f^h(v) - \frac{q\Delta t^h}{m^*} E^h \cdot \nabla_v f^h(v) + \Delta t^h C f^h(v) - \frac{q(\Delta t^h)^2}{m^*} E^h \cdot \nabla_v [C f^h(v)]. \tag{A.5}$$

In the limit $\Delta t^h \to 0$ the rightmost member vanishes and expression (A.5) merely becomes the variable-time-step forward-Euler formula, which is used extensively in finite-difference calculations (see Section 2.2.1.2):

$$\frac{f^{h+1}(v) - f^h(v)}{\Delta t^h} \approx -\frac{q}{m^*} E^h \cdot \nabla_v f^h(v) + C f^h(v). \tag{A.6}$$

A.2 Application to the (v_ρ, v_z, t) Problem

Velocity discretization of (A.1) and (A.2) for application to the (v_ρ, v_z, t) problem is straightforward. Discretization of (A.1) is trivial; the result has been written in Chapter 2 as Eq. (2.6). Discretization of (A.2) requires greater explanation. For simplicity, the quantity $\nu \doteq qE_z^h \Delta t^h / m^*$ in all forthcoming equations. Cast in the relevant velocity components, (A.2) changes to

$$f^{h+1}(v_\rho, v_z) = \int_0^\infty d\eta \ \exp(-\frac{\eta}{\Delta t^h}) g^h \left(v_\rho, v_z - \frac{\nu}{\Delta t^h}\eta\right). \tag{A.7}$$

A new integration variable, $\xi = v_z - qE_z^h \eta / m^*$, along with discretization of (v_ρ, v_z) to $(v_{\rho i}, v_{zj})$ yields

$$f^{h+1}(v_{\rho i}, v_{zj}) = \frac{\Delta t^h}{\nu} \exp\left(-\frac{v_{zj}}{\nu}\right) \int_{-\infty}^{v_{zj}} d\xi \ \exp\left(\frac{\xi}{\nu}\right) g^h(v_{\rho i}, \xi), \tag{A.8}$$

$$i = 1, \cdots, L-1$$
$$j = 2, \cdots, M-1,$$

for $q, E_z^h, \Delta t^h$, and m^* positive. The domain of integration for (A.8) can be split, giving

$$f^{h+1}(v_{\rho i}, v_{zj}) \ = \ \exp\left(-\frac{v_{zj}}{\nu} + \frac{v_{zj-1}}{\nu}\right) f^{h+1}(v_{\rho i}, v_{zj-1})$$

$$+ \quad \frac{\Delta t^h}{\nu} \exp\left(-\frac{v_{xj}}{\nu}\right) \int_{v_{xj-1}}^{v_{xj}} d\xi \exp\left(\frac{\xi}{\nu}\right) g^h(v_{\rho i}, \xi). \quad \text{(A.9)}$$

At this juncture it is useful to approximate the ξ dependence of $g^h(v_{\rho i}, \xi)$ by linear interpolation (see Appendix C.1) from $g^h_{ij-1} = g^h(v_{\rho i}, v_{xj-1})$ to $g^h_{ij} = g^h(v_{\rho i}, v_{xj})$:

$$g^h(v_{\rho i}, \xi) \approx \frac{g^h_{ij} - g^h_{ij-1}}{\Delta v_x}(\xi - v_{xj-1}) + g^h_{ij-1}. \quad \text{(A.10)}$$

Equation (A.10) is then substituted into (A.9), thereby enabling its integration, after which tedious algebraic manipulation leads to

$$f^{h+1}_{ij} = \exp\left(-\frac{v_{xj}}{\nu} + \frac{v_{xj-1}}{\nu}\right) f^{h+1}_{ij-1} + \frac{\Delta t^h}{\nu} \exp\left(-\frac{v_{xj}}{\nu}\right) \sum_{\mu=j-1}^{j} w_\mu g^h_{i\mu}, \quad \text{(A.11)}$$

where

$$w_{j-1} = -\frac{\nu}{\Delta v_x}\left[(\nu + \Delta v_x) \exp\left(\frac{v_{xj-1}}{\nu}\right) + \nu \exp\left(\frac{v_{xj}}{\nu}\right)\right] \quad \text{(A.12)}$$

and

$$w_j = -\frac{\nu}{\Delta v_x}\left[(\nu - \Delta v_x) \exp\left(\frac{v_{xj}}{\nu}\right) + \nu \exp\left(\frac{v_{xj-1}}{\nu}\right)\right] \quad \text{(A.13)}$$

For consistency, f^{h+1} in (A.11) has been subscripted like g^h to show its velocity dependence. Equation (2.7) follows from (A.11) by writing out ν in full.

Appendix B

Numerical Solution of First-Order Hyperbolic Differential Equations

B.1 The CFL Stability Criteria

Certain universal stability constraints exist whenever hyperbolic or quasi-hyperbolic differential equations are solved iteratively using an explicit time, or pseudo-time, stepping scheme. As first noted in Section 2.1.3.3 these constraints, commonly referred to as the CFL (Courant-Friedrichs-Lewy) stability criteria, can be readily deduced through intuitive physical arguments. A formal mathematical derivation of the CFL stability criteria will be the topic of this section. Two representative examples, a scalar and a vector hyperbolic system, will be studied.

Consider the first-order scalar hyperbolic equation

$$\frac{\partial u}{\partial t} = c\frac{\partial u}{\partial x}, \tag{B.1}$$

where $u = u(x,t)$ and c is some constant. The stability of (B.1) when subject to an explicit time-stepping scheme can be investigated following the method of von Neumann [20,23]. To assess numerical stability, a single Fourier mode $u(x,t) = \xi(t)\exp(ikx)$ is substituted into (B.1). Subsequent discretization in time, $\xi(t) \rightarrow \xi^h$, $t_h = t_o + h\Delta t$, requires that

$$\xi^{h+1} = (1 + i\Delta tkc)\xi^h, \tag{B.2}$$

$$h = 0, 1, 2, \cdots.$$

The solution to (B.2) is

$$\xi^h = (1 + i\Delta tkc)^h \xi^0. \tag{B.3}$$

The stability requirement is that the amplification factor[1] $|\xi^h/\xi^0|$ must be less than or equal to unity; this is true if

$$|1 + i\Delta tkc| \leq 1. \tag{B.4}$$

Obviously, inequality (B.4) can never be met (for $\Delta t > 0$ and $k, c \neq 0$); that being so, (B.3) will always become unbounded as $h \to \infty$, a characteristic of first-order hyperbolic equations when time-stepped explicitly.

In reality there are small, additional stabilizing terms associated with the original hyperbolic equation, the discretization errors themselves or sometimes ones introduced artificially. These terms induce stability provided that the relevant CFL criteria are not violated. To illustrate the effect of these stabilizing terms the quantity $\delta\partial^2 u/\partial x^2$ will be added to the right side of (B.1), with δ being a small positive constant, a diffusivity. The added diffusion term is a good way to achieve controlled stabilization; although in some situations [the (v_ρ, v_z, t) and (x, v_z, t) problems of Chapter 2] small diffusion terms arising from space discretization errors are inherently present and do not have to be introduced explicitly. In any event, a von Neumann analysis concludes that

$$\xi^h = (1 - \Delta t\delta k^2 + i\Delta tkc)^h \xi^0 \tag{B.5}$$

and

$$|1 - \Delta t\delta k^2 + i\Delta tkc| \leq 1 \tag{B.6}$$

as opposed to (B.3) and (B.4).

As a rule $\Delta t\delta k^2 \geq 0$ in (B.6), and for stability to be at all possible $|1 - \Delta t\delta k^2| \leq 1$. Hence, satisfaction of the CFL criterion

$$|c| \leq \frac{\Delta x}{\Delta t} \tag{B.7}$$

is necessary (but not always sufficient) to guarantee overall stability. This can be deduced by setting $|\Delta tkc| \leq 1$ for stability (assuming $1 - \Delta t\delta k^2 \approx 0$)

[1]Note that ξ^h may be complex.

and realizing that this inequality must be satisfied for all Fourier modes $\exp(ikx)$ with $|k| \leq \pi/\Delta x$.[2] A small amount of algebra then produces (B.7). A stronger condition for stability can be arrived at in a similar fashion, if specific bounds on $\Delta t \delta k^2$ are known.

The first-order vector hyperbolic equation,

$$\frac{\partial \boldsymbol{u}}{\partial t} = \boldsymbol{C}\frac{\partial \boldsymbol{u}}{\partial x} \tag{B.8}$$

where $\boldsymbol{C}$ is a constant square matrix, can be treated analogously. The vector equivalent of (B.5) is

$$\boldsymbol{\xi}^h = [(1 - \Delta t \delta k^2)\boldsymbol{I} + i\Delta t k \boldsymbol{C}]^h \boldsymbol{\xi}^0, \tag{B.9}$$

where $\boldsymbol{I}$ is the identity matrix. A diffusive stabilizing term $\delta \partial^2 \boldsymbol{u}/\partial x^2$ has been added to the right side of (B.8) and a vector Fourier-mode dependence $\boldsymbol{u}(x,t) = \boldsymbol{\xi}(t)\exp(ikx)$ has been posited. Matrix equation (B.9) is brought into tractable form by setting $\boldsymbol{\eta}^h = \boldsymbol{S}\boldsymbol{\xi}^h$ and choosing $\boldsymbol{S}$ so that $(1-\Delta t \delta k^2)\boldsymbol{I} + i\Delta t k \boldsymbol{C}$ is diagonal. In terms of $\boldsymbol{\eta}^h$ Eq. (B.9) transforms into

$$\boldsymbol{\eta}^h = [(1 - \Delta t \delta k^2)\boldsymbol{I} + i\Delta t k \boldsymbol{S}\boldsymbol{C}\boldsymbol{S}^{-1}]^h \boldsymbol{\eta}^0. \tag{B.10}$$

From the well-known properties of matrices, if the columns of $\boldsymbol{S}^{-1}$ consist of the eigenvectors of $(1-\Delta t \delta k^2)\boldsymbol{I} + i\Delta t k \boldsymbol{C}$, then the bracketed factor in (B.10) will be diagonal[3] with diagonal elements equal to the corresponding eigenvalues. The transformation matrix $\boldsymbol{S}$ will be taken to have this diagonalizing property. Instead of an amplification factor, elements of the diagonal amplification matrix $(1 - \Delta t \delta k^2)\boldsymbol{I} + i\Delta t k \boldsymbol{S}\boldsymbol{C}\boldsymbol{S}^{-1}$ must be bounded in magnitude by unity. In other words,

$$|1 - \Delta t \delta k^2 + i\Delta t k \lambda_{max}(\boldsymbol{C})| \leq 1. \tag{B.11}$$

where the symbol λ_{max} denotes the, possibly complex, eigenvalue of largest magnitude. In analogy with the scalar case, a necessary condition for overall stability is [compare (B.6) and (B.11)]

$$|\lambda_{max}(\boldsymbol{C})| \leq \frac{\Delta x}{\Delta t}, \tag{B.12}$$

[2]Fourier modes with $|k| > \pi/\Delta x$ are identical in discretized space to modes with $|k| \leq \pi/\Delta x$ since $\exp[i(k + mK)n\Delta x] = \exp(ikn\Delta x)$ for $K = 2\pi/\Delta x$ and integer n and m.

[3]The inverse transformation matrix $\boldsymbol{S}^{-1}$ is assumed to exist [33].

the CFL criterion.

The foregoing stability analysis extends without difficulty to systems of higher dimensionality, and can be applied directly to either the (v_ρ, v_z, t), (x, v_x, t), or (x, y, v_x, v_y, v_z) problems. Although not proved here, CFL criteria (2.14), (2.37), (2.38), (4.24), and (4.25), which were obtained intuitively, are expected to roughly agree with those obtained from von Neumann's method.[4]

B.2 Pseudo-Viscous Stabilization

It has been stated earlier that stabilization can in some cases occur automatically, with no need for external introduction of diffusion terms. Discretization errors in both (v_ρ, v_z, t) and (x, v_x, t) problems can be shown to be mathematically equivalent to a small, stabilizing diffusion term (see reference [21] for an example of this). The (x, y, v_x, v_y, v_z) problem, on the other hand, uses an accurate, second-order finite-difference derivative scheme in space. Stabilizing discretization errors are negligible and external artificial diffusion terms must be added to the governing equation. In this instance it is convenient to work with pseudo viscosities σ_x, σ_y, and σ_{xy} (refer to Section 4.4.5) since it is easier to introduce stabilizing terms after discretization of the original governing equation (4.1). The discrete version of (4.1), stabilized by continuous-to-discrete conversion of an added diffusion term, reads

$$\alpha_{ij}^{h+1} = \alpha_{ij}^h + \Delta t^h F_{ij}^h + \Delta t^h (\delta_x \Delta_x^2 \alpha_{ij}^h + \delta_y \Delta_y^2 \alpha_{ij}^h + \delta_{xy} \Delta_{xy}^2 \alpha_{ij}^h), \qquad \text{(B.13)}$$

where F_{ij}^h is a vector function of α_{ij}^h, $\alpha_{i\pm1j}^h$, and $\alpha_{ij\pm1}^h$ [refer to Eqs. (4.9) and (4.10)]; δ_x, δ_y, and δ_{xy} are the x, y, and "diagonal" diffusivities, respectively:

$$\Delta_x^2 \alpha_{ij}^h \doteq \frac{1}{(\Delta x)^2}(\alpha_{i+1j}^h - 2\alpha_{ij}^h + \alpha_{i-1j}^h), \qquad \text{(B.14)}$$

$$\Delta_y^2 \alpha_{ij}^h \doteq \frac{1}{(\Delta y)^2}(\alpha_{ij+1}^h - 2\alpha_{ij}^h + \alpha_{ij-1}^h), \qquad \text{(B.15)}$$

and

$$\Delta_{xy}^2 \alpha_{ij}^h \doteq \frac{1}{2[(\Delta x)^2 + (\Delta y)^2]}(\alpha_{i+1j+1}^h - 2\alpha_{ij}^h + \alpha_{i-1j-1}^h)$$

[4] Actual results from numerical calculations have directly validated the CFL criteria obtained by intuition.

$$+ \frac{1}{2[(\Delta x)^2 + (\Delta y)^2]}(\alpha^h_{i-1j+1} - 2\alpha^h_{ij} + \alpha^h_{i+1j-1}). \qquad \text{(B.16)}$$

The stabilization scheme described by substitution (4.26) is a direct consequence of (B.13) through (B.16). The pseudo viscosities in (4.26) and the diffusivities used here are therefore related:

$$\delta_x = \frac{\sigma_x(\Delta x)^2}{2\Delta t^h}, \ \delta_y = \frac{\sigma_y(\Delta y)^2}{2\Delta t^h}, \text{ and } \delta_{xy} = \frac{\sigma_{xy}[(\Delta x)^2 + (\Delta y)^2]}{2\Delta t^h}. \qquad \text{(B.17)}$$

The pseudo viscosities are all positive and their sum must be bounded by unity: $\sigma_x + \sigma_x + \sigma_{xy} \leq 1$; or else an instability may occur. This is not surprising because the pseudo viscosities $\sigma_x, \sigma_y, \sigma_{xy}$ can be interpreted as "weighting factors" in an approximation for α^h_{ij} in the unstabilized version of (B.13) ($\delta_x = \delta_y = \delta_{xy} = 0$) . At the other limit, it is clear that the pseudo viscosities can not be negative, since this would result in destabilizing "negative diffusion". In fact, the pseudo viscosities should be kept as small as possible to achieve numerical accuracy[5] but large enough to induce numerical stability.

[5]Remember that the diffusion terms in (B.12) will themselves produce additional numerical error in the final solution. Small pseudo viscosities ($\sigma_x, \sigma_y, \sigma_{xy} \ll 1$) should give rise to acceptably small numerical error.

Appendix C

Standard Numerical Methods

C.1 Interpolation

Often times in numerical calculations a function depends on a discrete set of independent variables. Function values at points that do not coincide with the discrete set are readily approximated by means of interpolation. In one dimension, given a discrete, real-valued function f_i with independent variable x_i,[1] the approximate value of its continuous version $f(x)$, for $x_i \leq x \leq x_{i+1}$, can be obtained with a linear fit between adjacent samples f_{i+1} and f_i:

$$f(x) \approx \frac{f_{i+1} - f_i}{x_{i+1} - x_i}(x - x_i) + f_i. \tag{C.1}$$

The linear interpolation formula (C.1) becomes in two dimensions a bilinear interpolation formula. The discrete function f_{ij} now depends on two variables, x_i and y_j. The approximate value of the continuous two-dimensional function $f(x,y)$, for $x_i \leq x \leq x_{i+1}$ and $y_i \leq y \leq y_{i+1}$, follows from a bilinear fit among four adjacent samples, $f_{ij+1}, f_{i+1j}, f_{ij+1}$, and f_{i+1j+1}:

$$\begin{aligned} f(x,y) \approx & \frac{f_{i+1j+1} - f_{ij+1} - f_{i+1j} + f_{ij}}{(x_{i+1} - x_i)(y_{j+1} - y_j)}(x - x_i)(y - y_j) \\ & + \frac{f_{ij+1} - f_{ij}}{y_{j+1} - y_j}(y - y_j) + \frac{f_{i+1j} - f_{ij}}{x_{i+1} - x_i}(x - x_i) + f_{ij}. \end{aligned} \tag{C.2}$$

[1] A uniform discretisation yields $x_i = x_o + i\Delta x$, $i = 1, 2, 3, \cdots$, for example.

C.2 Gaussian Quadrature

When a closed-form expression for some integral is not available, or perhaps too complicated, numerical integration is a useful alternative. Many numerical integration techniques exist: rectangular, trapezoidal, Simpson's, and so forth [15]. The numerical integration technique favored in this thesis is formally known as Gauss-Legendre quadrature, or simply Gaussian quadrature. Gaussian quadrature integration is especially accurate when integrating functions that are well approximated by high-order polynomials.

The m-point Gaussian quadrature formula for the integral of a function $f(x)$ over the interval [-1,+1] is

$$\int_{-1}^{+1} dx\ f(x) \approx \sum_{i=1}^{m} w_i f(x_i), \tag{C.3}$$

in which $x_1, \cdots, x_m$ are the (nonequidistant) zeros of the mth degree Legendre polynomial, $P_m(x) = (2^m m!)^{-1} d^m[(x^2-1)^m]/dx^m$ [24], and $w_1, \cdots, w_m$ are fixed constants known as the quadrature weights. Quadrature weights are calculated upon the assertion that (C.3) should be exact for the m functions $f(x) = P_i(x)$, $i = 0, \cdots, m-1$. The accuracy of the quadrature formula (C.3) is borne out by the fact that it can be shown to be exact for all polynomials of degree $2m-1$ or less (reference [15] gives a proof). Under circumstances where integration is over an arbitrary interval $[a, b]$ a linear transformation of integration variable "renormalizes" to the interval $[-1, +1]$:

$$\int_a^b dx\ f(x) = \frac{b-a}{2} \int_{-1}^{1} d\xi\ f\left[\frac{b-a}{2}\left(\xi + \frac{a+b}{b-a}\right)\right]. \tag{C.4}$$

A two-dimensional integration formula results from repeated application of (C.3) and (C.4) for each independent variable:

$$\int_{-1}^{1}\int_{-1}^{1} dxdy\ f(x,y) \approx \sum_{i=1}^{m}\sum_{j=1}^{m} w_i w_j f(x_i, y_j), \tag{C.5}$$

with interval renormalization

$$\int_a^b \int_c^d dxdy\ f(x,y) = \left(\frac{b-a}{2}\right)\left(\frac{d-c}{2}\right) \times \int_{-1}^{1}\int_{-1}^{1} d\xi d\eta\ f\left[\frac{b-a}{2}\left(\xi + \frac{a+b}{b-a}\right), \frac{d-c}{2}\left(\eta + \frac{c+d}{d-c}\right)\right]. \tag{C.6}$$

Precalculated samples and weights, x_i and w_i, for sixteen, thirty-two, sixty-four, and ninety-six point quadrature formulas are listed in reference [24]. Note further that integration accuracy can be improved beyond that of the ninety-six point formula if the integration domain is partitioned and quadrature is performed over each "subdomain". This integration procedure has been of frequent service throughout this thesis.

C.3 The Bisection Algorithm

One of the easiest ways to numerically determine the zeros or extrema of an arbitrary function is by means of the bisection algorithm. Determination of spectral basis function extrema is a good example of when the bisection algorithm can be usefully applied (refer to the discussion of Hermite-Gaussian functions in Appendix G).

Suppose it is known that a single zero or extremum (minimum or maximum) of a function $f(x)$ falls within the interval $[a, b]$. The zero or extremum can then be located through bisection of the interval $[a, b]$ into two intervals $[a, (a+b)/2]$ and $[(a+b)/2, b]$, followed by evaluation of $f(x)$ at the three distinct endpoints: $f(a), f[(a+b)/2]$, and $f(b)$. If a zero is being searched for, it is assumed to lie within $[a, (a+b)/2]$ when the sign of $f(a)$ is opposite to that of $f[(a+b)/2]$ and to lie within $[(a+b)/2, b]$ when the sign of $f[(a+b)/2]$ is opposite to that of $f(b)$. Note that $f(a)$ and $f(b)$ must be of opposite sign if the interval $[a, b]$ contains a single zero. If $f(a), f[(a+b)/2]$, or $f(b)$ is by some chance exactly zero the problem is concluded. In practice this does not frequently happen, and so the the algorithm just described is repeated, each time starting anew with the previous bisected interval in which the zero is assumed to lie. Thus, the zero can be located to within the endpoints of an arbitrarily small interval. An extremum can be searched for in a similar manner. In this case it is assumed to lie within $[a, (a+b)/2]$ when $f(a), f[(a+b)/2] \geq f(b)$ (maximum), or $f(a), f[(a+b)/2] \leq f(b)$ (minimum); and to lie within $[(a+b)/2, b]$ when $f[(a+b)/2], f(b) \geq f(a)$ (maximum), or $f[(a+b)/2], f(b) \leq f(a)$ (minimum). All other inequality relationships between the f values are ruled out by the assumption of a single extremum in the interval $[a, b]$. If the initial interval includes several zeros or extrema, either shortening the interval or resorting to a a process of elimination will resolve the problem.

C.4 The Theory of Spectral Collocation

A simple, intuitive analysis of spectral collocation will be presented here; the reader is directed to reference [14] for a more rigorous analysis.

Consider the equation $\mathcal{O}y(\boldsymbol{x}) = 0$, where $\mathcal{O}$ is a generalized operator (as in Section 1.2.2) and $y(\boldsymbol{x})$ is an unknown function of perhaps several variables, $\boldsymbol{x} = (x_1, \ldots, x_s)$. The spectral method involves the residual function,

$$R(\boldsymbol{x}) = \mathcal{O}\hat{y}(\boldsymbol{x}), \tag{C.7}$$

where the approximation for $y(\boldsymbol{x})$ is given by

$$\hat{y}(\boldsymbol{x}) = \sum_{n=1}^{N} \alpha_n \Phi_n(\boldsymbol{x}). \tag{C.8}$$

The basis functions Φ_n make up an orthogonal, mathematically complete set. The function $\hat{y}(\boldsymbol{x})$ is a good approximation to $y(\boldsymbol{x})$ when $R(\boldsymbol{x}) \approx 0$ over the relevant $\boldsymbol{x}$ domain. One way of choosing the N expansion coefficients α_n in (C.8) is according to a method first used by Galerkin [14]:

$$\int d^s\boldsymbol{x}\ \Phi_k(\boldsymbol{x}) R(\boldsymbol{x}) = 0, \tag{C.9}$$

$$k = 1, \cdots, N,$$

in which the residual is made orthogonal to the first N basis functions. Since the Φ_n are complete, (C.9) defines a mathematically well-conditioned, systematic procedure to determine the unknown expansion coefficients, and hence the spectral approximation $\hat{y}(\boldsymbol{x})$. It is expected that $|R(\boldsymbol{x})| \to 0$ as $N \to \infty$ for all $\boldsymbol{x}$.

An undesirable aspect of Galerkin's method is that the integrals (C.9) have often to be evaluated numerically, which can be computationally expensive for $s \geq 2$. A question then arises: Is there another method that possesses mathematical properties resembling those of Galerkin's method, but without need of the laborious integrations demanded by (C.9)? The answer is, of course, yes, the collocation (or pseudo spectral) method.

The collocation method forces the residual to vanish at N selected collocation points, $\boldsymbol{x}_1, \cdots, \boldsymbol{x}_N$. Equations for the expansion coefficients, or equivalently $\hat{y}(\boldsymbol{x})$, are simply

$$R(\boldsymbol{x}_k) = 0, \tag{C.10}$$

$$k = 1, \cdots, N.$$

In this instance, no integration is necessary. Collocation points are either the N zeros of Φ_{N+1} (zero collocation) or the N extrema of Φ_N (extrema collocation)[2]; this establishes a relationship between collocation and Galerkin methods. Figure C.1 depicts possible R and Φ_{N+1} in the simple, but informative, one-dimensional case ($s = 1$). A three-term ($N = 3$) spectral approximation is made. This zero-collocation procedure forces $R(x)$ to approximate $\Phi_{N+1}(x)$ through placement of zeros x_1, x_2, and x_3. Consequently, the Galerkin equations (C.9) are roughly satisfied because of approximate orthogonality between Φ_{N+1} and the Φ_k, $k = 1, \cdots, N$.[3] Figure C.2 depicts an equally viable extrema-collocation procedure. It is seen that extrema collocation makes $\Phi_N(x)$ nearly orthogonal to $R(x)$; the residual is obligated to switch signs where Φ_N is largest, that is, at its extrema. The residual is nearly orthogonal to $\Phi_1, \cdots, \Phi_{N-1}$ as well since it crosses the zero axis at least N times and therefore resembles Φ_{N+1}. Again, the Galerkin equations (C.9) are roughly satisfied. In fact, both zero- and extrema-collocation methods are mathematically equivalent to Galerkin's method as $N \to \infty$.

As a final remark, not using the zeros or extrema derived from the appropriate high-order basis functions runs the risk of losing numerical accuracy. If, for example, the bell-shaped function $(1 + x^2)^{-1}$ is approximated with a Tchebycheff basis set (see Appendix G), on a finite interval [-1,+1] with uniform collocation-point spacing, spurious interpolatory oscillations will occur near interval endpoints, called the Runge phenomenon [15].[4] The collocation method attempts to "mimic" the Galerkin method so that the overall numerical approximation error (that is, discretization error, $\sim \int d^s x \, |y(x) - \hat{y}(x)|$) vanishes in a mathematically well-behaved fashion with increasing N; Runge oscillations should be minimized, if not eliminated.

---

[2]The basis functions are assumed oscillatory in nature, examples of which are illustrated in Appendix G [Figs. G.1, G.2, and G.3].

[3]Orthogonality asserts that $\int dx \; \Phi_k(x)\Phi_{N+1}(x) = 0$ for $k = 1, \cdots, N$. If $R(x) \approx \Phi_{N+1}(x)$ then $\int dx \; \Phi_k(x)R(x) \approx 0$, an approximate version of (C.9).

[4]This phenomenon is not so surprising after noting that Tchebycheff polynomials oscillate relatively rapidly near interval endpoints.

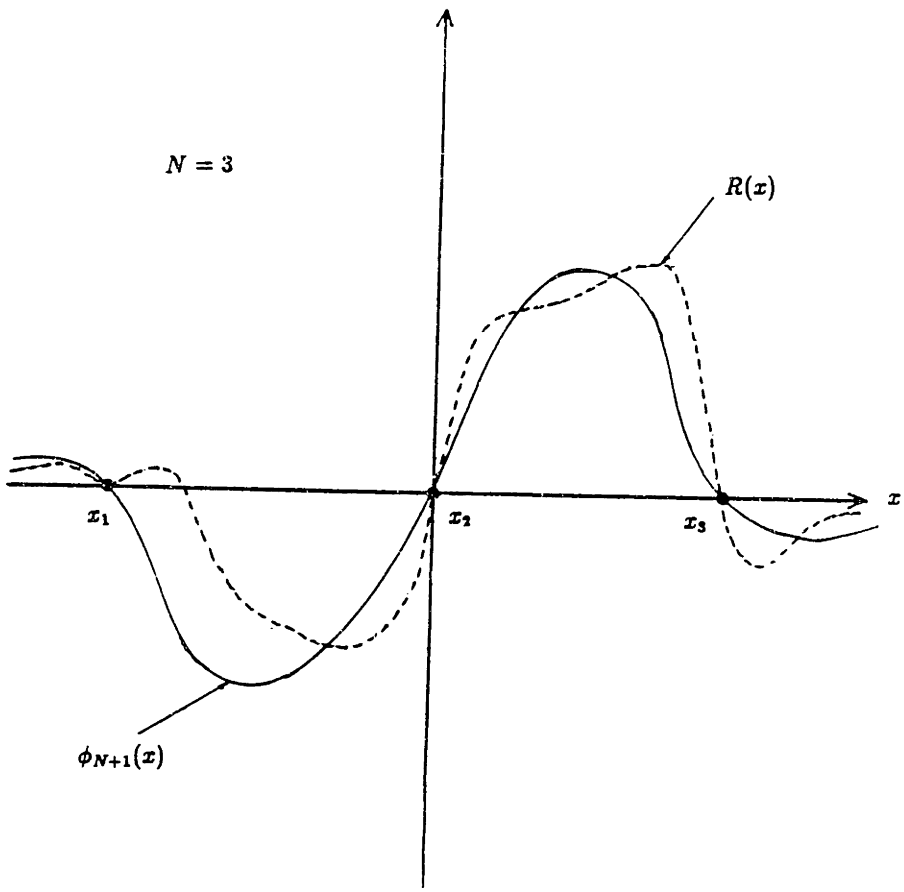

Figure C.1. Example of R and ϕ_{N+1} for zeros collocation.

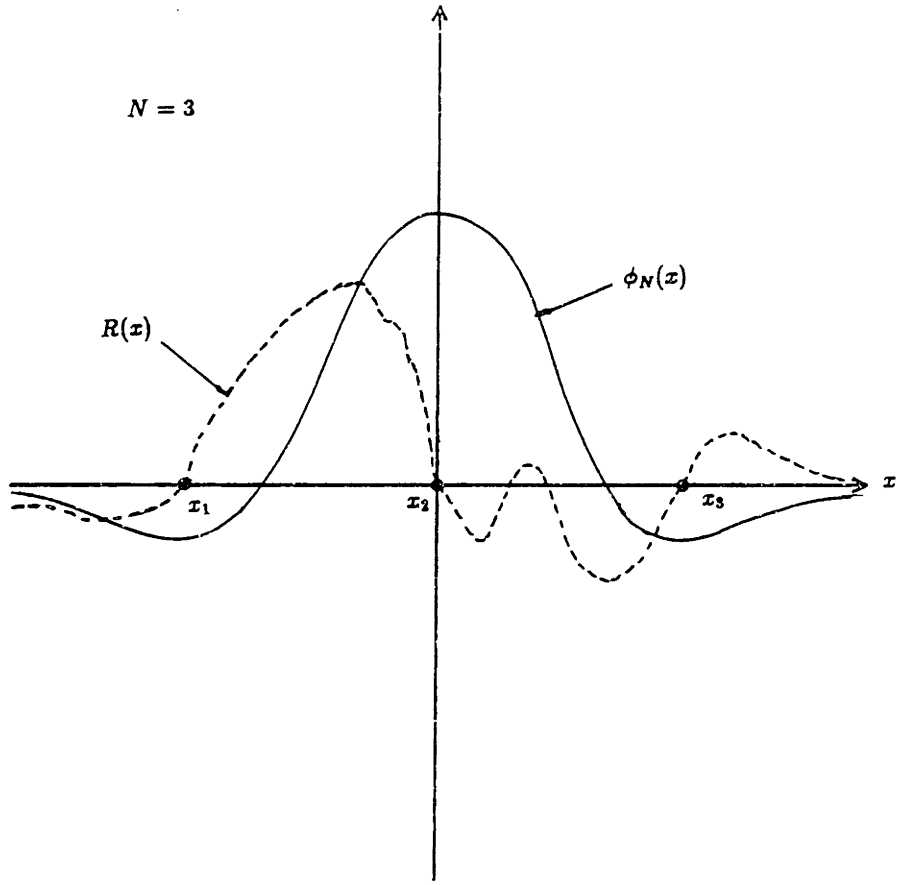

Figure C.2. Example of R and ϕ_N for extrema collocation.

C.5 Gaussian Elimination of Block-Tridiagonal Systems

The system of equations (3.14) generated from FD-spectral solution of the (x, v_x) and (z, v_ρ, v_z) problems have a block-tridiagonal structure, rewritten here,

$$\begin{pmatrix} R_2 & S_2 & & & & & & \\ Q & R_3 & S & & & & & \\ & Q & R_4 & S & & & & \\ & & \cdot & \cdot & \cdot & & & \\ & & & \cdot & \cdot & \cdot & & \\ & & & & \cdot & \cdot & \cdot & \\ & & & & & Q & R_{L-3} & S \\ & & & & & & Q & R_{L-2} & S \\ & & & & & & & Q_{L-1} & R_{L-1} \end{pmatrix} \begin{pmatrix} \alpha_2 \\ \alpha_3 \\ \alpha_4 \\ \cdot \\ \cdot \\ \cdot \\ \alpha_{L-3} \\ \alpha_{L-2} \\ \alpha_{L-1} \end{pmatrix} = \begin{pmatrix} \beta \\ 0 \\ 0 \\ \cdot \\ \cdot \\ \cdot \\ 0 \\ 0 \\ 0 \end{pmatrix}, \tag{C.11}$$

where $Q, Q_{L-1}, R_i, R_{L-1}, S$, and S_2 are square matrices and α_i and β are corresponding vectors ($i = 2, \cdots, L-1$). Equation (C.11) can be solved for the α_i through generalization of the Gaussian elimination procedure that is usually applied to systems of scalar equations [15].

The first step is forward elimination. The top block row is premultiplied by R_2^{-1} and any "block elements" directly beneath R_2 are eliminated. Elimination proceeds through matrix scaling of the top block row followed by addition of that row to lower block rows.[5] This process is repeated, starting with the leading block element of the second row down through the last block row, resulting in a block-upper-triangular system, which is mathematically

[5] Written in full, after eliminating with its top block row, (C.11) changes to:

$$\begin{pmatrix} I & R_2^{-1}S_2 & & & & \\ & R_3 - QR_2^{-1}S_2 & S & & & \\ & Q & R_4 & S & & \\ & & \cdot & \cdot & \cdot & \\ & & & \cdot & \cdot & \cdot \\ & & & & \cdot & \cdot & \cdot \end{pmatrix} \begin{pmatrix} \alpha_2 \\ \alpha_3 \\ \alpha_4 \\ \cdot \\ \cdot \\ \cdot \end{pmatrix} = \begin{pmatrix} R_2^{-1}\beta \\ -QR_2^{-1}\beta \\ 0 \\ \cdot \\ \cdot \\ \cdot \end{pmatrix}.$$

equivalent to (C.11):

$$\begin{pmatrix} I & U_2 & & & & & & \\ & I & U_3 & & & & & \\ & & I & U_4 & & & & \\ & & & \cdot & \cdot & & & \\ & & & & \cdot & \cdot & & \\ & & & & & \cdot & \cdot & \\ & & & & & I & U_{L-3} & \\ & & & & & & I & U_{L-2} \\ & & & & & & & I \end{pmatrix} \begin{pmatrix} \alpha_2 \\ \alpha_3 \\ \alpha_4 \\ \cdot \\ \cdot \\ \cdot \\ \alpha_{L-3} \\ \alpha_{L-2} \\ \alpha_{L-1} \end{pmatrix} = \begin{pmatrix} \gamma_2 \\ \gamma_3 \\ \gamma_4 \\ \cdot \\ \cdot \\ \cdot \\ \gamma_{L-3} \\ \gamma_{L-2} \\ \gamma_{L-1} \end{pmatrix}. \tag{C.12}$$

The matrices U_i, $i = 2, \cdots, L-2$ and vectors γ_i, $i = 2, \cdots, L-1$ represent the upper-diagonal and inhomogeneous block elements.

The second step in the solution procedure is back substitution. A recursion relation for the α_i immediately follows when (C.12) is written out, bottom to top:

$$\begin{aligned} &\alpha_{L-1} = \gamma_{L-1}, \\ &\alpha_{L-i} = \gamma_{L-i} - U_{L-i}\alpha_{L-i+1}, \qquad (C.13) \\ &\qquad i = 2, \cdots, L-2. \end{aligned}$$

Appendix D

Spectral and Transformation Matrices for the (x, y, v_x, v_y, v_z) Problem

D.1 Symmetry of the Spectral and Transformation Matrices

Undertaken in this appendix is further elaboration of the c symmetry of the spectral matrices, along with a proof of the r symmetry of the transformation matrix, all in context of the (x, y, v_x, v_y, v_z) problem.

With reference to the discussion in Section 4.4.3, matrices U, V, A, and B have been shown to be c symmetric. Array (D.1) conveniently illustrates their symmetry.

$$\begin{array}{c} \\ I \\ II \\ III \\ IV \end{array} \begin{array}{c} \begin{array}{cccc} ee & oe & oo & eo \end{array} \\ \begin{pmatrix} G_1 & G_2 & G_3 & G_4 \\ \pm G_1 & \mp G_2 & \mp G_3 & \pm G_4 \\ \mp G_1 & \pm G_2 & \mp G_3 & \pm G_4 \\ \mp G_1 & \mp G_2 & \mp G_3 & \pm G_4 \end{pmatrix} \end{array} . \tag{D.1}$$

Matrices G_1, G_2, G_3, and G_4 represent "generic" block elements within each c-symmetric spectral matrix. The upper sign is to be taken for U and V matrices, whereas the the lower sign should be taken for A and B matrices. Column ordering is indicated by the parities of the constituent functions $\phi_\kappa \phi_\ell$ (e=even and o=odd) and row-ordering by the collocation quadrant in

the (v_x, v_y) plane. Matrices C and T^{-1} are also c symmetric, according to Section 4.4.3. Arrays (D.2) and (D.3) depict their respective symmetries:

$$\begin{array}{c} \\ I \\ II \\ III \\ IV \end{array} \begin{array}{c} \begin{array}{cccc} ee & oe & oo & eo \end{array} \\ \begin{pmatrix} C_1 & C_2 & C_3 & C_4 \\ C_1 & C_2 & C_3 & C_4 \\ C_1 & C_2 & C_3 & C_4 \\ C_1 & C_2 & C_3 & C_4 \end{pmatrix} \end{array}, \tag{D.2}$$

$$\begin{array}{c} \\ I \\ II \\ III \\ IV \end{array} \begin{array}{c} \begin{array}{cccc} ee & oe & oo & eo \end{array} \\ \begin{pmatrix} T_1^{-1} & T_2^{-1} & T_3^{-1} & T_4^{-1} \\ T_1^{-1} & -T_2^{-1} & -T_3^{-1} & T_4^{-1} \\ T_1^{-1} & -T_2^{-1} & T_3^{-1} & -T_4^{-1} \\ T_1^{-1} & T_2^{-1} & -T_3^{-1} & -T_4^{-1} \end{pmatrix} \end{array}. \tag{D.3}$$

It was claimed in Section 4.4.3 , without proof, that the transformation matrix T is r symmetric. This can be proved by means of Gaussian elimination (see Appendix C.5), given that T^{-1} is c symmetric. Array (D.3) can be augmented with the identity block matrix,

$$\begin{pmatrix} T_1^{-1} & T_2^{-1} & T_3^{-1} & T_4^{-1} & I & O & O & O \\ T_1^{-1} & -T_2^{-1} & -T_3^{-1} & T_4^{-1} & O & I & O & O \\ T_1^{-1} & -T_2^{-1} & T_3^{-1} & -T_4^{-1} & O & O & I & O \\ T_1^{-1} & T_2^{-1} & -T_3^{-1} & -T_4^{-1} & O & O & O & I \end{pmatrix}, \tag{D.4}$$

where I is the identity matrix. The inverse of T^{-1}, that is, T, can be computed using the standard augmented-matrix technique [33], generalized for block matrices. The inverse results after a sequence of elementary block-row operations, summarized in (D.5) through (D.9) (see the discussion of Appendix C.5):

$$\begin{pmatrix} T_1^{-1} & T_2^{-1} & T_3^{-1} & T_4^{-1} & I & O & O & O \\ O & -2T_2^{-1} & -2T_3^{-1} & O & -I & I & O & O \\ O & -2T_2^{-1} & O & -2T_4^{-1} & -I & O & I & O \\ O & O & -2T_3^{-1} & -2T_4^{-1} & -I & O & O & I \end{pmatrix}, \tag{D.5}$$

$$\begin{pmatrix} T_1^{-1} & O & O & T_4^{-1} & \frac{1}{2}I & \frac{1}{2}I & O & O \\ O & -2T_2^{-1} & -2T_3^{-1} & O & -I & I & O & O \\ O & O & 2T_3^{-1} & -2T_4^{-1} & O & -I & I & O \\ O & O & -2T_3^{-1} & -2T_4^{-1} & -I & O & O & I \end{pmatrix}, \tag{D.6}$$

$$\begin{pmatrix} T_1^{-1} & O & O & T_4^{-1} & \frac{1}{2}I & \frac{1}{2}I & O & O \\ O & -2T_2^{-1} & O & -2T_4^{-1} & -I & O & I & O \\ O & O & 2T_3^{-1} & -2T_4^{-1} & O & -I & I & O \\ O & O & O & -4T_4^{-1} & -I & -I & I & I \end{pmatrix}, \tag{D.7}$$

$$\begin{pmatrix} T_1^{-1} & O & O & O & \frac{1}{4}I & \frac{1}{4}I & \frac{1}{4}I & \frac{1}{4}I \\ O & -2T_2^{-1} & O & O & -\frac{1}{2}I & \frac{1}{2}I & \frac{1}{2}I & -\frac{1}{2}I \\ O & O & 2T_3^{-1} & O & \frac{1}{2}I & -\frac{1}{2}I & \frac{1}{2}I & -\frac{1}{2}I \\ O & O & O & -4T_4^{-1} & -I & -I & I & I \end{pmatrix}, \tag{D.8}$$

and,

$$\begin{pmatrix} I & O & O & O & \frac{1}{4}T_1 & \frac{1}{4}T_1 & \frac{1}{4}T_1 & \frac{1}{4}T_1 \\ O & I & O & O & \frac{1}{4}T_2 & -\frac{1}{4}T_2 & -\frac{1}{4}T_2 & \frac{1}{4}T_2 \\ O & O & I & O & \frac{1}{4}T_3 & -\frac{1}{4}T_3 & \frac{1}{4}T_3 & -\frac{1}{4}T_3 \\ O & O & O & I & \frac{1}{4}T_4 & \frac{1}{4}T_4 & -\frac{1}{4}T_4 & -\frac{1}{4}T_4 \end{pmatrix}. \tag{D.9}$$

In the last step, (D.9), the block element identity relations $T_1T_1^{-1} = T_2T_2^{-1} = T_3T_3^{-1} = T_4T_4^{-1} = I$ have been employed. Augmented array (D.9) therefore implies that T is r symmetric with structure

$$\left(\frac{1}{4}\right)\begin{pmatrix} T_1 & T_1 & T_1 & T_1 \\ T_2 & -T_2 & -T_2 & T_2 \\ T_3 & -T_3 & T_3 & -T_3 \\ T_4 & T_4 & -T_4 & -T_4 \end{pmatrix}. \tag{D.10}$$

D.2 Numerical Evaluation of Vector Products Involving C- and R-Symmetric Matrices

Iterative solution of the (x, y, v_x, v_y, v_z) problem requires a large number of vector-matrix multiplications specified by (4.9) and (4.10). The numerical computation time for these multiplications can be greatly reduced—by a factor of four—if matrix symmetries are fully exploited.

It is evident from the preceding section that only two types of vector-matrix multiplications will be encountered in iterating (4.9) and (4.10): written symbolically, a vector product with a c-symmetric matrix,

$$\boldsymbol{Pa} = \boldsymbol{b}, \tag{D.11}$$

and a vector product with an r-symmetric matrix

$$Qc = d. \tag{D.12}$$

The $N \times N$ matrices P and Q are composed of $N/4 \times N/4$ block-matrix elements P_i and Q_i, $i = 1, \cdots, 4$, respectively, with a block-element sign pattern $s_{ij} = \pm 1$ for $i, j = 1, \cdots, 4$. Vectors a, b, c, and d are all of length N. Suppose a, b, c, and d are partitioned into $N/4$-vector elements[1]:

$$a = \begin{pmatrix} a_1 \\ a_2 \\ a_3 \\ a_4 \end{pmatrix}, b = \begin{pmatrix} b_1 \\ b_2 \\ b_3 \\ b_4 \end{pmatrix}, c = \begin{pmatrix} c_1 \\ c_2 \\ c_3 \\ c_4 \end{pmatrix}, \text{ and } d = \begin{pmatrix} d_1 \\ d_2 \\ d_3 \\ d_4 \end{pmatrix}. \tag{D.13}$$

The vector-matrix products (D.11) and (D.12) can be put into the form,

$$\sum_{j=1}^{4} s_{ij}(P_j a_j) = b_i \tag{D.14}$$

and

$$Q_i \left(\sum_{j=1}^{4} s_{ij} c_j \right) = d_i \tag{D.15}$$

for $i = 1, \cdots, 4$. The calculations would commence by evaluating and storing the quantities within parentheses above. Appropriate matrix additions and subtractions in the case of (D.14), or matrix multiplications in the case of (D.15), would then be carried out. In terms of computational effort (number of scalar multiplications) this procedure results in an order $N^2/4$ process. "Brute force" evaluation of (D.11) or (D.12) is an order N^2 process, and thus a factor of four is gained in execution rate. Observe also that only four block matrices P_i (or Q_i), not their large original matrix P (or Q), need be stored in computer memory.

[1]By assumption, N is divisible by four. This also follows from the fact that the vectors a, b, c, and d multiply c- and r-symmetric matrices that, by definition, have four-fold internal symmetry [see (D.1) through (D.3) and (D.10), for example].

Appendix E

Scattering Probability-Rate Functions

Appendix E contains derivations of physically realistic scattering probability rates in terms of velocity variables. The derivations will start with k-dependent scattering-probability-rate functions obtained from the literature.[1] The primary intent here is not to describe physical scattering processes in painstaking detail (nonparabolicity factors, screening effects, Bloch-function overlap integrals, and the like [6–10], but to make reasonable assumptions and approximations that simplify the mathematics while the same time preserving overall mathematical behavior.

Throughout this appendix, it is understood that the assumptions of Section 1.1.3 are all in effect.

E.1 Transformation to Velocity Space

As is standard practice, semiconductor scattering rates are formulated in k-space variables. Carriers (electrons) are described through introduction of a k-space distribution function $f^{(k)}(r, k, t)$, an occupation probability that when multiplied by the density of states (including spin) per unit k volume

[1] These probability-rate equations have been taken from Conwell's monograph *High-Field Transport in Semiconductors* [8] and Jacoboni and Reggiani's review article *The Monte-Carlo Method for Solution of Charge Transport in Semiconductors with Applications to Covalent Materials* [9]. These two works should also serve as good starting references for a physical explanation of semiconductor scattering processes.

per unit $\boldsymbol{r}$ volume, $2/(2\pi)^3$, and the phase-space volume element $d^3r d^3k$ gives the number of carriers in $(\boldsymbol{r}, \boldsymbol{r}+d\boldsymbol{r})$ with wavevector within $(\boldsymbol{k}, \boldsymbol{k}+d\boldsymbol{k})$ at time t. The $\boldsymbol{k}$-space version of BTE (1.2) (for a spherical, parabolic band) can be shown to be [6]

$$\frac{\partial f^{(k)}}{\partial t} = -\frac{\hbar}{m^*}\boldsymbol{k}\cdot\nabla_r f^{(k)} - \frac{q}{\hbar}\boldsymbol{E}\cdot\nabla_k f^{(k)} + C^{(k)} f^{(k)}, \tag{E.1}$$

where the collision operator $C^{(k)}$ affects only the $\boldsymbol{k}$ variables according to the scattering formula (nondegenerate statistics, time and space variables suppressed)

$$C^{(k)} f^{(k)} = \frac{V}{(2\pi)^3}\int d^3k' \left[f^{(k)}(\boldsymbol{k}')S^{(k)}(\boldsymbol{k}', \boldsymbol{k}) - f^{(k)}(\boldsymbol{k})S^{(k)}(\boldsymbol{k}, \boldsymbol{k}')\right] \tag{E.2}$$

[compare (E.1), (E.2) and (1.2) through (1.4)]. Both in- and out-scattering contributions have been written explicitly in (E.2), and the appearance of the (single-spin) density-of-states factor $V/(2\pi)^3$ follows from the spin-conservation assumption (see Section 1.1.3). Here, V is the quantization volume chosen small enough that $f^{(k)}$ is nearly constant within V. It is important to understand that the $\boldsymbol{k}$-space scattering rate $S^{(k)}(\boldsymbol{k}, \boldsymbol{k}')$ is a probability per unit time for transitions from $\boldsymbol{k}$ to $\boldsymbol{k}'$, unlike the velocity-space scattering rate $S(\boldsymbol{v}, \boldsymbol{v}')$, which is a probability per unit time per unit velocity volume (see Section 1.1.1).

Transformation to velocity variables is achieved through setting $\hbar\boldsymbol{k} = m^*\boldsymbol{v}$ and $\hbar\boldsymbol{k}' = m^*\boldsymbol{v}'$, and using the associated differential relations $d^3k = (m^*/\hbar)^3 d^3v$ and $d^3k' = (m^*/\hbar)^3 d^3v'$. Transformation of (E.1) leads directly to BTE (1.2), after changing $C^{(k)}$ to C, the collision operator in velocity space, and $f^{(k)}$ to f, the occupancy probability per unit $\boldsymbol{r}$ volume per unit $\boldsymbol{v}$ volume. The latter transformation involves just multiplicative factors: $f(\boldsymbol{r}, \boldsymbol{v}, t) = f^{(k)}(\boldsymbol{r}, m^*\boldsymbol{v}/\hbar, t) \times 2/(2\pi)^3 \times (m^*/\hbar)^3$. Similar transformation of (E.2) ends with

$$\begin{aligned} Cf = \int d^3v' \Bigg[& f(\boldsymbol{v}')\frac{V}{(2\pi)^3}\left(\frac{m^*}{\hbar}\right)^3 S^{(k)}\left(\frac{m^*}{\hbar}\boldsymbol{v}', \frac{m^*}{\hbar}\boldsymbol{v}\right) \\ & - f(\boldsymbol{v})\frac{V}{(2\pi)^3}\left(\frac{m^*}{\hbar}\right)^3 S^{(k)}\left(\frac{m^*}{\hbar}\boldsymbol{v}, \frac{m^*}{\hbar}\boldsymbol{v}'\right)\Bigg]. \end{aligned} \tag{E.3}$$

Comparison of velocity-space Eqs. (1.3) and (1.4) with (E.3) above establishes the transformation rule

$$S(\boldsymbol{v},\boldsymbol{v}') = \frac{V}{(2\pi)^3}\left(\frac{m^*}{\hbar}\right)^3 S^{(k)}\left(\frac{m^*}{\hbar}\boldsymbol{v},\frac{m^*}{\hbar}\boldsymbol{v}'\right). \tag{E.4}$$

The quantity $S(\boldsymbol{v},\boldsymbol{v}')d^3v'$ can be interpreted as a probability rate for transitions from $\boldsymbol{v}$ to within $(\boldsymbol{v}',\boldsymbol{v}'+d\boldsymbol{v}')$, as originally stated in Section 1.1.1.

E.2 Deformation-Potential Acoustic Scattering

The combined absorption and emission probability rate for deformation-potential scattering by acoustic phonons is [10]

$$S_a^{(k)}(\boldsymbol{k},\boldsymbol{k}') = \frac{2\pi k_B T \Xi_a^2}{\rho u^2 \hbar V}\delta(\varepsilon'-\varepsilon). \tag{E.5}$$

where ε and ε' are the initial and final kinetic energies, respectively, which for spherical, parabolic bands are simply $\varepsilon = (\hbar k)^2/2m^*$ and $\varepsilon' = (\hbar k')^2/2m^*$. Quantization volume is given by V, crystal density by ρ, speed of sound by u, and acoustic-deformation-potential interaction constant by Ξ_a. In establishing (E.5) collisions are treated as elastic ($\varepsilon \approx \varepsilon'$), carrier screening has been neglected, and the cell-periodic Bloch-function overlap integral has been set to unity (see reference [10]). Equipartition is also assumed to hold; thus, typical carrier energy ($\sim k_B T$) is much larger than the phonon energy $\hbar\omega_a(\boldsymbol{q})$ near $q = 0$.

Transformation of (E.5) to velocity variables is achieved by means of (E.4), yielding

$$S_a(\boldsymbol{v},\boldsymbol{v}') = \frac{(m^*)^3 k_B T \Xi_a^2}{(2\pi)^2 \rho u^2 \hbar^4}\delta(\varepsilon'-\varepsilon), \tag{E.6}$$

where kinetic energies are now expressed as $\varepsilon = m^* v^2/2$ and $\varepsilon' = m^*(v')^2/2$.

The total scattering probability rate $\lambda_a(\varepsilon)$ is calculated upon integrating (E.6) over all $\boldsymbol{v}'$ [as in Eq. (1.4)]. Integration is facilitated using spherical-energy coordinates $(\varepsilon',\phi',\theta')$ with velocity volume element $d^3v' = 2^{1/2}(m^*)^{-3/2}$

$(\varepsilon')^{1/2}\sin\theta' d\varepsilon' d\phi' d\theta'$:

$$\begin{aligned}\lambda_a(\varepsilon) &= \frac{(m^*)^{3/2}k_BT\Xi_a^2}{2\sqrt{2}\pi^2\rho u^2\hbar^4}\int_0^\pi\int_{-\pi}^{\pi}\int_0^\infty d\varepsilon' d\phi' d\theta'\ \sqrt{\varepsilon'}\sin\theta'\delta(\varepsilon'-\varepsilon)\\ &= \frac{\sqrt{2}(m^*)^{3/2}k_BT\Xi_a^2}{\pi\rho u^2\hbar^4}\sqrt{\varepsilon}. \qquad \text{(E.7)}\end{aligned}$$

When the distribution function possesses cylindrical velocity symmetry, which is the case for the (z, v_ρ, v_z) problem, the in-scattering component of the BTE collision term can be to a certain extent simplified. After suppression of space and time variables, the in-scattering component

$$\begin{aligned}\int d^3v'\ f(v'_\rho, v'_z)S_a(\boldsymbol{v}', \boldsymbol{v}) &= \frac{(m^*)^{3/2}k_BT\Xi_a^2}{2\sqrt{2}\pi^2\rho u^2\hbar^4}\\ &\times\int_0^\pi\int_{-\pi}^{\pi}\int_0^\infty d\varepsilon' d\phi' d\theta'\ \sqrt{\varepsilon'}\sin\theta' f\left(\sqrt{\frac{2\varepsilon'}{m^*}}\sin\theta', \sqrt{\frac{2\varepsilon'}{m^*}}\cos\theta'\right)\delta(\varepsilon'-\varepsilon)\\ &= S_a\int_{-v}^{v} d\xi\ f(\sqrt{v^2-\xi^2}, \xi), \qquad \text{(E.8)}\end{aligned}$$

with the scattering factor

$$S_a = \frac{(m^*)^2k_BT\Xi_a^2}{2\pi\rho u^2\hbar^4}. \qquad \text{(E.9)}$$

The first equality in (E.8) follows by transformation to spherical-energy coordinates; the last equality follows from integration over ε' and ϕ' and subsequent transformation of θ' according to $\xi = (2\varepsilon/m^*)^{1/2}\cos\theta'$.

A similar situation arises in connection with the (x, y, v_x, v_y, v_z) problem. In this case the in-scattering component

$$\begin{aligned}\int d^3v'\ f(v'_x, v'_y, |v'_z|)S_a(\boldsymbol{v}', \boldsymbol{v}) &= \frac{(m^*)^{3/2}k_BT\Xi_a^2}{\sqrt{2}\pi^2\rho u^2\hbar^4}\int_0^{\pi/2}\int_{-\pi}^{\pi}\int_0^\infty d\varepsilon' d\phi' d\theta'\\ &\times\sqrt{\varepsilon'}\sin\theta' f\left(\sqrt{\frac{2\varepsilon'}{m^*}}\sin\theta'\cos\phi', \sqrt{\frac{2\varepsilon'}{m^*}}\sin\theta'\sin\phi', \sqrt{\frac{2\varepsilon'}{m^*}}\cos\theta'\right)\delta(\varepsilon'-\varepsilon)\\ &= \int_{-v}^{v}\int_{-(v^2-\eta^2)^{1/2}}^{(v^2-\eta^2)^{1/2}} d\xi d\eta\ S_a(\xi, \eta, v)f(\xi, \eta, \sqrt{v^2-\xi^2-\eta^2}), \qquad \text{(E.10)}\end{aligned}$$

with the scattering factor

$$S_a(\xi,\eta,v) = \left[\frac{(m^*)^2 k_B T \Xi_a^2}{2\pi^2 \rho u^2 \hbar^4}\right] \frac{1}{\sqrt{v^2-\xi^2-\eta^2}}. \tag{E.11}$$

These results are found through transformation to spherical-energy coordinates, integration over ε', and then final transformation to rectangular coordinates.[2] This last transformation is simply $\xi(\theta',\phi') = (2\varepsilon/m^*)^{1/2}\sin\theta'\cos\phi'$ and $\eta(\theta',\phi') = (2\varepsilon/m^*)^{1/2}\sin\theta'\sin\phi'$ with Jacobian determinant $\partial(\theta',\phi')/\partial(\xi,\eta)$ $= (m^*/2)^{1/2}\varepsilon^{-1/2}(\sin\theta')^{-1}(v^2-\xi^2-\eta^2)^{-1/2}$.

E.3 Nonpolar Optic Scattering

Nonpolar optic phonon scattering is characterized by the probability rate [10]

$$S_o^{(k)}(\boldsymbol{k},\boldsymbol{k}') = \frac{\pi\Xi_o^2}{\rho\omega_o V}\begin{cases} N_o\delta(\varepsilon'-\varepsilon-\hbar\omega_o) & \text{(absorption)} \\ (N_o+1)\delta(\varepsilon'-\varepsilon+\hbar\omega_o) & \text{(emission).}\end{cases} \tag{E.12}$$

Identical to those in (E.5), energies ε and ε' are functions of wavevector magnitude. The optic phonon frequency, nonpolar-deformation-potential interaction constant, and Bose-Einstein occupancy factor for optic-phonon modes are denoted ω_o, Ξ_o, and N_o, respectively. The Bose-Einstein occupancy factor is evaluated at a fixed phonon energy $\hbar\omega_o$:

$$N_o = \frac{1}{\exp\left(\frac{\hbar\omega_o}{k_B T}\right)-1}, \tag{E.13}$$

which is consistent with the assumption that there is no dispersion for optical phonons $[\hbar\omega_o(q) = \hbar\omega_o]$. Most of the other assumptions made in the previous section are also valid here, although in this section collisions are inelastic $(\varepsilon' = \varepsilon \pm \hbar\omega_o$ where $k_B T \sim \hbar\omega_o)$.

Transformation of (E.12) to velocity variables works along the same line as that for the deformation-potential acoustic scattering. With ε and ε'

[2]Placement of final results in rectangular coordinates, and earlier, in cylindrical coordinates [(E.8)], is done for reasons of numerical accuracy; the distribution function is presumed, on physical grounds, to be "well-matched" to a uniform discretization in these respective coordinate systems.

functions of velocity magnitude, the velocity-dependent scattering probability rate becomes

$$S_o(v,v') = \frac{(m^*)^3\Xi_o^2}{8\pi^2\rho\omega_o\hbar^3}\begin{cases} N_o\delta(\varepsilon'-\varepsilon-\hbar\omega_o) & \text{(absorption)} \\ (N_o+1)\delta(\varepsilon'-\varepsilon+\hbar\omega_o) & \text{(emission).}\end{cases} \tag{E.14}$$

Integration of (E.15) in a manner similar to (E.7) yields

$$\lambda_o(\varepsilon) = \frac{(m^*)^{3/2}\Xi_o^2}{\sqrt{2}\pi\rho\omega_o\hbar^3}\begin{cases} N_o\sqrt{\varepsilon+\hbar\omega_o} & \text{(absorption)} \\ (N_o+1)\sqrt{\varepsilon-\hbar\omega_o}\;u(\varepsilon-\hbar\omega_o) & \text{(emission)}\end{cases} \tag{E.15}$$

for the total scattering probability rate due to nonpolar optic phonons. The unit step function $u(\varepsilon-\hbar\omega_o)$ ensures that phonon emission does not occur for carrier energies less than the optic-phonon energy.

Lastly, cylindrical and mirror symmetric in-scattering components can be written immediately, after noting the mathematical manipulations in (E.8) and (E.10) and replacing ε by the appropriate quantity $\varepsilon \pm \hbar\omega_o$. Unit step functions need also to be introduced to eliminate unphysical imaginary radicals. The results are

$$\int d^3v'\; f(v'_\rho, v'_z)S(v',v)$$
$$= \begin{cases} S_o^-(v)\displaystyle\int_{-(v^2-v_o^2)^{1/2}}^{(v^2-v_o^2)^{1/2}} d\xi\; f(\sqrt{v^2-v_o^2-\xi^2},\xi) & \text{(absorption)} \\ S_o^+\displaystyle\int_{-(v^2+v_o^2)^{1/2}}^{(v^2+v_o^2)^{1/2}} d\xi\; f(\sqrt{v^2+v_o^2-\xi^2},\xi) & \text{(emission)}\end{cases} \tag{E.16}$$

and

$$\int d^3v'\; f(v'_x, v'_y, |v'_z|)S(v',v)$$
$$= \begin{cases} \displaystyle\int_{-(v^2-v_o^2)^{1/2}}^{(v^2-v_o^2)^{1/2}}\int_{-(v^2-v_o^2-\eta^2)^{1/2}}^{(v^2-v_o^2-\eta^2)^{1/2}} d\xi d\eta\; S_o^-(\xi,\eta,v) \\ \times f(\xi,\eta,\sqrt{v^2-v_o^2-\xi^2-\eta^2}) & \text{(absorption)} \\ \displaystyle\int_{-(v^2+v_o^2)^{1/2}}^{(v^2+v_o^2)^{1/2}}\int_{-(v^2+v_o^2-\eta^2)^{1/2}}^{-(v^2+v_o^2-\eta^2)^{1/2}} d\xi d\eta\; S_o^+(\xi,\eta,v) \\ \times f(\xi,\eta,\sqrt{v^2+v_o^2-\xi^2-\eta^2}) & \text{(emission)}\end{cases} \tag{E.17}$$

with the scattering factors

$$S_o^-(v) = \frac{(m^*)^2 \Xi_o^2 N_o}{4\pi\rho\omega_o\hbar^3}\, u(v - v_o), \tag{E.18}$$

$$S_o^+ = \frac{(m^*)^2 \Xi_o^2 (N_o + 1)}{4\pi\rho\omega_o\hbar^3}, \tag{E.19}$$

$$S_o^-(\xi, \eta, v) = \left[\frac{(m^*)^2 \Xi_o^2 N_o}{4\pi^2\rho\omega_o\hbar^3}\right] \frac{u(v - v_o)}{\sqrt{v^2 - v_o^2 - \xi^2 - \eta^2}}, \tag{E.20}$$

and

$$S_o^+(\xi, \eta, v) = \left[\frac{(m^*)^2 \Xi_o^2 (N_o + 1)}{4\pi^2\rho\omega_o\hbar^3}\right] \frac{1}{\sqrt{v^2 + v_o^2 - \xi^2 - \eta^2}}. \tag{E.21}$$

In all foregoing expressions, the parameter $v_o = (2\hbar\omega_o/m^*)^{1/2}$ is the carrier velocity corresponding to the optic-phonon energy.

E.4 Polar Optic Scattering

Scattering due to polar optic phonons obeys the probability-rate equation [10]

$$S_{po}^{(k)}(\boldsymbol{k}, \boldsymbol{k}') = \frac{\pi q^2 \omega_\ell (\epsilon_\infty^{-1} - \epsilon_o^{-1})}{V|\boldsymbol{k} - \boldsymbol{k}'|^2} \begin{cases} N_\ell \delta(\varepsilon' - \varepsilon - \hbar\omega_\ell) & \text{(absorption)} \\ (N_\ell + 1)\delta(\varepsilon' - \varepsilon + \hbar\omega_\ell) & \text{(emission).} \end{cases} \tag{E.22}$$

Equation (E.22) is the analog of (E.12) for nonpolar phonon scattering, and is predicated upon similar assumptions (spherical, parabolic bands; unity overlap integral; zero phonon dispersion; and so forth). In the above expression ω_ℓ is the longitudinal optic phonon frequency, ϵ_∞ and ϵ_o are the high-frequency and static dielectric constants, respectively, and N_ℓ is the Bose-Einstein occupancy factor for longitudinal phonon modes at energy $\hbar\omega_\ell$:

$$N_\ell = \frac{1}{\exp\left(\frac{\hbar\omega_\ell}{k_B T}\right) - 1}. \tag{E.23}$$

In velocity variables, with $\varepsilon = m^* v^2/2$ and $\varepsilon' = m^*(v')^2/2$, (E.27) changes

to

$$S_{po}(\boldsymbol{v},\boldsymbol{v}') = \frac{m^* q^2 \omega_\ell (\epsilon_\infty^{-1} - \epsilon_o^{-1})}{8\pi^2 \hbar |\boldsymbol{v}-\boldsymbol{v}'|^2} \begin{cases} N_\ell \delta(\varepsilon' - \varepsilon - \hbar\omega_\ell) & \text{(absorption)} \\ (N_\ell + 1)\delta(\varepsilon' - \varepsilon + \hbar\omega_\ell) & \text{(emission).} \end{cases} \tag{E.24}$$

Integration of (E.24) for the total scattering probability rate λ_{po} is slightly more complicated than in the previous cases owing to the appearance of the scattering anisotropy term $|\boldsymbol{v}-\boldsymbol{v}'|^2$. It is clear from the definition (1.4) and Eq. (E.24) that λ_{po} will be a function of ε, or equivalently, v. Therefore, it is permitted to choose $\boldsymbol{v}$ parallel to the z axis and pointing in the same direction as $\hat{\boldsymbol{e}}_z$. In spherical-energy coordinates, application of the law of cosines implies $|\boldsymbol{v}-\boldsymbol{v}'|^2 = 2\varepsilon/m^* + 2\varepsilon'/m^* - 2(2\varepsilon/m^*)^{1/2}(2\varepsilon'/m^*)^{1/2}\cos\theta'$, which means

$$\lambda_{po}(\varepsilon) = \frac{(m^*)^{1/2} q^2 \omega_\ell (\epsilon_\infty^{-1} - \epsilon_o^{-1})}{8\sqrt{2}\pi^2\hbar} \int_0^\pi \int_{-\pi}^\pi \int_0^\infty d\varepsilon' d\phi' d\theta' \frac{\sqrt{\varepsilon'}\sin\theta'}{\varepsilon + \varepsilon' - 2\sqrt{\varepsilon}\sqrt{\varepsilon'}\cos\theta'}$$
$$\times \begin{cases} N_\ell \delta(\varepsilon' - \varepsilon - \hbar\omega_\ell) & \text{(absorption)} \\ (N_\ell + 1)\delta(\varepsilon' - \varepsilon + \hbar\omega_\ell) & \text{(emission).} \end{cases} \tag{E.25}$$

The integration over ε' and ϕ' presents no problem, and a subsequent change of variables, $\xi = (\varepsilon \pm \hbar\omega_\ell)^{1/2}\cos\theta'$ (upper sign for absorption, lower sign for emission), converts (E.25) to

$$\lambda_{po}(\varepsilon) = \frac{(m^*)^{1/2} q^2 \omega_\ell (\epsilon_\infty^{-1} - \epsilon_o^{-1})}{4\sqrt{2}\pi\hbar}$$
$$\times \begin{cases} N_\ell \displaystyle\int_{-(\varepsilon+\hbar\omega_\ell)^{1/2}}^{(\varepsilon+\hbar\omega_\ell)^{1/2}} d\xi \, [2\varepsilon - 2\sqrt{\varepsilon}\xi + \hbar\omega_\ell]^{-1} & \text{(absorption)} \\ (N_\ell + 1) \displaystyle\int_{-(\varepsilon-\hbar\omega_\ell)^{1/2}}^{(\varepsilon-\hbar\omega_\ell)^{1/2}} d\xi \, [2\varepsilon - 2\sqrt{\varepsilon}\xi - \hbar\omega_\ell]^{-1} \, u(\varepsilon - \hbar\omega_\ell) & \text{(emission).} \end{cases} \tag{E.26}$$

Integrals in (E.26) are readily evaluated, giving the final result[3]

$$\lambda_{po}(\varepsilon) = \frac{(m^*)^{1/2} q^2 \omega_\ell (\epsilon_\infty^{-1} - \epsilon_o^{-1})}{4\sqrt{2}\pi\hbar\sqrt{\varepsilon}} \times \begin{cases} N_\ell \ln \left| \dfrac{\sqrt{\varepsilon}+\sqrt{\varepsilon+\hbar\omega_\ell}}{\sqrt{\varepsilon}-\sqrt{\varepsilon+\hbar\omega_\ell}} \right| & \text{(absorption)} \\ (N_\ell+1) \ln \left| \dfrac{\sqrt{\varepsilon}+\sqrt{\varepsilon-\hbar\omega_\ell}}{\sqrt{\varepsilon}-\sqrt{\varepsilon-\hbar\omega_\ell}} \right| u(\varepsilon-\hbar\omega_\ell) & \text{(emission).} \end{cases} \tag{E.27}$$

The (z, v_ρ, v_z) problem requires that the in-scattering rate be put in cylindrical coordinates. This component is readily calculated by resorting to spherical-energy coordinates, where $|\boldsymbol{v}' - \boldsymbol{v}| = v^2 + (v')^2 - 2vv'[\cos\theta\cos\theta' + \sin\theta\sin\theta'\cos(\phi-\phi')]$, and integrating first over ε'. Integration over ϕ' is next carried out using the fact that $\int_0^{2\pi} d\xi\,(a+b\cos\xi)^{-1} = 2\pi(a^2-b^2)^{-1/2}$. The final result is obtained after the change of variables $\xi = (2/m^*)^{1/2}(\varepsilon \mp \hbar\omega_\ell)^{1/2}\cos\theta'$ (upper sign for absorption, lower sign for emission) and $v_z = (2\varepsilon/m^*)^{1/2}\cos\theta$:

$$\int d^3v'\; f(v'_\rho, v'_z) S_{po}(\boldsymbol{v}', \boldsymbol{v}) = \begin{cases} \displaystyle\int_{-(v^2-v_\ell^2)^{1/2}}^{(v^2-v_\ell^2)^{1/2}} d\xi\; f(\sqrt{v^2-v_\ell^2-\xi^2}, \xi) S_{po}^-(\xi, v) & \text{(absorption)} \\ \displaystyle\int_{-(v^2+v_\ell^2)^{1/2}}^{(v^2+v_\ell^2)^{1/2}} d\xi\; f(\sqrt{v^2+v_\ell^2-\xi^2}, \xi) S_{po}^+(\xi, v) & \text{(emission),} \end{cases} \tag{E.28}$$

with the scattering factors

$$S_{po}^-(\xi, v) = \frac{q^2\omega_\ell(\epsilon_\infty^{-1} - \epsilon_o^{-1}) N_\ell}{4\pi\hbar} \times \frac{u(v - v_\ell)}{[(2v^2 - v_\ell^2 - 2v_z\xi)^2 - 4(v^2 - v_z^2)(v^2 - v_\ell^2 - \xi^2)]^{1/2}} \tag{E.29}$$

and

$$S_{po}^+(\xi, v) = \frac{q^2\omega_\ell(\epsilon_\infty^{-1} - \epsilon_o^{-1})(N_\ell + 1)}{4\pi\hbar} \times \frac{1}{[(2v^2 + v_\ell^2 - 2v_z\xi)^2 - 4(v^2 - v_z^2)(v^2 + v_\ell^2 - \xi^2)]^{1/2}} \tag{E.30}$$

[3] In deriving (E.27) use has been made of relations like $2\varepsilon \pm \hbar\omega_\ell \pm 2\sqrt{\varepsilon}\sqrt{\varepsilon \pm \hbar\omega_\ell} = (\sqrt{\varepsilon} \pm \sqrt{\varepsilon \pm \hbar\omega_\ell})^2$.

In all the above $v_\ell = (2\hbar\omega_\ell/m^*)^{1/2}$ is the carrier velocity corresponding to the longitudinal-optic-phonon energy. Details of the mathematics involved in obtaining these expressions, (E.28) through (E.30), are in large part identical to those earlier for (E.8), (E.9), (E.16), (E.18), and (E.19). The only major difference here is inclusion of a scattering anisotropy term.

Appendix F

Analytical Solution of the Constant-Field, Ballistic (x, v_x) Problem

The constant-field, ballistic (x, v_x) problem is a linear, first-order partial differential equation for $f(x, v_x)$:

$$v_x \frac{\partial f}{\partial x} + \frac{qE_x}{m^*} \frac{\partial f}{\partial v_x} = 0, \tag{F.1}$$

with boundary conditions

$$f(0, v_x) = f_1(v_x) \quad v_x > 0. \tag{F.2}$$

and

$$f(0, v_x) = f_2(v_x) \quad v_x < 0. \tag{F.3}$$

For now it is presumed that $qE_x > 0$, a positive constant, and that f_1 and f_2 are arbitrary functions.

An exact solution to (F.1) subject to boundary conditions (F.2) and (F.3) can be obtained using the well-known method of characteristics [34]. The strategy is to find a transformation that converts (F.1) into an ordinary differential equation and (F.2) and (F.3) into a relatively simple initial condition. Consider the general transformation $x = x(\sigma, \tau)$, $v_x = v_x(\sigma, \tau)$; application of the chain rule results in a differential equation

$$\frac{df}{d\sigma} = \frac{\partial x}{\partial \sigma} \frac{\partial f}{\partial x} + \frac{\partial v_x}{\partial \sigma} \frac{\partial f}{\partial v_x} = 0, \tag{F.4}$$

which is equivalent to (F.1) if the characteristic equations,

$$\frac{\partial x}{\partial \sigma} = v_x \quad \text{and} \quad \frac{\partial v_x}{\partial \sigma} = \frac{qE_x}{m^*}, \tag{F.5}$$

are obeyed. Characteristic equations (F.5) can be partially integrated to give specific transformation equations:

$$\begin{aligned} x(\sigma,\tau) &= \frac{qE_x}{2m^*}\sigma^2 + c_1(\tau)\sigma + c_2(\tau), \\ v_x(\sigma,\tau) &= \frac{qE_x}{m^*}\sigma + c_1(\tau). \end{aligned} \tag{F.6}$$

The independent variable τ behaves as a parameter, on which integration constants c_1 and c_2 depend.

The proper transformation has been found, (F.6). The next step is to evaluate the integration constants; boundary conditions (F.2) and (F.3) serve as a guide. Figure F.1 depicts the strip domain (regions I and II) over which (F.1) is to be solved. An especially convenient transformation requirement is that the boundary condition domain BC , corresponding to (F.2), should map onto $B'C'$, as shown in Fig. F.2. Hence, $x(0,\tau) = 0$, which implies $c_2(\tau) = 0$; and $x = 0$, $v_x > 0$ has to map onto $\sigma = 0$, $\tau > 0$, which is certainly true if $c_1(\tau) = qE_x\tau/m^*$.[1] A transformation for region I is therefore defined:

$$\left.\begin{aligned} x(\sigma,\tau) &= \tfrac{qE_x}{2m^*}(\sigma^2 + 2\tau\sigma) \\ v_x(\sigma,\tau) &= \tfrac{qE_x}{m^*}(\sigma + \tau) \end{aligned}\right\} \text{ region I.} \tag{F.7}$$

It is easily checked that transformation (F.7) maps region I of the (x, v_x) domain according to Figs. F.1 and F.2. The remaining portion of the (x, v_x) dom region II, maps onto the (σ, τ) domain under the transformation

$$\left.\begin{aligned} x(\sigma,\tau) &= \tfrac{qE_x}{2m^*}(\sigma^2 + 2\tau\sigma) + L_x \\ v_x(\sigma,\tau) &= \tfrac{qE_x}{m^*}(\sigma + \tau) \end{aligned}\right\} \text{ region II,} \tag{F.8}$$

(as is also depicted in Figs. F.1 and F.2). The above transformation has been obtained in a manner similar to that used for (F.7). The transformation

[1] This choice for c_1 is one of the simplest, but is by no means the only one that meets the transformation requirements.

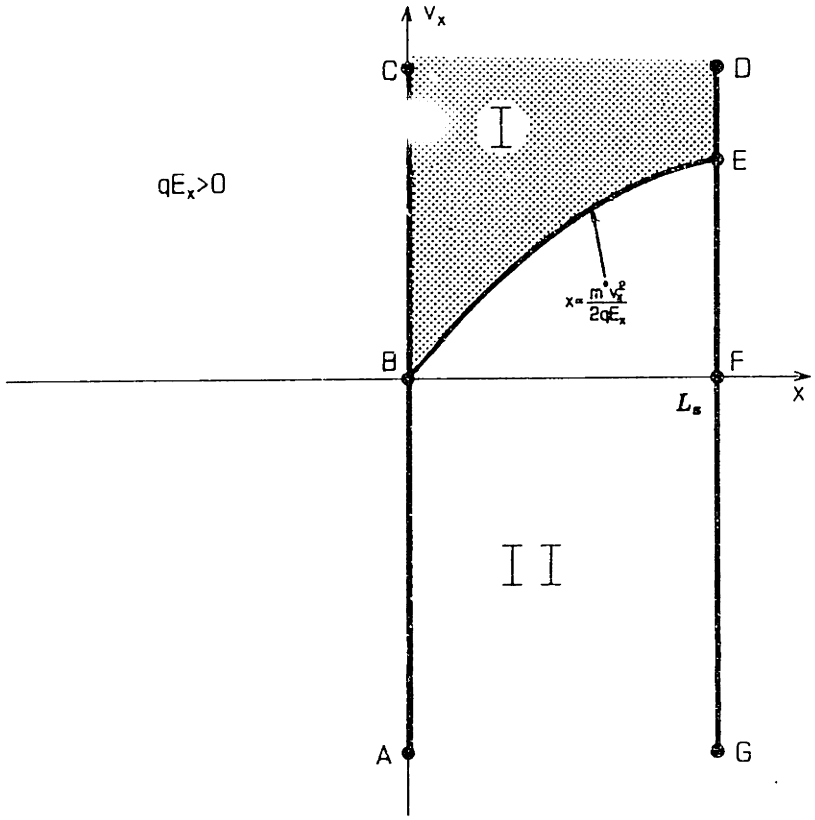

Figure F.1. Region I and II domains for Eq. (F.1).

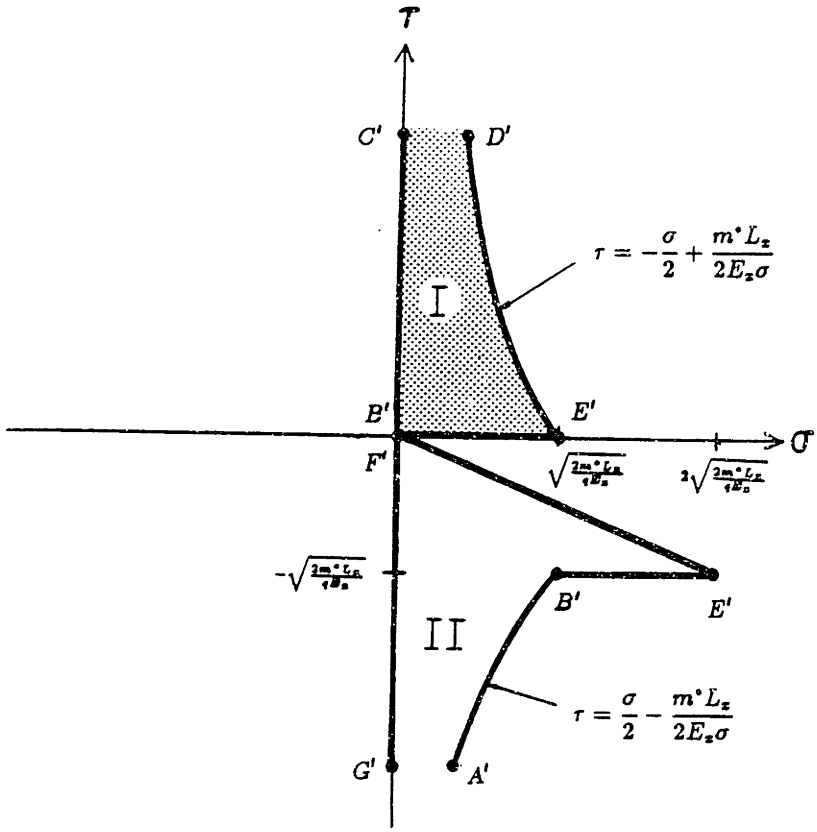

Figure F.2. Region I and II domains, transformed according to characteristic equations (F.5).

requirement is that the boundary condition domain FG, corresponding to (F.3), should map onto $F'G'$. This means $x(0,\tau) = L_x$, and that $x = L_x$, $v_x < 0$ maps onto $\sigma = 0$, $\tau < 0$. These requirements are met if $c_1(\tau) = qE_x\tau/m^*$ and $c_2(\tau) = L_x$, based on (F.6).

Inverse transformations for regions I and II are derivable from (F.7) and (F.8), and can be written[2]

$$\left.\begin{aligned} \sigma(x,v_x) &= \frac{m^*}{qE_x}\left(v_x - \sqrt{v_x^2 - \frac{2qE_x}{m^*}x}\right) \\ \tau(x,v_x) &= \frac{m^*}{qE_x}\sqrt{v_x^2 - \frac{2qE_x}{m^*}x} \end{aligned}\right\} \text{region I,} \tag{F.9}$$

and

$$\left.\begin{aligned} \sigma(x,v_x) &= \frac{m^*}{qE_x}\left[v_x + \sqrt{v_x^2 + \frac{2qE_x}{m^*}(L_x - x)}\right] \\ \tau(x,v_x) &= -\frac{m^*}{qE_x}\sqrt{v_x^2 + \frac{2qE_x}{m^*}(L_x - x)} \end{aligned}\right\} \text{region II.} \tag{F.10}$$

The final solution step is to integrate (F.4), $f(\sigma,\tau)$ =constant, and apply boundary conditions at $\sigma = 0$ for region I ($\tau > 0$) and region II ($\tau < 0$), separately. The result is

$$f(\sigma,\tau) = \begin{cases} f_1\left(\frac{qE_x}{m^*}\tau\right) & \text{region I} \\ f_2\left(\frac{qE_x}{m^*}\tau\right) & \text{region II.} \end{cases} \tag{F.11}$$

Upon inverse transformation,

$$f(x,v_x) = \begin{cases} f_1\left(\sqrt{v_x^2 - \frac{2qE_x}{m^*}x}\right) & \text{region I} \\ f_2\left[-\sqrt{v_x^2 + \frac{2qE_x}{m^*}(L_x - x)}\right] & \text{region II.} \end{cases} \tag{F.12}$$

[2]Inversion of (F.7) and (F.8) results in two sets of inverse transformation equations. Only one set meets the transformation requirements throughout the boundary condition domain, (F.9) and (F.10), in which it is to be understood that the positive square roots are to be taken; the other spurious set is ignored. Note that $x < mv_x^2/2qE_x$ in region I, so that the quantity under the square root in (F.9) is positive.

Equation (F.12) can be expressed in terms of boundary conditions used in Sections 2.2 and 3.1, namely, $f_1 = f_o$ and $f_2 = 0$, where f_o is the equilibrium Maxwellian defined in (2.31):

$$f(x, v_x) = \begin{cases} \exp\left(\frac{qE_x}{k_B T} x\right) f_o(v_x) & v_x > \sqrt{\frac{2qE_x}{m^*} x} \\ 0 & v_x < \sqrt{\frac{2qE_x}{m^*} x}, \end{cases} \tag{F.13}$$

$$qE_x > 0 \text{ and } 0 < x < L_x.$$

The negative constant-field version of (F.13) can be written by inspection, after noting the effect of the transformation $x' = L_x - x$, $v' = -v$, $qE'_x = -qE_x$ on (F.1), (F.2), and (F.3), and on regions I and II of Fig. F.1. Thus,

$$f(x, v_x) = \begin{cases} \exp\left(\frac{qE_x}{k_B T} x\right) f_o(v_x) & v_x > -\sqrt{\frac{2qE_x}{m^*}(x - L_x)} \\ 0 & v_x < -\sqrt{\frac{2qE_x}{m^*}(x - L_x)}, \end{cases} \tag{F.14}$$

$$qE_x < 0 \text{ and } 0 < x < L_x.$$

Appendix G

Mathematical Properties of Monodimensional Fourier, Tchebycheff, and Hermite-Gaussian Basis Functions

Various basis sets have been employed, at one time or another, throughout this work. The important mathematical properties of the functions that make up these sets will be reviewed. The comprehensive reference *Handbook of Mathematical Functions* by Abramowitz and Stegun [24] should be consulted for a more thorough treatment.

G.1 Fourier Basis Functions

A Fourier basis set derives from a sequence of trigonometric functions defined on the interval [-1,+1]. These functions are solutions to one of the the simplest second-order ordinary differential equations,

$$\frac{d^2y}{dx^2} = \begin{cases} -\left(\frac{n\pi}{2}\right)^2 y & \text{if } n \text{ and } y \text{ have even parity} \\ \left[\frac{(n+1)\pi}{2}\right]^2 y & \text{if } n \text{ and } y \text{ have odd parity.} \end{cases} \tag{G.1}$$

$$n = 0, 1, 2, \cdots.$$

Solutions to (G.1) are given by the trigonometric functions

$$F_n(x) = \begin{cases} \cos\left(\frac{n\pi x}{2}\right) & n \text{ even } (n = 0, 2, 4, \cdots) \\ \sin\left[\frac{(n+1)\pi x}{2}\right] & n \text{ odd } (n = 1, 3, 5, \cdots). \end{cases} \tag{G.2}$$

The Fourier set begins $\{1, \sin\pi x, \cos\pi x, \sin 2\pi x, \cos 2\pi x, \cdots\}$; the first seven elements are plotted in Fig. G.1.[1] Notice that n and F_n have identical parity for all n.

The functions F_n are mathematically complete and are orthogonal over [-1,+1]:

$$\int_{-1}^{1} dx\ F_m(x)F_n(x) = \begin{cases} 0 & m \neq n \\ 2 & m = n = 0 \\ 1 & m = n \neq 0. \end{cases} \tag{G.3}$$

In the interval [-1,+1] F_n for n even and $n > 0$ possesses n zeros and $n+1$ extrema, while for n odd possesses $n+2$ zeros and $n+1$ extrema. The zeros are defined by $F_n(z_i) = 0$, that is,

$$z_i = \begin{cases} \pm\frac{(2i-1)}{n} & i = 1, 2, \cdots, n/2;\ n \text{ even and } n > 0 \\ \pm\frac{2(i-1)}{n+1} & i = 1, 2, \cdots, (n+3)/2;\ n \text{ odd.} \end{cases} \tag{G.4}$$

And similarly, the extrema are defined by $F'(e_i) = 0$; hence,

$$e_i = \begin{cases} \pm\frac{2(i-1)}{n} & i = 1, 2, \cdots, (n+2)/2;\ n \text{ even and } n > 0 \\ \pm\frac{(2i-1)}{n+1} & i = 1, 2, \cdots, (n+1)/2;\ n \text{ odd.} \end{cases} \tag{G.5}$$

G.2 Tchebycheff Basis Functions

Besides trigonometric functions, Tchebycheff polynomials are also useful in constructing a basis set. They are solutions to Tchebycheff's differential

[1] The reader should not be confused by the fact that the F_n are labeled $n = 0, 1, 2, \cdots$, whereas the one-dimensional basis functions, $\phi_n(v_x)$ (Section 3.1), and constituent functions—$\phi_{2\ell}(v_\rho)$ and $\phi_m(v_x)$ (Section 3.2); and $\phi_\kappa(v_x)$, $\phi_\ell(v_y)$, and $\phi_{2m}(v_x)$ (Section 4.1)—are labeled $n, \kappa, \ell, m = 1, 2, 3, \cdots$. The former labeling convention is customary in purely mathematical treatments and will be adhered to in this appendix.

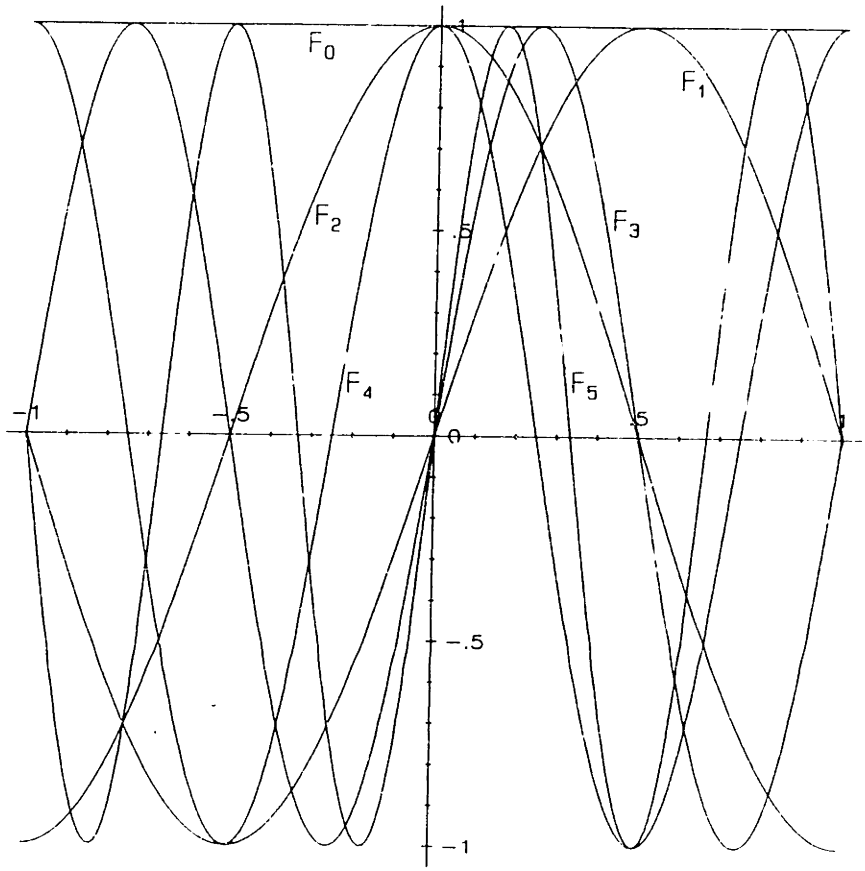

Figure G.1. Fourier monodimensional basis elements ($n = 0, \cdots, 6$).

equation

$$(1-x^2)\frac{d^2y}{dx^2} - x\frac{dy}{dx} + n^2 y = 0, \tag{G.6}$$

$$n = 0, 1, 2, \cdots.$$

Solutions of (G.6) are given by[2]

$$T_n(x) = \cos(n \cos^{-1} x). \tag{G.7}$$

The first several Tchebycheff basis elements are $\{1, x, 2x^2-1, 4x^3-3x, 8x^4-8x^2+1, \cdots\}$. Polynomials T_0 through T_6 are plotted in Fig. G.2. Like the trigonometric functions, T_n and n always have the same parity.

Tchebycheff polynomials obey the recursion formula

$$T_{n+1}(x) = 2xT_n(x) - T_{n-1}(x). \tag{G.8}$$

Formula (G.8) is of particular service when generating the T_n numerically. In addition, Tchebycheff polynomials are mathematically complete, and further, they are orthogonal with respect to the weighting function $(1-x^2)^{-1/2}$ over [-1,+1]:

$$\int_{-1}^{1} dx \, \frac{T_m(x)T_n(x)}{\sqrt{1-x^2}} = \begin{cases} 0 & m \neq n \\ \pi & m = n = 0 \\ \pi/2 & m = n \neq 0. \end{cases} \tag{G.9}$$

The n zeros of T_n in [-1,+1], $T(z_i) = 0$, are

$$z_i = \cos\left[\frac{(2i-1)\pi}{2n}\right] \quad i = 1, 2, \cdots, n; \; n > 0. \tag{G.10}$$

Correspondingly, the $n+1$ extrema, $T'(e_i) = 0$, are located at

$$e_i = \cos\left[\frac{(i-1)\pi}{n}\right] \quad i = 1, 2, \cdots, n+1. \tag{G.11}$$

[2]In this case, one of two possible solutions is sought, Tchebycheff polynomials of the first kind [24].

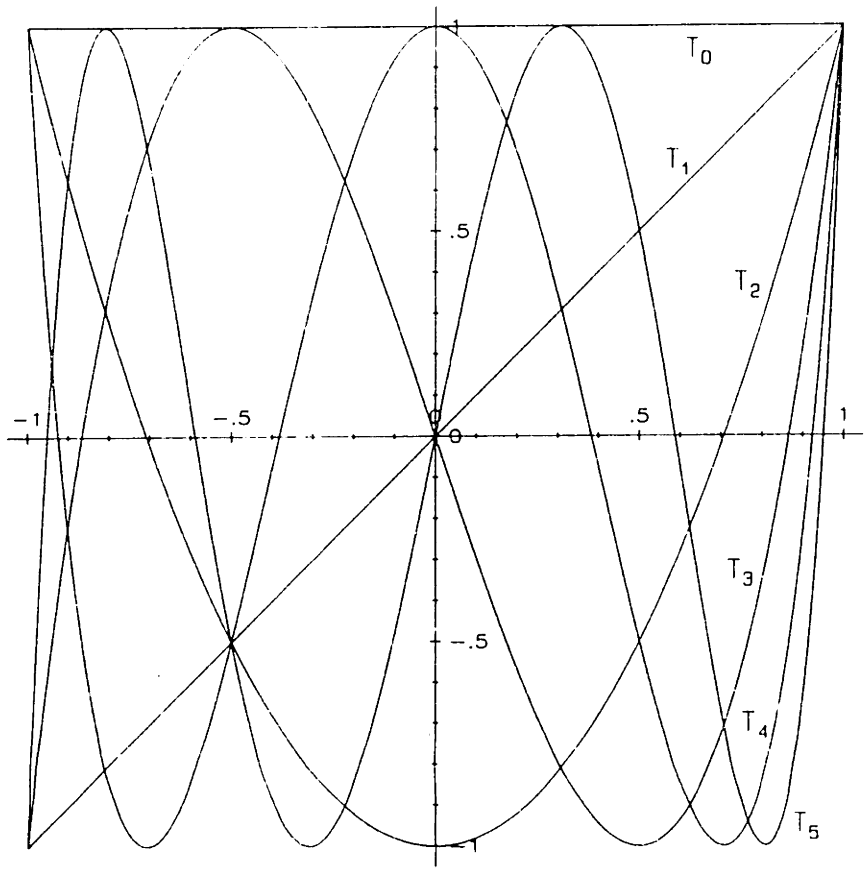

Figure G.2. Tchebycheff monodimensional basis elements ($n = 0, \cdots, 6$).

G.3 Hermite-Gaussian Basis Functions

Most FD-spectral calculations carried out in this thesis implement a Hermite-Gaussian basis set, whose elements are constructed from solutions to

$$\frac{d^2y}{dx^2} + (2n + 1 - x^2)y = 0, \qquad (G.12)$$
$$n = 0, 1, 2, \cdots.$$

Equation (G.12) is the one-dimensional parabolic-potential Schrodinger equation [35]. Solutions to (G.12) are given by

$$S_n(x) = \frac{(-1)^n}{\sqrt{2^n n!}} \exp\left(\frac{x^2}{2}\right) \frac{d^n}{dx^n} \exp(-x^2) \qquad (G.13)$$

where $0! \doteq 1$. The functions S_n are called Hermite-Gaussian functions since they consist of a Gaussian, $\exp(-x^2/2)$, multiplied by a sequence of Hermite polynomials.[3] The Hermite-Gaussian set starts with $(2^n n!)^{-1/2} \exp(-x^2/2) \times \{1, 2x, 4x^2 - 2, 8x^3 - 12x, 16x^4 - 48x^2 + 12, \cdots\}$. Hermite-Gaussian functions up to S_6 are plotted in Fig. G.3; n and S_n always have the same parity as in the previous Fourier and Tchebycheff cases.

In numerical applications the recursion formula

$$S_{n+1}(x) = 2xS_n(x) - 2nS_{n-1}(x) \qquad (G.14)$$

is of frequent use. Note, too, the S_n are mathematically complete over the infinite interval $(-\infty, +\infty)$ with orthogonality relation

$$\int_{-\infty}^{\infty} dx\ S_m(x)S_n(x) = \begin{cases} 0 & m \neq n \\ \sqrt{\pi} & m = n. \end{cases} \qquad (G.15)$$

The Hermite-Gaussian function S_n possesses $n - 1$ zeros and n extrema throughout $(-\infty, +\infty)$. Unfortunately, there are no known closed-form expressions for their exact location. In any event, the numerical algorithm outlined in Appendix C.3 can be called upon.

[3] Hermite polynomials, $H_n(x)$, can be shown to satisfy Hermite's differential equation $y'' - 2xy' + 2ny = 0$, $n = 0, 1, 2, \cdots$.

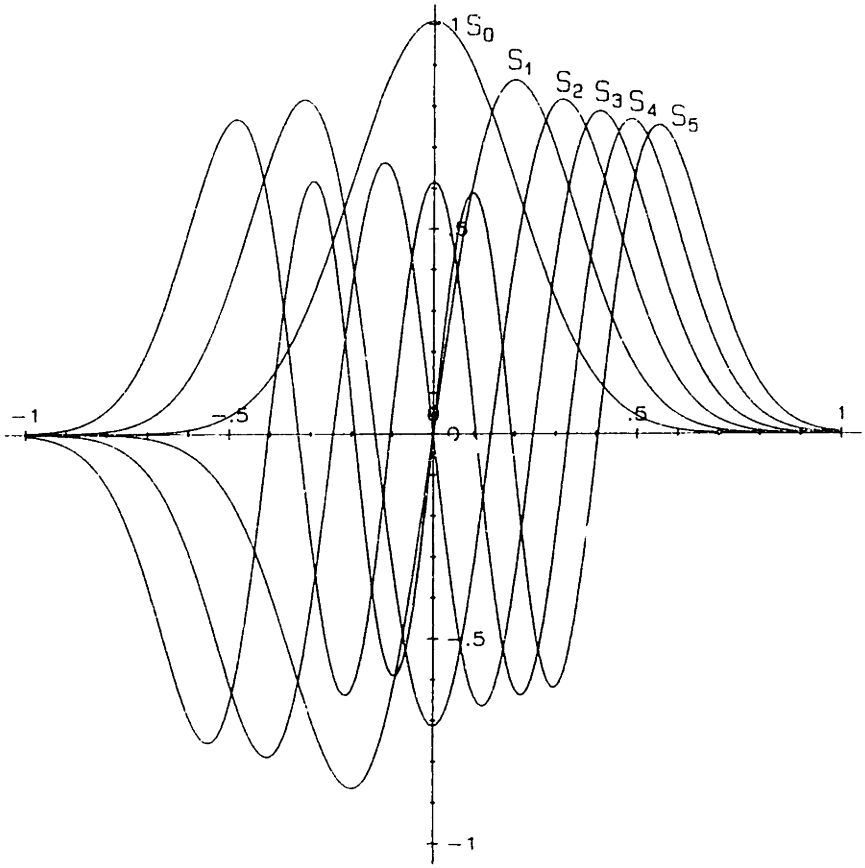

Figure G.3. Hermite-Gaussian monodimensional basis elements ($n = 0, \cdots, 6$).

Appendix H

Boundary Conditions in Two-Dimensional Transversally Periodic and Mirror-Symmetric Structures

Different types of boundary conditions that pertain to the BTE have been touched upon in Section 1.1.2. A qualitative "derivation" will be given here concerning the boundary conditions along the interface between unit cells of a two-dimensional transversally periodic and mirror-symmetric device structure. Although this situation was not covered in Section 1.1.2, it will be shown in a limiting case that the interfacial boundary condition is equivalent to (1.7) for a reflective boundary. It is this interfacial boundary condition that has been used in solving the (x, y, v_x, v_y, v_z) problem (see Section 4.2.3).

Figure H.1 depicts a two-dimensional transversally periodic and mirror-symmetric device structure. This structure has been chosen to resemble the idealized cross section of a permeable-base transistor [4], for the sake of realism. Yet, the following arguments are generally applicable to any two-dimensional transverse-periodic structure possessing mirror symmetry (geometrical and material) about the unit-cell interfaces.[1] The solid up-

[1] Mirror symmetry about the unit-cell interfaces of a periodic structure also implies mirror symmetry about the mid-plane of the unit cell, and vice versa. This is easily proved by using the defining property that if a function g has parity p upon reflection about the plane $x = x_o$, then $g(x_o + \epsilon) = (-1)^p g(x_o - \epsilon)$. Assume the unit-cell interface $x = 0$ is a plane of mirror

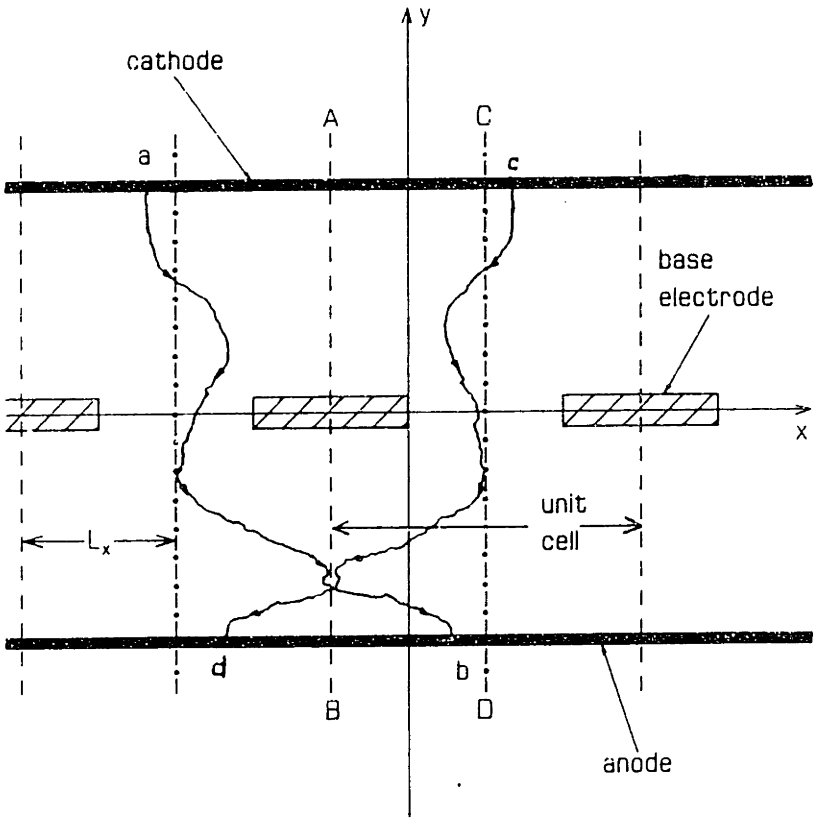

Figure H.1. A two-dimensional transversally periodic and mirror-symmetric device structure.

per and lower horizontal lines represent cathode and anode (emitter and collector) electrodes, respectively. Mathematically, these electrodes are adequately described with the injective boundary conditions (1.6). The series of cross-hatched horizontal lines represent internal base electrodes; the reflective boundary condition (1.7) is well suited in mathematically describing these electrodes. The dashed vertical lines represent the interface between unit cells, which repeat indefinitely in x. The BTE is to be solved in the half-unit cell enclosed by segments AB and CD, after which symmetry arguments can be made to construct the solution elsewhere.

First, imagine the electric-field distribution $E_x(x,y)\hat{e}_x + E_y(x,y)\hat{e}_y$ in the structure of Fig. H.1. Since the geometrical and material properties of the structure are assumed to be mirror symmetric with respect to lines AB, CD, and all other equivalent lines, the x component of electric field must also be mirror symmetric about those symmetry lines. In other words, if either AB or CD passes through x_o then

$$E_x(x_o + \epsilon, y) = -E_x(x_o - \epsilon, y) \tag{H.1}$$

for $0 \leq \epsilon \leq L_x$. This can be justified by asserting that an observer at $(x_o+\epsilon, y)$ or at $(x_o-\epsilon, y)$ would "see" mirror-symmetric charge distributions about the line $x = x_o$. In addition, as a special case of (H.1), if there is no trapped interfacial charge density along symmetry lines (AB, CD, and other equivalent ones), the electric field must be continuous at those lines. Thus, $\lim_{\epsilon\to 0} E_x(x_o + \epsilon, y) = \lim_{\epsilon\to 0} -E_x(x_o - \epsilon, y)$, which can be true only if $E_x(x_o, y) = 0$, where $x = x_o$ can now coincides with any mirror-symmetry line. An analogous charge-symmetry argument can be made to show

$$E_y(x_o + \epsilon, y) = E_y(x_o - \epsilon, y) \tag{H.2}$$

for $0 \leq \epsilon \leq L_x$.

Now, imagine the distribution of carriers in the structure of Fig. H.1. In accordance with the comments of Section 4.1 the carrier velocity distribution is mirror symmetric about the (v_x, v_y) plane: $f = f(x, y, v_x, v_y, |v_z|)$. This is a direct consequence of three basic facts: (1) anode and cathode injected

---

symmetry and that the periodicity of the structure is L_x. Then $g(\frac{1}{2}L_x+\epsilon) = (-1)^p g(-\frac{1}{2}L_x-\epsilon) = (-1)^p g(\frac{1}{2}L_x - \epsilon)$, proving that $\frac{1}{2}L_x$ is also a plane of mirror symmetry. Conversely, assume that $\frac{1}{2}L_x$ is a plane of mirror symmetry. Then $g(\epsilon) = (-1)^p g(L_x - \epsilon) = g(-\epsilon)$, proving that $x = 0$ is also a plane of mirror symmetry.

velocity distributions are even functions of v_z, (2) the scattering probability-rate function $S(\boldsymbol{v}, \boldsymbol{v}')$ is an even function of v_z' (see Appendix E), and (3) $\boldsymbol{E}$ is a two-dimensional vector field in the (x, y) plane. The distribution function can be viewed as a (steady-state) histogram of positions and velocities for a large number of individual carrier trajectories [which happens also to be the approach used in the Monte-Carlo method (see Section 1.2.1)]. With reference to Fig. H.1, all possible carrier trajectories can be reduced to pairs of mirror-symmetric trajectories such as *ab* and *cd*. This is ensured by Eqs. (H.1) and (H.2), the facts enumerated earlier, and the additional property $S(v_x, v_y, v_z, v_x', v_y', v_z') = S(-v_x, v_y, v_z, -v_x', v_y', v_z')$ (see Appendix E), if anode and cathode boundary conditions are spatially homogeneous. Therefore, the distribution function must obey

$$f(x_o + \epsilon, y, v_x, v_y, |v_z|) = f(x_o - \epsilon, y, -v_x, v_y, |v_z|) \tag{H.3}$$

for $0 \leq \epsilon \leq L_x$, and for any mirror-symmetry line $x = x_o$. Under circumstances where the spatial domain has to be absolutely restricted within AB and CD, it is necessary to evaluate (H.3) for $\epsilon \to 0$, which is simply[2]

$$f(x_o, y, v_x, v_y, |v_z|) = f(x_o, y, -v_x, v_y, |v_z|) \tag{H.4}$$

Equation (H.4) is merely a special case of the reflective boundary condition (1.7). Note that (H.4) can be interpreted as a "no-flow" condition since $J_x(x_o, y) = \int d^3v \; v_x f = 0$.

[2]It is worth remarking that condition (H.3) results in a convenient boundary condition for numerical solution of the (x, y, v_x, v_y, v_z) problem (see Section 4.2.3). In this instance the distribution function is not absolutely restricted within AB and CD but is sampled a distance $\epsilon = \Delta x/2$ just outside these symmetry lines (refer to Fig. H.1). If, however, the finite-difference mesh is displaced so that the distribution function is sampled exactly on either or both symmetry lines AB and CD, condition (H.4) can then be applied.

Appendix I

Evaluation of Distribution Function Moments

Spectral representation of the distribution function's velocity dependence greatly facilitates numerical moment evaluation. The generalized Pth-rank moment tensor is

$$\mathcal{M}_P(\boldsymbol{r},t) \doteq \int d^3v\ \boldsymbol{v}^P f(\boldsymbol{r},\boldsymbol{v},t), \tag{I.1}$$

its tensor character made evident by definition of the tensor quantity $\boldsymbol{v}^P$ with elements

$$\{\boldsymbol{v}^P\}_{i_1,i_2,\cdots,i_P} \doteq \prod_{p=1}^{P} v_{i_p}. \tag{I.2}$$

Equations (I.1) and (I.2) have been presented in general notation so as to apply to any of the problems in Chapters 2 through 4.[1] Observe also that the zeroth- and first-rank moment tensors ($P = 0, 1$, respectively) are the carrier concentration and current density, $\mathcal{M}_0(\boldsymbol{r},t) = n(\boldsymbol{r},t)$ and $\mathcal{M}_1(\boldsymbol{r},t) = J(\boldsymbol{r},t)$; the second-rank moment tensor ($P = 2$) is commonly denoted the energy tensor, $\mathcal{M}_2(\boldsymbol{r},t) = W(\boldsymbol{r},t)$.

The FD-spectral decomposition (1.14) implies

$$\mathcal{M}_P(\boldsymbol{r},t) = \sum_{n=1}^{N} \alpha_n(\boldsymbol{r},t)\mathsf{m}_{nP}, \tag{I.3}$$

[1] To illustrate, the (z, v_ρ, v_z) problem requires $\boldsymbol{r} \to z\hat{\boldsymbol{e}}_z$, $\boldsymbol{v} \to v_\rho\hat{\boldsymbol{e}}_\rho + v_z\hat{\boldsymbol{e}}_z$, $d^3v \to 2\pi v_\rho dv_\rho dv_z$, and $(v_\rho, v_z) \to (v_1, v_2)$, $i_p = 1, 2$, in (I.1) and (I.2).

with the N "moment parameters"

$$\mathsf{m}_{nP} = \int d^3v \; v^P \Phi_n(v), \tag{I.4}$$

$$n = 1, \cdots, N.$$

Therefore, numerically efficient moment evaluation would first entail a "one-time-only" determination of the m_{nP} according to (I.4), and then, for any subsequent FD-spectral calculation, the use of (I.3).

Additional simplification is possible if symmetries in basis function constituents are exploited. This is most easily understood by way of example. Take the third-rank tensor element $\{M_3(r,t)\}_{201}$ associated with the (x, y, v_x, v_y, v_z) problem. In terms of constituent functions,

$$\{M_3(r,t)\}_{201} = \sum_{\kappa,\ell,m} \alpha_{\kappa\ell m}(r,t) m_{\kappa 2} m_{\ell 0} m_{(2m)1}, \tag{I.5}$$

where

$$m_{\mu\nu} = \int d\xi \; \xi^\nu \phi_\mu(\xi), \tag{I.6}$$

$$\mu\nu = \kappa 2, \; \ell 0, \; (2m)1.$$

The constituent moment parameters $m_{\kappa 2}, m_{\ell 0}$, and $m_{(2m)1}$ either vanish or need only be integrated over a semi-infinite interval depending on the respective parities of their integrands.

Bibliography

[1] S.M. Sze, *VLSI Technology* (McGraw-Hill, New York, 1983).

[2] S.K. Ghandi, *VLSI Fabrication Principles* (Wiley, New York, 1983).

[3] H. Morkoc and P.M. Solomon, IEEE Spectrum **21**, 28 (1984).

[4] S.M. Sze, *Physics of Semiconductor Devices* (Wiley, New York, 1981).

[5] F. Reif, *Fundamentals of Statistical and Thermal Physics* (McGraw-Hill, New York, 1965).

[6] O. Madlung, *Introduction to Solid-State Theory* (Springer-Verlag, New York, 1981).

[7] B.R. Nag, *Electron Transport in Compound Semiconductors* (Springer-Verlag, New York, 1980).

[8] E.M. Conwell, *High Field Transport in Semiconductors* (Academic, New York, 1967).

[9] C. Jacoboni and L. Reggiani, Rev. Mod. Phys. **55**, 698 (1983).

[10] W. Fawcett, A.D. Boardman, and S. Swain, J. Phys. Chem. Solids **31**, 1963 (1970).

[11] A. van der Ziel, *Solid State Physical Electronics* (Prentice-Hall, Englewood Cliffs, New Jersey, 1976).

[12] H.D. Rees, J. Phys. Chem. Solids **30**, 643 (1969).

[13] P.A. Lebwohl and P.M. Marcus, Solid State Commun. **9**, 1671 (1971).

[14] B.A. Finalyson, *The Method of Weighted Residuals and Variational Principles* (Academic Press, New York, 1972)

[15] G. Dalquist and A. Bjorck, *Numerical Methods* (Prentice-Hall, Englewood Cliffs, New Jersey, 1974).

[16] D.Gottlieb and S.A. Orzag, *Numerical Analysis of Spectral Methods: Theory and Applications* (SIAM, Philadelphia, 1977).

[17] W.M. Stacey, *Modal Approximations: Theory and Applications to Reactor Physics* (MIT Press, Cambridge, Massachusetts, 1967).

[18] L.M. Delves and T.L. Freeman, *Analysis of Global Expansion Methods: Weakly Asymptotically Diagonal Systems* (Academic Press, New York, 1981).

[19] H.D. Rees, J. Phys. C. **6**, 262 (1973).

[20] L. Lapidus and G.F. Pinder, *Numerical Solution of Partial Differential Equations in Science and Engineering* (Wiley, New York, 1982).

[21] V. Vemuri and W.J. Karplus, *Digital Computer Treatment of Partial Differential Equations* (Prentice-Hall, Englewood Cliffs, New Jersey, 1981).

[22] C.W. Gear, *Numerical Initial Value Problems in Ordinary Differential Equations* (Prentice-Hall, Englewood Cliffs, New Jersey, 1971).

[23] D. Potter, *Computational Physics* (Wiley, New York, 1973).

[24] M. Abramowitz and I.A. Stegun, *Handbook of Mathematical Functions* (Dover, New York, 1972).

[25] R.V. Churchill and J.W. Brown, *Fourier Series and Boundary Value Problems* (McGraw-Hill, New York, 1978).

[26] Y. Awano and N. Hashizume, "Electrical Properties of GaAs Ballistic FET", to be published (Electrotechnical Laboratory, 1-1-4 Umezono, Japan, 1983).

[27] W.R. Frensley, IEEE Trans. Electron Devices **ED-30**, 1624 (1983).

[28] R.E. Mortensen, *Random Signals and Systems* (Wiley, New York, 1987).

[29] J.F. Botha and G.F. Pinder, *Fundamental Concepts in the Numerical Solution of Differential Equations* (Wiley, New York, 1983).

[30] M.Y. Hussaini, C.L. Streett, and T.A. Zang, *Spectral Methods for Partial Differential Equations*, ICASE Report No. 83-46, NASA Langley Research Center, Hampton, Virginia, 1983.

[31] J.R. Barker, *Physics of Nonlinear Transport in Semiconductors* (Plenum, New York, 1980).

[32] F. Capasso, K. Mohammed, and A.Y. Cho, IEEE J. Quantum Electron. **QE-22**, 1853 (1986).

[33] B. Kolman, *Introductory Linear Algebra with Applications* (Macmillan, New York, 1976).

[34] R. Courant and D. Hilbert, *Methods of Mathematical Physics* (Wiley, New York, 1962).

[35] L.I. Schiff, *Quantum Mechanics* (McGraw-Hill, New York, 1968).